

Polymer Nanocomposite Processing, Characterization, and Applications 2012

Guest Editors: Gaurav Mago, Sadhan C. Jana, Suprakas Sinha Ray,
and Tony McNally





**Polymer Nanocomposite Processing,
Characterization, and Applications 2012**

Journal of Nanomaterials

**Polymer Nanocomposite Processing,
Characterization, and Applications 2012**

Guest Editors: Gaurav Mago, Sadhan C. Jana,
Suprakas Sinha Ray, and Tony McNally



Copyright © 2012 Hindawi Publishing Corporation. All rights reserved.

This is a special issue published in "Journal of Nanomaterials." All articles are open access articles distributed under the Creative Commons Attribution License, which permits unrestricted use, distribution, and reproduction in any medium, provided the original work is properly cited.

Editorial Board

- Katerina Aifantis, Greece
Nageh K. Allam, USA
Margarida Amaral, Portugal
Xuedong Bai, China
L. Balan, France
Enrico Bergamaschi, Italy
Theodorian Borca-Tasciuc, USA
C. Jeffrey Brinker, USA
Christian Brosseau, France
Xuebo Cao, China
Shafiul Chowdhury, USA
Kwang-Leong Choy, UK
Cui ChunXiang, China
Miguel A. Correa-Duarte, Spain
Shadi A. Dayeh, USA
Claude Estournes, France
Alan Fuchs, USA
Lian Gao, China
Russell E. Gorga, USA
Hongchen Chen Gu, China
Mustafa O. Guler, Turkey
John Zhanhu Guo, USA
Smrati Gupta, Germany
Michael Harris, USA
Zhongkui Hong, USA
Michael Z. Hu, USA
David Hui, USA
Y.-K. Jeong, Republic of Korea
Sheng-Rui Jian, Taiwan
Wanqin Jin, China
Rakesh K. Joshi, India
Zhenhui Kang, China
Fathallah Karimzadeh, Iran
Alireza Khataee, Iran
- Do Kyung Kim, Korea
Kin Tak Lau, Australia
Burtrand Lee, USA
Benxia Li, China
Jun Li, Singapore
Shijun Liao, China
Gong Ru Lin, Taiwan
J.-Y. Liu, USA
Jun Liu, USA
Tianxi Liu, China
Songwei Lu, USA
Daniel Lu, China
Jue Lu, USA
Ed Ma, USA
Gaurav Mago, USA
Santanu K. Maiti, Israel
Sanjay R. Mathur, Germany
A. McCormick, USA
Vikas Mittal, UAE
Weihai Ni, Germany
Sherine Obare, USA
Abdelwahab Omri, Canada
Edward Andrew Payzant, USA
Kui-Qing Peng, China
Anukorn Phuruangrat, Thailand
Ugur Serincan, Turkey
Huaiyu Shao, Japan
Donglu Shi, USA
Suprakas Sinha Ray, South Africa
Vladimir Sivakov, Germany
Marinella Striccoli, Italy
Bohua Sun, South Africa
Saikat Talapatra, USA
Nairong Tao, China
- Titipun Thongtem, Thailand
Somchai Thongtem, Thailand
Alexander Tolmachev, Ukraine
Valeri P. Tolstoy, Russia
Tsung-Yen Tsai, Taiwan
Takuya Tsuzuki, Australia
Raquel Verdejo, Spain
Mat U. Wahit, Malaysia
Shiren Wang, USA
Yong Wang, USA
Ruibing Wang, Canada
Cheng Wang, China
Zhenbo Wang, China
Jinquan Wei, China
Ching Ping Wong, USA
Xingcai Wu, China
Guodong Xia, Hong Kong
Zhi Li Xiao, USA
Ping Xiao, UK
Shuangxi Xing, China
Yangchuan Xing, USA
N. Xu, China
Doron Yadlovker, Israel
Ying-Kui Yang, China
Khaled Youssef, USA
William W. Yu, USA
Kui Yu, Canada
Haibo Zeng, China
Tianyou Zhai, Japan
Renyun Zhang, Sweden
Yanbao Zhao, China
Lianxi Zheng, Singapore
Chunyi Zhi, Japan

Contents

Polymer Nanocomposite Processing, Characterization, and Applications 2012, Gaurav Mago, Sadhan C. Jana, Suprakas Sinha Ray, and Tony McNally
Volume 2012, Article ID 924849, 1 page

Fabrication and Application of Iron(III)-Oxide Nanoparticle/Polydimethylsiloxane Composite Cone in Microfluidic Channels, Cheng-Chun Huang, Ming-Dao Wu, Dao Liang, Jiashing Yu, Po-Jen Shih, and Wen-Pin Shih
Volume 2012, Article ID 986454, 10 pages

Analysis of Gas Permeability Characteristics of Poly(Lactic Acid)/Poly(Butylene Succinate) Nanocomposites, Amita Bhatia, Rahul K. Gupta, Sati N. Bhattacharya, and Hyoung Jin Choi
Volume 2012, Article ID 249094, 11 pages

Layer-by-Layer Nanoassembly of Copper Indium Gallium Selenium Nanoparticle Films for Solar Cell Applications, A. Hemati, S. Shrestha, M. Agarwal, and K. Varahramyan
Volume 2012, Article ID 512409, 6 pages

Gold/Chitosan Nanocomposites with Specific Near Infrared Absorption for Photothermal Therapy Applications, Guandong Zhang, Xinghua Sun, Jacek Jasinski, Dhruvin Patel, and Andre M. Gobin
Volume 2012, Article ID 853416, 9 pages

Influence of Lauro lactam Content on the Clay Intercalation of Polyamide 6,12/Clay Nanocomposites Synthesized by Open Ring Anionic Polymerization, E. N. Cabrera Álvarez, L. F. Ramos de Valle, F. J. Rodríguez González, F. Soriano-Corral, and R. E. Díaz De León
Volume 2012, Article ID 487948, 7 pages

Electrically Conductive Compounds of Polycarbonate, Liquid Crystalline Polymer, and Multiwalled Carbon Nanotubes, Penwisa Pisitsak, Rathanawan Magaraphan, and Sadhan C. Jana
Volume 2012, Article ID 642080, 10 pages

Direct-Write Drawing of Carbon Nanotube/Polymer Composite Microfibers, Scott M. Berry, Santosh Pabba, Robert W. Cohn, and Robert S. Keynton
Volume 2012, Article ID 690301, 8 pages

Editorial

Polymer Nanocomposite Processing, Characterization, and Applications 2012

Gaurav Mago,¹ Sadhan C. Jana,² Suprakas Sinha Ray,³ and Tony McNally⁴

¹ Department of Mechanical Engineering, Stevens Institute of Technology, Hoboken, NJ 07030, USA

² Department of Polymer Engineering, The University of Akron, 250 South Forge Street, Akron, OH 44325, USA

³ DST/CSIR National Centre for Nano-Structured Materials, Council for Scientific and Industrial Research, Pretoria 0001, South Africa

⁴ School of Mechanical and Aerospace Engineering, Queen's University, Belfast, UK

Correspondence should be addressed to Gaurav Mago, gauravmago2001@gmail.com

Received 17 December 2012; Accepted 17 December 2012

Copyright © 2012 Gaurav Mago et al. This is an open access article distributed under the Creative Commons Attribution License, which permits unrestricted use, distribution, and reproduction in any medium, provided the original work is properly cited.

Polymer nanocomposites have attracted interest in the last few decades providing scope for improvement of various functional properties, such as mechanical, thermal, optical, rheological, magnetic, and electrical. The improvements in functional properties of polymers are achieved at very low loading of nanoparticles. While significant work has been done on preparation and properties of polymer nanocomposites, effort is still needed to elucidate the interrelationship between processing, morphology, and functional properties of nanocomposites. The properties of nanocomposites are affected by a large number of factors including microstructural distributions that are generated during nanocomposite processing as well as the state of nanoparticle distribution in polymer systems. It is believed that understanding of the relationship between processing, morphology and functional properties of nanocomposites will be very helpful in optimizing the ultimate properties of nanocomposites as well as improving the models for predicting properties of nanocomposite systems.

Considering the challenges in the area of processing of nanocomposites, we invited research articles for this special issue with a particular focus on the interrelationships between polymer nanocomposite processing, characterization, and novel applications. This special issue with a total of seven papers covers a wide range of areas related to fabrication of electrically conductive compounds of poly(carbonate), liquid crystalline polymer, and multiwalled carbon nanotubes (CNTs); gas permeability and morphological properties of nanocomposites prepared

by the mixing of poly(lactic acid) (PLA), poly(butylene succinate) (PBS), and clay; synthesis and evaluation of gold/chitosan nanocomposites as a therapeutic agent for the photothermal therapy applications; novel direct-write drawing of CNT/poly(methyl methacrylate) (PMMA) composite microfibers; influence of lauro lactam content on clay intercalation in poly(amide) 6, 12/clay nanocomposites synthesized by open ring anionic polymerization; fabrication and application of iron(III)-oxide nanoparticle/poly(dimethylsiloxane) composite cone in microfluidic channels; and finally layer-by-layer (LbL) nanoassembly of copper indium gallium selenium (CIGS) nanoparticle films for solar cell applications.

It is expected that this special issue will help readers with a wide range of backgrounds to understand the impact of various processing methods as well as nanoparticles on nanocomposite properties, and applications.

Acknowledgments

The Editors would like to acknowledge the invited and contributing authors, reviewers, and staff members of Hindawi Publishing Corporation.

Gaurav Mago
Sadhan C. Jana
Suprakas Sinha Ray
Tony McNally

Research Article

Fabrication and Application of Iron(III)-Oxide Nanoparticle/Polydimethylsiloxane Composite Cone in Microfluidic Channels

Cheng-Chun Huang,¹ Ming-Dao Wu,¹ Dao Liang,¹ Jiashing Yu,²
Po-Jen Shih,³ and Wen-Pin Shih¹

¹ Department of Mechanical Engineering, National Taiwan University, Taipei 10617, Taiwan

² Department of Chemical Engineering, National Taiwan University, Taipei 10617, Taiwan

³ Department of Civil and Environmental Engineering, National University of Kaohsiung, Kaohsiung 81148, Taiwan

Correspondence should be addressed to Wen-Pin Shih, wpshih@ntu.edu.tw

Received 4 May 2012; Accepted 5 December 2012

Academic Editor: Gaurav Mago

Copyright © 2012 Cheng-Chun Huang et al. This is an open access article distributed under the Creative Commons Attribution License, which permits unrestricted use, distribution, and reproduction in any medium, provided the original work is properly cited.

This paper presented the fabrication and applications of an iron(III)-oxide nanoparticle/polydimethylsiloxane (PDMS) cone as a component integrated in lab on a chip. The two main functions of this component were to capture magnetic microbeads in the microfluid and to mix two laminar fluids by generating disturbance. The iron(III)-oxide nanoparticle/PDMS cone was fabricated by automatic dispensing and magnetic shaping. Three consecutive cones of 300 μm in height were asymmetrically placed along a microchannel of 2 mm in width and 1.1 mm in height. Flow passing the cones was effectively redistributed for Reynolds number lower than 3.45×10^{-3} . Streptavidin-coated magnetic microbeads which were bound with biotin were successfully captured by the composite cones as inspected under fluorescence microscope. The process parameters for fabricating the composite cones were investigated. The fabricated cone in the microchannel could be applied in lab on a chip for bioassay in the future.

1. Introduction

Microfluidic device applied in chemical and biological process has drawn more and more attention in research due to versatile advantages such as low fabrication cost, short reaction time, and low reagent consumption. However, the laminar characteristics of flow in microchannel make it difficult to mix two separate flow streams together. Many mixing methodologies have been reported to enhance the mixing efficiency. One of the popular mixing methods is to generate chaotic advection utilizing particular geometric structures in microchannel, such as staggered herringbone pattern on channel surface [1, 2], triangular-wave structures as obstacles along channel side walls [3], and spiral microchannels [4]. Furthermore, PDMS multilayer microfluidic chips with 3D configuration have been fabricated simply to carry out mixing work [5].

Magnetic beads are popular carriers for biological manipulation in microfluidic system under the application

of magnetic field. Particularly, bioanalytic processes such as separation, capture, and recognition [6–9] could be conducted and integrated utilizing magnetic beads. In previous studies [10–13], the magnetic fields were applied from the outside of device with permanent magnet. If the magnetic fields could be generated in specified locations in a microchannel, the external magnet would not be needed and hence the device implementation would be made easier.

In this paper, we fabricate a magnetic nanoparticle/polydimethylsiloxane (PDMS) microcone for mixing fluids due to its three-dimensional asymmetric shape in a microfluidic chip. The fabricated microcone could also be used to capture magnetic beads with its intrinsic magnetism.

2. Design and Experiment

Figure 1 depicts the design of the microfluidic chip composed of three polymethylmethacrylate (PMMA) layers. The microfluidic chip possesses two inlet holes which allow

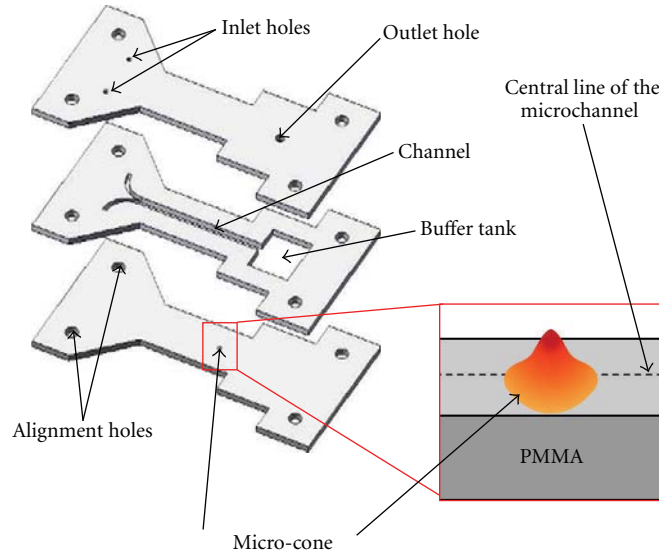


FIGURE 1: Schematics of the proposed microcone in a microfluidic chip.

two different fluids to enter the microchannel and then to encounter the microcone. The fluids can be collected in the buffer tank and then flow out through the outlet hole. There are four alignment holes on each PMMA layer for accurately assembling the microfluidic chip.

Figure 2 illustrates the functionalities of the proposed micro-cone in the microfluidic chip. Let the first fluid in the microchannel contain particles A, which do not possess magnetism, and particles C attached on magnetic beads. The second fluid contains only particles B. The micro-cone is proposed to separate particles A from particles C and then to mix particles A with particles B together. Before the fluids pass through the micro-cone, they are laminar flows in the microchannel. The particles C would be captured by the micro-cone due to the magnetic force when the first fluid passes through the micro-cone. Beyond the micro-cone, the first and the second fluids could be mixed due to the turbulence caused by the cone shape. Therefore, particles A and B could interact. The particles C captured on the micro-cone and the mixture of particles A and B can then be analyzed for versatile applications of lab on a chip. It should be noted that the position of the proposed micro-cone has to be deviated from the central line of the microchannel for enhancing the mixing effect. In our design, the deviated distance is 10% of the microchannel width.

3. Fabrication

Figure 3 details the process for fabricating the microfluidic chip. It is composed of three PMMA layers. All the layers are machined using a CO₂ laser. Each layer is made of a bulk PMMA plate of 1 mm in thickness. To assemble the microfluidic chip, both sides of the middle layer are coated with adhesive of 50 μm in thickness (Figure 3(a)). Therefore, the total depth of the microchannel is 1.1 mm, and the width is 2 mm.

To fabricate the micro-cone, the PDMS prepolymer and curing agent with 10:1 weight ratio are prepared, then

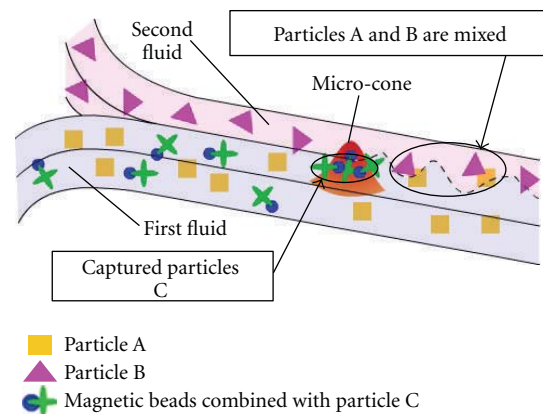


FIGURE 2: Illustrative function of the proposed microcone in a microfluidic chip.

the iron(III)-oxide nanoparticles are dispersed and mixed thoroughly in the PDMS for 10 minutes using regular stirring machine. The mixture is then put in a vacuum chamber for degassing. The iron(III)-oxide nanoparticles (nanopowder of 544884-5G Iron (III)-oxide, SIGMA-ALDRICH) are comprised of primarily the gamma-form Fe₂O₃ which exhibits superparamagnetic behavior [14–17]. The average diameter of the nanoparticles is 50 nm. After degassing, the nanoparticle/PDMS composite is poured into a syringe and then degassing process is conducted again. An automatic dispenser is used to extrude the nanoparticle/PDMS composite into the microchannel. In the beginning of the dispensing process, the initial portion of the nanoparticle/PDMS composite is disregarded in order to obtain constant volume of every single drop. A reference plate with a defined area is put onto the sample stage for aligning the dispenser (Figures 4 and 5). Therefore, the syringe needle can be precisely placed above the designated area. After finishing the alignment, the reference plate is replaced by the bottom

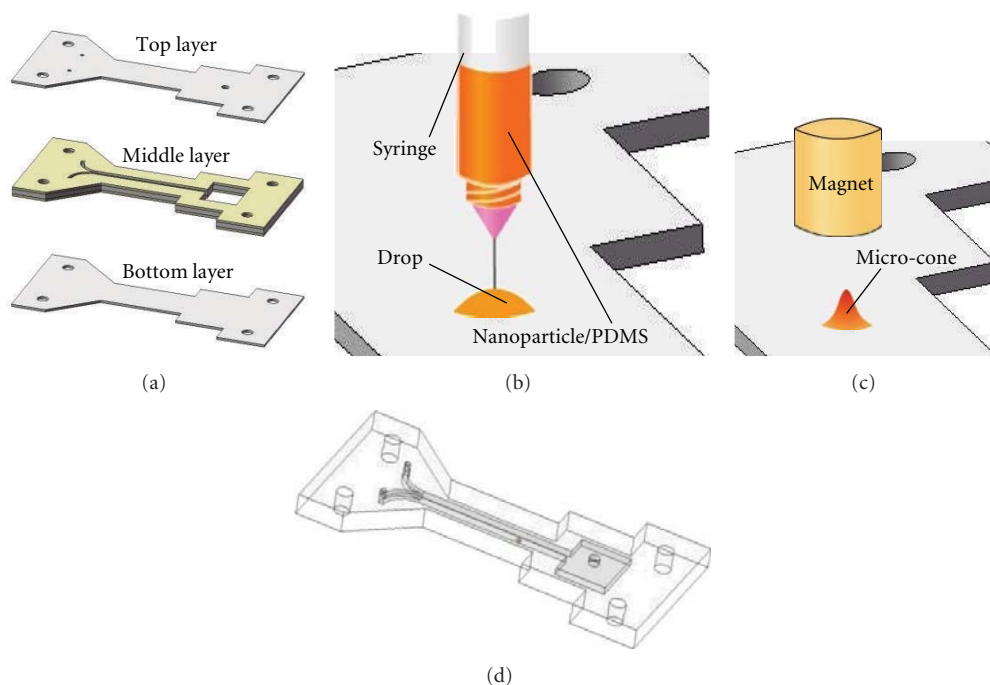


FIGURE 3: Process for fabricating the nanoparticle/PDMS micro-cone. (a) The chip is composed of three bulk PMMA plates. (b) The nanoparticle/PDMS composite is applied through the automatic dispenser. (c) The micro-cone is formed under the applied external magnetic field. (d) Schematic of the fabricated microfluidic chip.

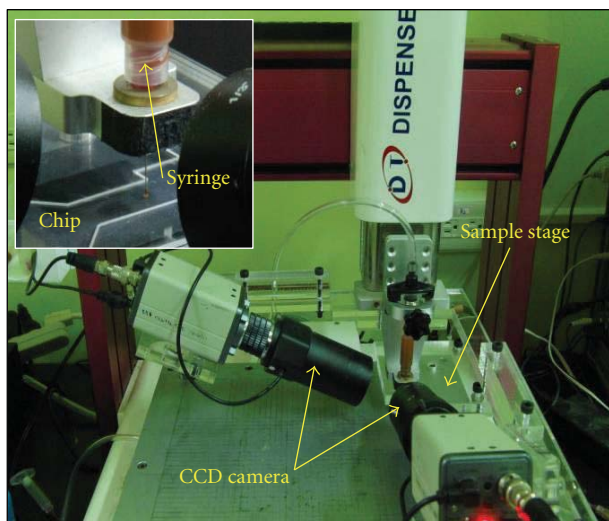


FIGURE 4: Configuration of the automatic dispensing system.

layer of the microfluidic chip. Then a drop of nanoparticle/PDMS composite is dispensed onto the bottom layer (see Figure 3(b)). The dispensing pressure is 0.25 MPa. After dispensing the nanoparticle/PDMS composite, a permanent magnet is placed above the composite (Figure 3(c)). The composite becomes a cone shape due to the external magnetic field. Then the cone is cured at 70°C for 30 minutes. The fabrication environment is at 23°C and 71% relative humidity. After the cone is cured, the three layers of the microfluidic chip are assembled together (Figure 3(d)).

There are two setups to facilitate the fabrication process. One is the automatic dispensing system (Figure 4), and

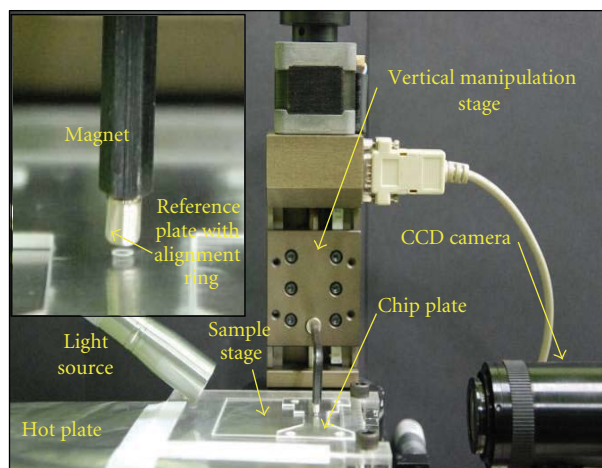


FIGURE 5: Configuration of the magnetic platform.

the other is the magnetic platform for generating the cone shape of the composite (Figure 5). The automatic dispensing system consists of a dispenser (SR-330D), two CCD cameras, and a sample stage. The dispenser is used to extrude iron(III)-oxide nanoparticle/PDMS composites. It features three-axis movement with 50 μm resolution and a controller for adjusting the dispensing pressure and duration. The two CCD cameras assist the alignment of the syringe needle on the substrate and monitor the dispensing process. The sample stage is used to displace the substrate. The magnetic platform includes a vertical manipulation stage, a permanent magnet, a CCD camera, a light source, a sample stage, and a hot plate. The permanent magnet is connected to

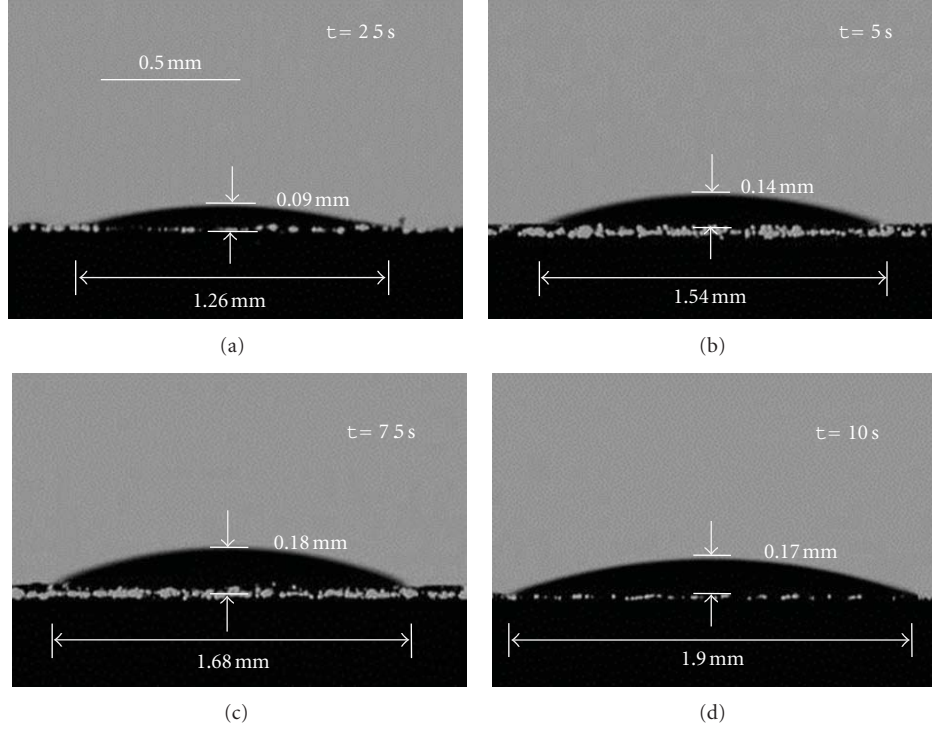


FIGURE 6: Images of the PDMS droplets at different dispensing durations (t). The droplet height (h) and diameter (d) are measured. (a) $t = 2.5$ s. (b) $t = 5$ s. (c) $t = 7.5$ s. (d) $t = 10$ s.

the vertical manipulation stage with 10 nm resolution. The high resolution of the manipulation stage is necessary to finely adjust the distance between the bottom of the magnet and surface of the substrate. The CCD camera is used to monitor the deformation of the uncured nanoparticle/PDMS composite. There is also a sample alignment stages which is placed on the hot plate so that the alignment would not be deviated in the curing process.

The composites with different weight ratios of the nanoparticles are added into the PDMS for evaluating the fabrication parameters. The weight ratios are prepolymer: curing agent: iron(III)-oxide nanoparticle = 40:4:1, 40:4:3, 40:4:5, respectively. Therefore, the weight ratios of the nanoparticles to the composite are 2.22%, 6.38%, and 10.20%, respectively. Different magnetic fields which are controlled by the distance (D) from the bottom of the magnet to the substrate surface are applied. The corresponding magnetic fields of variant distances between substrate and magnet are measured by tesla meter (TM-701, KANETEC CO., LTD). The results are summarized in Table 1.

4. Results

The size of drops could be controlled by the diameter of syringe needle, dispensing pressure and dispensing duration. The stainless steel syringe needle which its inner diameter is 0.15 mm and outer diameter is 0.3 mm was used. The dispensing pressure is fixed at 0.25 MPa. Figure 6 shows the images of PDMS droplets without nanoparticles at different dispensing durations $t = 2.5, 5, 7.5,$ and 10 s. The variation of the droplet size at the same dispensing

TABLE 1: Weight ratios of nanoparticles and magnet height for parametric study.

| | Weight ratio of nanoparticles | | |
|---|-------------------------------|----------------|----------------|
| | 2.22% | 6.38% | 10.20% |
| | 1.0 mm | 1.25 mm | 1.5 mm |
| Distances between substrate and magnet (mm) | 0.220 T | 0.191 T | 0.168 T |
| Magnetic field (Tesla, T) | 1.5 mm | 1.75 mm | 2.0 mm |
| | 0.168 T | 0.148 T | 0.133 T |

parameters is not obvious before and after the nanoparticles adding into the PDMS. This parametric study is conducted for obtaining the desirable droplet diameter (d) and height (h) by controlling the dispensing duration. Since the height of the microchannel is 1.1 mm, the initial height of the PDMS droplet should be relatively smaller. All the initial heights of the PDMS droplets using different dispensing durations in our tests are smaller than 1.1 mm, as shown in Figure 7(a). The average height is $h = 0.09 (\pm 0.007), 0.14 (\pm 0.005), 0.17 (\pm 0.009), 0.19 (\pm 0.018)$ mm for $t = 2.5, 5, 7.5, 10$ s, respectively. Since, in this design, the channel width is 2 mm and the deviated distance from the cone center to the central line of the microchannel is 0.2 mm, the diameter of the PDMS droplet should be smaller than 1.6 mm. The obtained cone diameter is shown in Figure 7(b). The average diameter is $d = 1.28 (\pm 0.029), 1.51 (\pm 0.032), 1.64 (\pm 0.061),$ and $1.79 (\pm 0.067)$ mm for $t = 2.5, 5, 7.5,$ and 10 s, respectively. Therefore, the optimum dispensing duration is 5 s in this test.

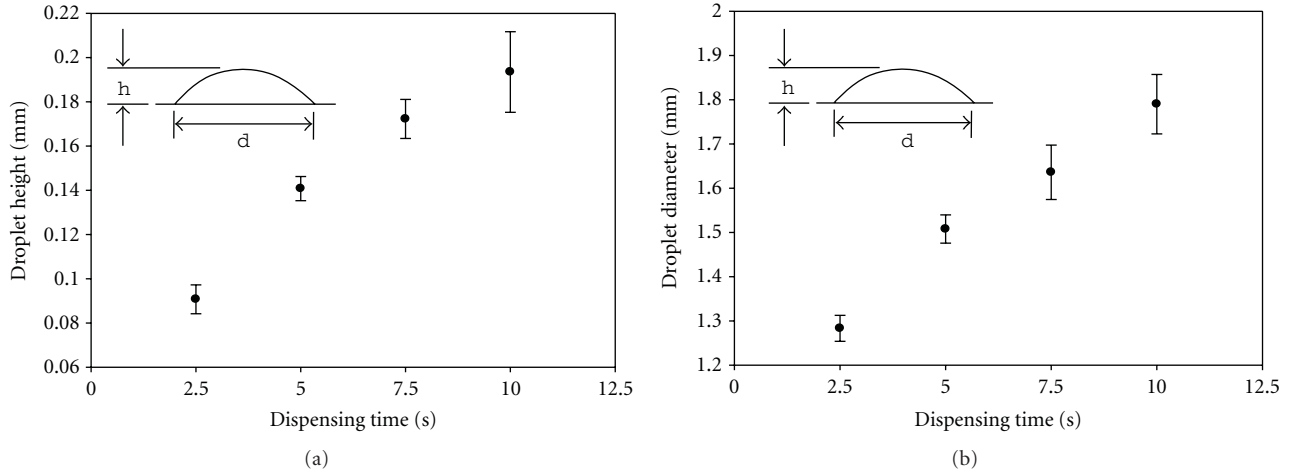


FIGURE 7: Dispensing test for controlling the droplet height and diameter at the constant dispensing pressure of 0.25 MPa. (a) The relation between the droplet height and dispensing duration. (b) The relation between the droplet diameter and dispensing duration.

For each parameter in Table 1, the images of the cone formation are captured every 5 s in 60 s. For the 2.22% weight ratio with 1.0 mm magnetic height, the 6.38% weight ratio with 1.25 mm magnetic height, and the 10.2% weight ratio with 1.5 mm magnetic height, the nanoparticle/PDMS droplets are pulled up and touch the magnet immediately. Therefore, the images of the cone formation for these three particular samples are captured every 1 s. Figure 8(a) shows the height increase (Δh) of the droplet deformation as a function of process time. All the data in Figure 8(a) are from the samples of the 10.20% nanoparticles with the magnetic height of 1.5 mm, 1.75 mm, and 2.0 mm, respectively. For the same process time, the height increase is larger for the lower magnetic height. The error bars in Figure 8(a) stand for the standard deviation from five samples. The deviations are attributed to the vertical and horizontal alignment between the magnet and the center of the droplet. The nondispersed nanoparticles in the uncured PDMS might also affect the repeatability of the cone formation.

The inset of Figure 8(a) shows the height increase of the droplet deformation for the magnetic height of 1.5 mm. The five samples are pulled up and reach the magnet at the process time of 11, 12, 19, 20, and 23 s, respectively. Because the magnet is very close to the droplet, the magnetic force is strong and sensitive to the magnetic height. The variation of the initial droplet might significantly deviate the process time for the droplet to reach the magnet. The height increase of the droplet with 1.5 mm magnetic height and the nanoparticle weight ratio of 2.22%, 6.38%, and 10.20%, respectively, are shown in Figure 8(b). The height increase is larger for the higher weight ratio of nanoparticles. Table 2 shows the height increase at the process time of 30, 40, 50, and 60 s, respectively. The evolution of the height increase with the increasing process time for the samples with 1.5 mm magnetic height and 2.22% nanoparticles is close to that with 1.75 mm magnetic height and 10.2% nanoparticles.

For the 1.75 mm magnetic height in Figure 8(a) and the 6.83% nanoparticles in Figure 8(b), the slope of the curve changes in a piecewise manner with the process time. In

TABLE 2: Parameters of weight ratio of the nanoparticles and the magnetic field.

| | wt. % | Height increase, Δh | | | | |
|--|-------|-----------------------------|-------|-------|-------|-------|
| | | 30 s | 40 s | 50 s | 60 s | |
| Distance between substrate and magnet (mm) | 1.5 | 2.22 | 0.033 | 0.040 | 0.048 | 0.054 |
| | | 6.38 | 0.086 | 0.102 | 0.123 | 0.145 |
| | 1.75 | 6.38 | 0.032 | 0.035 | 0.004 | 0.042 |
| | | 10.2 | 0.032 | 0.038 | 0.043 | 0.051 |

the beginning of applying the magnetic field, the slope is steep for the process time from 0 s to 5 s in Figure 8(a), while the slope becomes smaller for the process time of 5~25 s. Figure 9(a) shows the fabricated microfluidic chip, and Figure 9(b) shows the cross-sectional image of the microchannel. The nanoparticle/PDMS cone is successfully fabricated in the microchannel. The height of the micro-cone is 300 μm , and the deviated distance from the central line is 0.3 mm.

5. Discussions

The method to form the cone shape of the nanoparticle/PDMS composite is to exploit the uncured PDMS deformation as result of being dragged by the nanoparticles. The iron(III)-oxide nanoparticles can be attracted by the permanent magnet. They are mixed in the PDMS and enveloped by the entangling polymer chains. As the magnetic nanoparticles are attracted by the magnetic field above, they would move upward and carry the PDMS together. Because the distribution of the magnetic is hyperbolic (Figure 10(a)), the center of the nanoparticle/PDMS composite is subjected to a relatively stronger magnetic force. Conversely, the rim of the composite is subjected to a weaker magnetic force. As a result, the nanoparticle/PDMS cone can be obtained.

When the magnetic field is applied, the nanoparticles in the composite start to aggregate and to form radiated lines on the cone surface (Figure 10(b)) [18]. There are more nanoparticles aggregating on the tip of the cone in

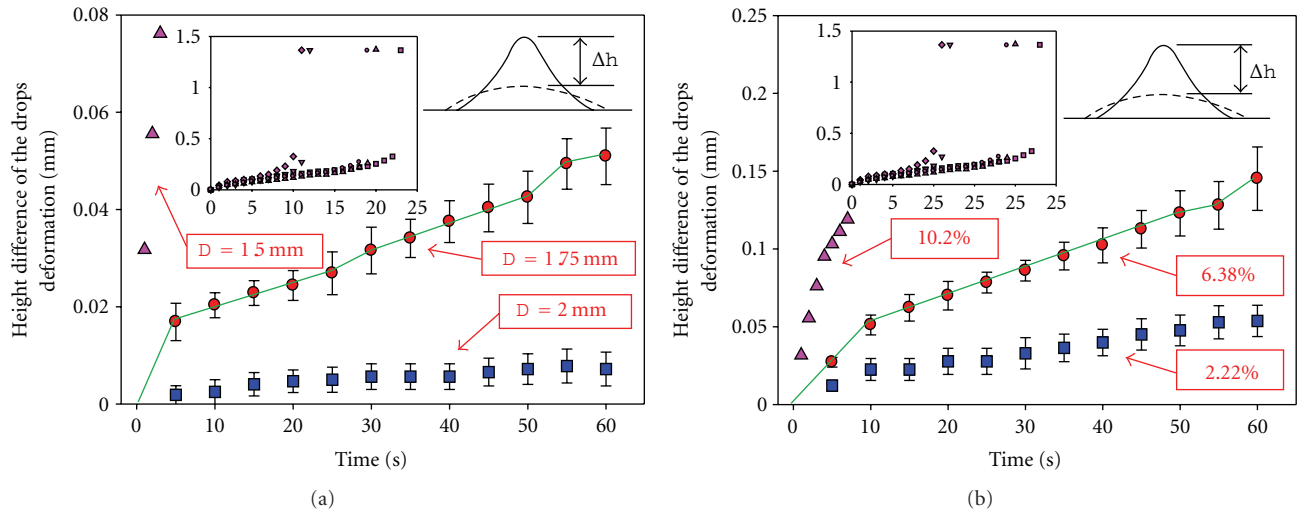


FIGURE 8: The height difference, Δh , of the nanoparticle/PDMS drops deformation. (a) The weight ratio is 10.2%. $D = 1.5, 1.75, 2.0$ mm, respectively. (b) $D = 1.5$ mm. The weight ratios are 2.22%, 6.38%, and 10.2%, respectively.

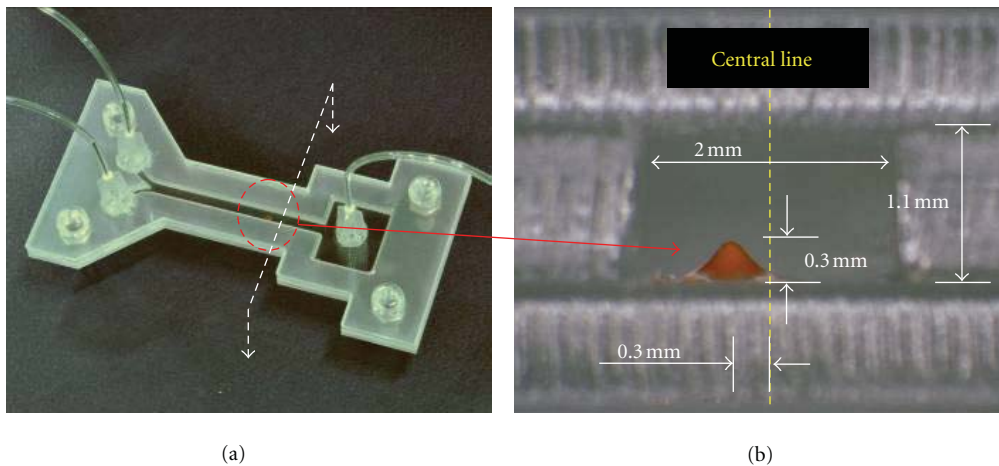


FIGURE 9: The images of the fabricated microfluidic chip. (a) The fabricated chip with fluidic interconnects. (b) The cross-sectional view of the nanoparticle/PDMS cone in the microchannel.

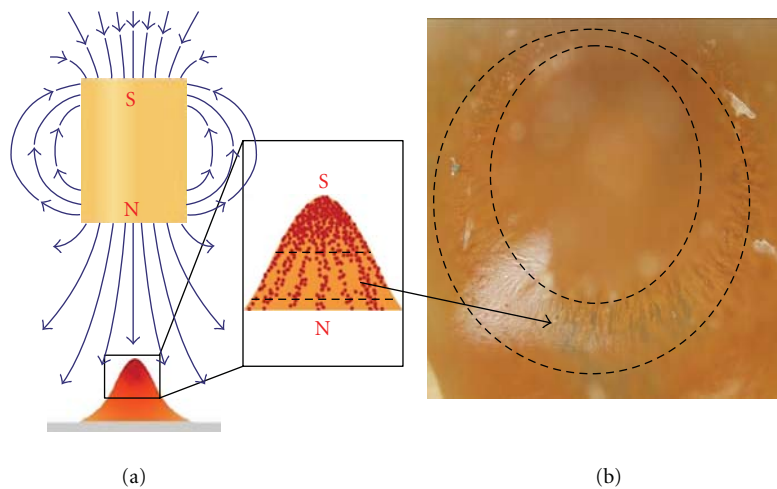


FIGURE 10: Illustration of the magnetism and shape-formation of the cured micro-cone. (a) Schematic of the magnetic field and nanoparticles in PDMS. (b) Top view of the fabricated micro-cone with nanoparticle aggregation.

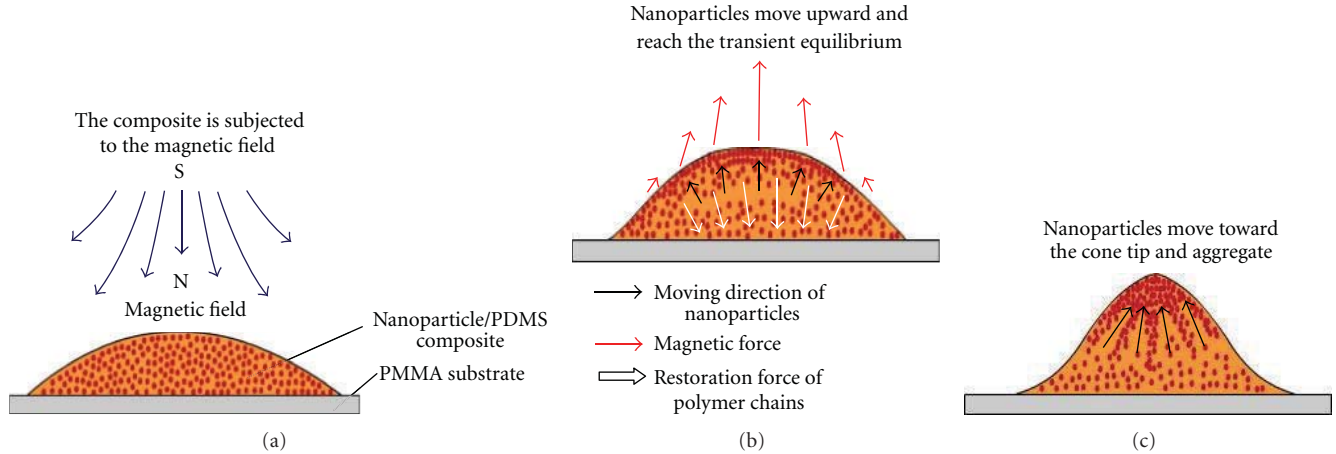


FIGURE 11: Illustration of the mechanism of the composite deformation.

comparison to the rim region. Therefore, a darker color around the cone tip is observed. Before the nanoparticle/PDMS composite is cured, the nanoparticles are allowed to move in the PDMS. As soon as the PDMS is cured, the nanoparticles cannot move anymore. This results in the gradient magnetism due to the nonuniform distribution of the nanoparticles. Originally, the nanoparticles distribute uniformly in the PDMS. Then the magnetic field on the droplet attracts the nanoparticles which are closer to the droplet surface. These nanoparticles move upward, causing the PDMS to deform as illustrated in Figure 11(a). The momentum of the nanoparticles causes the PDMS to deform rapidly, and hence, the initial slope in Figure 8(a) is steep. When the magnetic force and the restoration force of the polymer chains reach transient equilibrium, the speed of deformation becomes slower, as illustrated in Figure 11(b). Although it is in equilibrium at 5 s in Figure 8(a), the height increase reduces the distance between the magnet and the top of the droplet. Therefore, the magnetic force exerting on the nanoparticles which are close to the droplet surface increases. Nevertheless, the nanoparticles are insufficient to cause rapid deformation of the PDMS. Hence the slope becomes smaller for the process time during 5~25 s. Since the top of the droplet is subjected to a relatively stronger magnetic force, the nanoparticles in the internal portion of the droplet will move to the surface gradually and then accumulate on top of the droplet, in the center of the drop top, as illustrated in Figure 11(c). When the nanoparticles are sufficient and the droplet reaches the appropriate height, the droplet deformation becomes more rapid for the process time during 25~30 s in Figure 8(a). The nanoparticles keep moving to the droplet top and hence the PDMS deformation concentrates at the top of the droplet until the cone shape is obtained. The more nanoparticles in the PDMS, the stronger magnetism the cured cone has. However, the shorter magnetic height would cause the cone to touch the magnet. The 6.38% nanoparticles with the 1.5 mm magnetic height are the optimum parameters in this study and hence are used in the following fabrication of the microfluidic chip.

Figure 12 shows the deformation process for the 10.2% nanoparticles at 0, 10, and 20 s in Figure 8(a). The first

TABLE 3: Reynolds numbers estimation of deionized water and glycerin.

| | Deionized water | Glycerin |
|--|-----------------------|-----------------------|
| ρ , density (kg/m^3) | 1000 | 1263 |
| v , velocity (m/s) | 2.50×10^{-3} | 2.50×10^{-3} |
| D_H , hydraulic diameter (m) | 1.05×10^{-3} | 1.05×10^{-3} |
| μ , dynamic viscosity ($\text{Pa} \cdot \text{s}$) | 8.90×10^{-4} | 0.96 |
| Re, Reynolds numbers | 2.96 | 3.45×10^{-3} |

set of the pictures (Figures 12(a)–12(c)) indicate that the cone for the 1.5 mm magnetic height is formed quickly at the process time during 20 s but it is unstable. For the process time beyond 20 s in Figure 8(a), the micro-cone will touch the magnet and then break into two parts, as shown in (Figure 12(j)). The smaller portion of the composite is attached to the magnet while the large portion remains on the substrate, as shown in Figure 12(k). The process images for the magnetic height of 1.75 mm are shown in Figures 12(d)–12(f). The cone is formed gradually but cannot be clearly observed for the process time shorter than 20 s. The process images for the magnetic height of 2.0 mm are shown in Figures 12(g)–12(i). The composite barely deforms at this magnetic height because the magnetic force is not strong enough to overcome the restoration force of the polymer chains.

6. Microrchannel Mixing Test

In order to enhance the mixing efficiency, three nanoparticle/PDMS micro-cones are fabricated in the microchannel. Two kinds of the fluids, deionized water and glycerin, are used for microchannel mixing test. The width of the channel is 2 mm, the height of channel is 1.1 mm, the hydraulic diameter is calculated as 1.05 mm, and the flow rate is set as 10 mL/h. The Reynolds numbers, $Re = \rho v D_H / \mu$, of these two fluids are listed in Table 3. In the same condition of the diameters of the channel and the flow rate, however, the Reynolds numbers are different mainly due to variations in the dynamic viscosity, μ . Figures 13(a) and 13(b) show

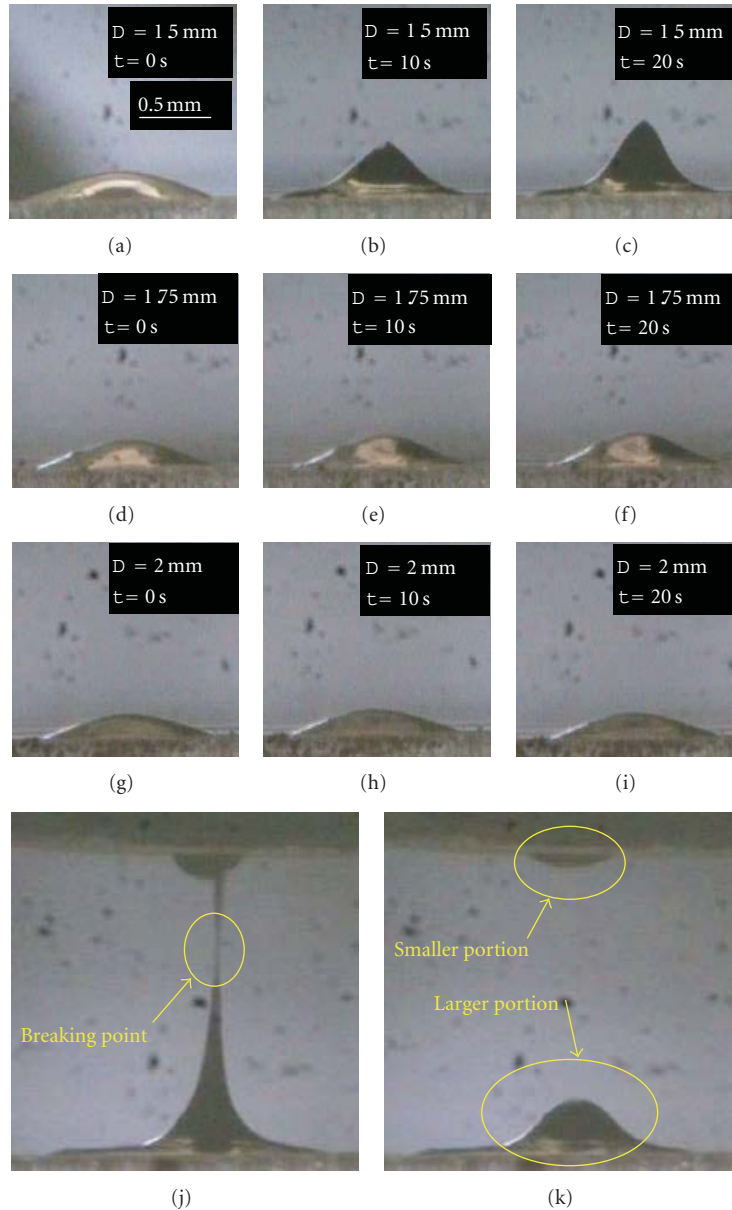


FIGURE 12: The process of the nanoparticle/PDMS droplet becomes a cone shape. The weight ratio of the nanoparticles is 10.2%. (a) $D = 1.5$ mm, $t = 0$ s. (b) $D = 1.5$ mm, $t = 10$ s. (c) $D = 1.5$ mm, $t = 20$ s. (d) $D = 1.75$ mm, $t = 0$ s. (e) $D = 1.75$ mm, $t = 10$ s. (f) $D = 1.75$ mm, $t = 20$ s. (g) $D = 2.0$ mm, $t = 0$ s. (h) $D = 2.0$ mm, $t = 10$ s. (i) $D = 2.0$ mm, $t = 20$ s. (j) $D = 1.5$ mm. The composite which expands between the substrate and the magnetic is about to break. (k) $D = 1.5$ mm. The composite breaks into two parts.

the fluidic test of deionized water without and with micro-cone, respectively. Because the Reynolds number is 2.96, which is not low enough, the laminar phenomenon is not obvious. Different diffusion results across the interface between the two fluids are also observed under different Reynolds numbers. In Figure 13(a) without the micro-cone, the distribution of the red-ink water crosses the whole channel width at a relatively downstream location as marked by the line A. In Figure 13(b) with the micro-cones, the distribution of the red-inked water crosses the whole channel width at a relatively upstream location as marked by the line B. The result demonstrates that the micro-cones effectively enhanced the mixing efficiency. Figures 13(c) and 13(d)

show the fluidic test of glycerin and the Reynolds number is 3.45×10^{-3} ($Re \ll 1$). The laminar phenomenon could be seen clearly in Figure 13(c). In Figure 13(d), although the red ink glycerin does not distribute across the channel width through the whole channel length, the flow field is redistributed as passing through the micro-cones and the flow of the red-inked glycerin becomes wider.

7. Magnetism of the Micro-Cones Test

Streptavidin has extremely high affinity for biotin, so the streptavidin-coated magnetic particles and fluorescently labeled biotin are combined to carry out the magnetism

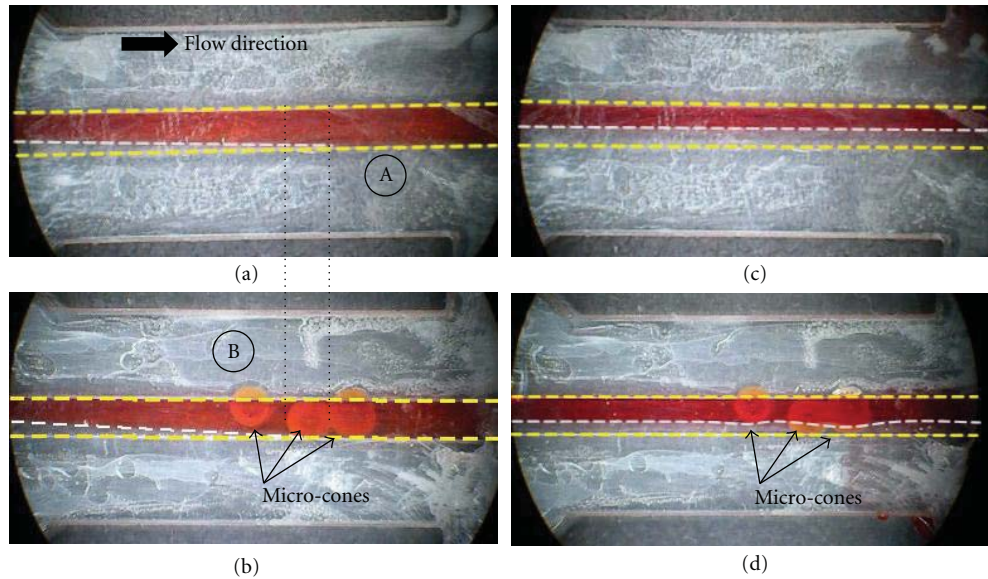


FIGURE 13: The mixing test of microchannel. (a) Deionized water in the channel without micro-cone. (b) Deionized water in the channel with three micro-cones. (c) Glycerin in the channel without micro-cone. (d) Glycerin in the channel with three micro-cones. The flow direction is from the left to the right.

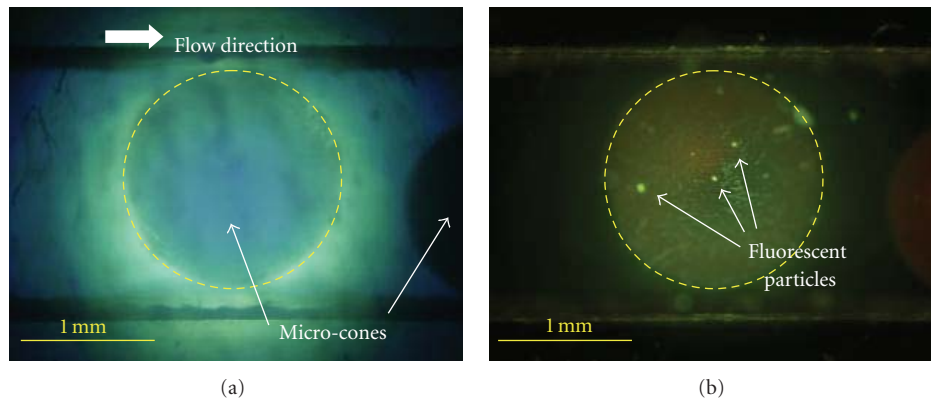


FIGURE 14: The magnetism test indicates that the micro-cone has magnetic polarity. (a) Top view of the micro-cone observed under fluorescence microscope without blue light filter. (b) The fluorescent particles captured by the micro-cone, observed under fluorescence microscope with blue light filter.

of the micro-cones test. The $50\ \mu\text{L}$ of streptavidin-coated magnetic particles (Dynabeads M-270 streptavidin, Invitrogen, $2.8\ \mu\text{m}$ in diameter, $10\ \text{mg/mL}$) are mixed with $1\ \text{mL}$ of biotin which were labeled with fluorescence (Biotin-4-fluorescein, Molecular Probes, Invitrogen) at $20\ \mu\text{g/mL}$ in concentration for 30 min. In the beginning, the deionized water is injected in and full of the microchannel to expel air. The reagent is continued to flow into the microchannel at $5\ \text{mL/h}$ flow rate. Then, the deionized water is used to wash the reagent out of the channel. The chip is mounted on a fluorescence microscope (BX51, Olympus, Japan), and the images are taken by CCD camera. Figure 14(a) shows the microchannel full of reagent, which is observed under the microscope without the blue light filter. Figure 14(b) is the same location of the microchannel as Figure 14(a) but is observed by microscope with blue light filter. The fluorescent particles captured on the micro-cone are observed. In order

to confirm that the particles are truly attracted on the micro-cone, the deionized water is used to wash the channel again. The particles still remain on the micro-cone after the wash, which proves that the iron(III)-oxide nanoparticle/PDMS cone has the magnetism and could be used in capturing magnetic particles.

8. Conclusion

An approach to fabricate the 3D iron(III)-oxide nanoparticle/PDMS cone in a microchannel has been demonstrated. The 6.38% weight ratio of the nanoparticles in the PDMS was used. An automatic dispenser was used to align the composite cone in the microchannel and to control the diameter of the composite droplet. The dispensing pressure is $0.25\ \text{MPa}$, and the dispensing time is 5 s. A permanent magnet connected to the vertical manipulation stage was

used to attract the droplet to form the cone shape. The distance between the magnet and the PMMA substrate is 1.5 mm. The cone is cured by heating at 70°C for 30 mins.

The micro-cone has been successfully fabricated in the microchannel. The height of the cone is 300 μm , and the deviated location of the cone from the central line of the microchannel is 0.3 mm. The cone has the magnetism due to the arrangement of the nanoparticles and can enhance the mixing efficiency. The fabricated cone in the microchannel could be applied in lab on a chip in the future.

Conflict of Interests

The authors do not have any conflict of interests in this present work.

Acknowledgment

This work has been sponsored by the National Science Council, Taiwan under the Contract no.: NSC 99-2221-E-002-193-MY3.

References

- [1] A. D. Stroock, S. K. W. Dertinger, A. Ajdari, I. Mezić, H. A. Stone, and G. M. Whitesides, "Chaotic mixer for microchannels," *Science*, vol. 295, no. 5555, pp. 647–651, 2002.
- [2] Y. Z. Liu, B. J. Kim, and H. J. Sung, "Two-fluid mixing in a microchannel," *International Journal of Heat and Fluid Flow*, vol. 25, no. 6, pp. 986–995, 2004.
- [3] H. J. Sheen, C. J. Hsu, T. H. Wu, H. C. Chu, C. C. Chang, and U. Lei, "Experimental study of flow characteristics and mixing performance in a PZT self-pumping micromixer," *Sensors and Actuators A*, vol. 139, no. 1-2, pp. 237–244, 2007.
- [4] A. P. Sudarsan and V. M. Ugaz, "Fluid mixing in planar spiral microchannels," *Lab on a Chip*, vol. 6, no. 1, pp. 74–82, 2006.
- [5] M. Zhang, J. Wu, L. Wang, K. Xiao, and W. Wen, "A simple method for fabricating multi-layer PDMS structures for 3D microfluidic chips," *Lab on a Chip*, vol. 10, no. 9, pp. 1199–1203, 2010.
- [6] S. G. Grancharov, H. Zeng, S. Sun et al., "Bio-functionalization of monodisperse magnetic nanoparticles and their use as biomolecular labels in a magnetic tunnel junction based sensor," *The Journal of Physical Chemistry B*, vol. 109, no. 26, pp. 13030–13035, 2005.
- [7] M. A. M. Gijs, "Magnetic bead handling on-chip: new opportunities for analytical applications," *Microfluidics and Nanofluidics*, vol. 1, no. 1, pp. 22–40, 2004.
- [8] A. Sandhu, H. Handa, and M. Abe, "Synthesis and applications of magnetic nanoparticles for biorecognition and point of care medical diagnostics," *Nanotechnology*, vol. 21, no. 44, Article ID 442001, 2010.
- [9] A. R. Kose and H. Koser, "Ferrofluid mediated nanocytometry," *Lab on a Chip*, vol. 12, no. 1, pp. 190–196, 2012.
- [10] N. Pamme and C. Wilhelm, "Continuous sorting of magnetic cells via on-chip free-flow magnetophoresis," *Lab on a Chip*, vol. 6, no. 8, pp. 974–980, 2006.
- [11] S. A. Peyman, A. Iles, and N. Pamme, "Mobile magnetic particles as solid-supports for rapid surface-based bioanalysis in continuous flow," *Lab on a Chip*, vol. 9, no. 21, pp. 3110–3117, 2009.
- [12] T. Zhu, F. Marrero, and L. Mao, "Continuous separation of non-magnetic particles inside ferrofluids," *Microfluidics and Nanofluidics*, vol. 9, no. 4-5, pp. 1003–1009, 2010.
- [13] K. S. Kim and J. K. Park, "Magnetic force-based multiplexed immunoassay using superparamagnetic nanoparticles in microfluidic channel," *Lab on a Chip*, vol. 5, no. 6, pp. 657–664, 2005.
- [14] S. S. Shevkoplyas, A. C. Siegel, R. M. Westervelt, M. G. Prentiss, and G. M. Whitesides, "The force acting on a superparamagnetic bead due to an applied magnetic field," *Lab on a Chip*, vol. 7, no. 10, pp. 1294–1302, 2007.
- [15] C. Pascal, J. L. Pascal, F. Favier, M. L. E. Moubtassim, and C. Payen, "Electrochemical synthesis for the control of $\gamma\text{-Fe}_2\text{O}_3$ nanoparticle size, morphology, microstructure, and magnetic behavior," *Chemistry of Materials*, vol. 11, no. 1, pp. 141–147, 1999.
- [16] W. H. Binder, H. Weinstabl, and R. Sachsenhofer, "Superparamagnetic ironoxide nanoparticles via ligand exchange reactions: organic 1,2-diols as versatile building blocks for surface engineering," *Journal of Nanomaterials*, vol. 2008, Article ID 383020, 10 pages, 2008.
- [17] C. Zhang and X. Xie, "Controllable assembly of hydrophobic superparamagnetic iron oxide nanoparticle with mPEG-PLA copolymer and its effect on MR transverse relaxation rate," *Journal of Nanomaterials*, vol. 2011, Article ID 152524, 7 pages, 2011.
- [18] G. Filipcsei and M. Zrínyi, "Magnetodeformation effects and the swelling of ferrogels in a uniform magnetic field," *Journal of Physics Condensed Matter*, vol. 22, no. 27, Article ID 276001, 2010.

Research Article

Analysis of Gas Permeability Characteristics of Poly(Lactic Acid)/Poly(Butylene Succinate) Nanocomposites

Amita Bhatia,¹ Rahul K. Gupta,¹ Sati N. Bhattacharya,¹ and Hyoung Jin Choi²

¹ Rheology and Materials Processing Centre, School of Civil, Environmental and Chemical Engineering, RMIT University, Melbourne, VIC 3001, Australia

² Department of Polymer Science and Engineering, Inha University, Incheon 402-751, Republic of Korea

Correspondence should be addressed to Rahul K. Gupta, rahul.gupta@rmit.edu.au and Hyoung Jin Choi, hjchoi@inha.ac.kr

Received 29 June 2012; Revised 13 September 2012; Accepted 13 September 2012

Academic Editor: Suprakas Sinha Ray

Copyright © 2012 Amita Bhatia et al. This is an open access article distributed under the Creative Commons Attribution License, which permits unrestricted use, distribution, and reproduction in any medium, provided the original work is properly cited.

Gas permeability and morphological properties of nanocomposites prepared by the mixing of poly(lactic acid) (PLA), poly(butylene succinate) (PBS), and clay was investigated. While the composition of PLA and PBS polymers was fixed as 80% and 20% by weight, respectively, for all the nanocomposites, clay contents varied from 1 to 10 wt%. From the morphological studies using both wide angle X-ray diffraction and transmission electron microscopy, the nanocomposite having 1 wt% of clay was considered to have a mixed morphology of intercalated and delaminated structure, while some clusters or agglomerated particles were detected for nanocomposites having 3 and more than 3 wt% of clay content. However, the average particle size of the dispersed PBS phase was reduced significantly from 7 μm to 30–40 nm with the addition of clay in the blend. The oxygen barrier property was improved significantly as compared to the water vapor. A model based on gas barrier property was used for the validation of the oxygen relative permeabilities of PLA/PBS/clay nanocomposites. PLA/PBS/clay nanocomposites validated the Bharadwaj model up to 3 wt% of clay contents only, while for nanocomposites of higher clay contents the Bharadwaj model was invalid due to the clusters and agglomerates formed.

1. Introduction

Polymer/organically modified layered silicate nanocomposites have attracted much attention in the past few decades because of their demonstrated significant enhancement of a large number of the properties including barrier, thermal, mechanical, rheological, flammability resistance, and other physical properties relative to an unmodified silicate or neat polymer resin. These improvements are mainly achieved at lower silicate loadings (≤ 5 wt%), which result in a high aspect ratio along with a large surface area. The concentration of silicate loading required for the preparation of nanocomposites is a fraction of what is typically required with conventional composites. Moreover, the improvement in these nanocomposites is matchable or higher than those for the conventional composites regarding the filler content. Till now, various nanocomposites have been developed and

are being developed using layered silicate clay minerals as a reinforcing phase due to its easy and abundant availability, low cost, and, more importantly, environmental friendliness [1].

The rapid growth of the use of plastics in our daily life has become an important issue due to the resulting global environmental problems. Generally, polyethylene, polypropylene, polystyrene, poly(vinyl chloride), and so forth are the most produced, used, and then discarded in the environment. Especially, their packaging materials end up as dangerous, undegradable wastes. Due to the unavailability of satisfactory landfill sites, production of large amounts of carbon dioxide and toxic gases during incineration, which again contribute to the environmental pollution, and the more expensive and reduced quality of recycled plastic products, there has been a drive to concentrate on

biodegradable polymeric materials. Keeping these reasons in mind, the development of biodegradable materials with superior properties has become a challenging and interesting subject for researchers, scientists, and engineers throughout the world today. It is expected that, like other polymer nanocomposites, biodegradable polymer-nanocomposites will also demonstrate great enhancements in physical and material properties. Therefore, these biodegradable nanocomposites may become a possible solution for the global environmental problem caused by plastic wastes.

Various researchers [2, 3] have studied biodegradable polymers which are derived from renewable and petroleum resources; these include poly(L-lactide) (PLA), poly(butylene succinate) (PBS), poly(butylene adipate terephthalate), poly(ethylene terephthalate succinate), and poly(ϵ -caprolactone). The PLA, which is produced from a feedstock of corn rather than petroleum, has recently been used for packaging material. Packaging material for food should provide sufficient barriers against water vapour to prevent the food degradation, against atmospheric gases to prevent the oxidation of the food material, and against volatile organic compounds to preserve the aromas and the flavors of the food [4]. In food packaging, mass transfer both from the food to the polymer and vice-versa is responsible for the contamination of food and also causes degradation of the packaging material. Since the PLA is produced from a lactide monomer coming from a lactic acid which is a nontoxic substance already found in the human body, food contamination can be neglected when the PLA is used as a packaging material. Therefore, it can be assumed that the determination of permeability of oxygen, water vapour, and aromas in PLA used for food packaging material is an important parameter.

PLA is a linear thermoplastic polyester. It has good mechanical properties, thermal plasticity, and good biocompatibility and it can be easily fabricated. However, the cost associated with the ring-opening polymerization of lactide monomer and brittleness of the PLA limit the commercial use of PLA polymer. Therefore, blending of PLA with another biodegradable polyester polymer may be necessary such that the resultant blend would overcome the limitations of PLA achieving good qualities by the addition of another polymer and also reduced the final cost.

In this study, the polymer selected to blend with PLA was PBS which is one of the most promising polymers in the family of synthetic biodegradable polyesters. PBS, chemically synthesized by the polycondensation of 1, 4-butanediol with succinic acid [5], has high flexibility, excellent impact strength, and thermal and chemical resistance [6]. Excellent processability of the PBS might make processability PLA better. Among various physical characteristics, gas permeability properties of the nanocomposites are mainly focused and then correlated with their morphological properties from both XRD and TEM.

2. Background of Gas Barrier Modeling

Theoretical models have been developed for predicting the properties of composite materials based on the properties of

the pure components and the morphology of the composite. The general objective of such theories has been to predict the performance of the composite for a given set of components [7]. These theories enable a simple route for evaluation of the individual contribution of the component's properties, such as matrix type, volume fraction, filler aspect ratio, filler orientation, and filler distribution. Various studies [8, 9] have shown that aspect ratio and particle distribution in the polymer matrix are important factors for predicting the properties of polymer nanocomposites; suitable values help in achieving high enhancement in properties of nanocomposites.

Enhancements of various properties are well known in polymer-silicate nanocomposites; their main dependence is on the distribution of the silicate layers in the polymer matrices. However, the main factors behind the improvement in gas barrier properties are not yet fully understood. As clays are crystalline materials, they are believed to increase the barrier properties by creating a maze or "tortuous path" that restricts the progress of the gas molecules to pass through the polymer matrices [10]. Note that the idea of "tortuosity" has been already introduced by Michaels and Parker [11] accounting for the impedance to flow offered by the irregular intercrystallite passages of polyethylene.

Nielsen [10] developed a theory for diffusion through filled polymer systems. According to this theory, if the fillers are impenetrable to a diffusing gas or liquid molecule, then the diffusing molecule must go around the filler particles. He utilized the tortuosity factor (τ) which is defined as the ratio of the actual distance (d') that a penetrant must travel to the shortest distance (d) that it would have travelled in the absence of the layered silicate. Nielsen added that thin, plate-like fillers, having a large aspect ratio ($L/2W$) (where L is the length of the filler particle and W is the width of the filler plates), can dramatically reduce the permeability only if the particles are oriented in such a way that their flat surfaces are parallel to the surfaces of the film. Nielsen also stressed that incomplete filler dispersion, voids, and only partial orientation of the particles should result in a reverse affect on permeability. The tortuosity factor (τ) is expressed as

$$\tau = \frac{d'}{d} = 1 + \frac{L}{2W} \phi_s, \quad (1)$$

where ϕ_s is the volume fraction of the sheets.

The effect of tortuosity on the permeability can be expressed as

$$\frac{P_s}{P_p} = \frac{1 - \phi_s}{1 + L/2W \phi_s}, \quad (2)$$

where P_s and P_p represent the permeabilities of the nanocomposite and neat polymer, respectively.

Bharadwaj [12] invoked a simple model, developed earlier by Nielsen, correlating the sheet length, concentration, relative orientation, and state of aggregation of the filler in the polymer matrix. This model gave further guidance in the design of better barrier materials for nanocomposites. Bharadwaj [12] predicted, from (2), that the relative

permeability (P_s/P_p) is a function of the silicate sheet length. The relative permeability of H₂O in a polyimide-montmorillonite nanocomposite reproduced the proposed concentration dependence according to (2) [13], showing a progressive decrease in relative permeabilities as a function of increasing concentration and sheet length. Extremely large length-to-thickness ratio of the silicate sheets (30 to ~2000 nm in length, 1 nm thick) showed a significant increase in tortuosity. It is interesting to note that no significant reduction in the relative permeability was noticed, regardless of the clay sheet length, beyond $\Phi_s = 0.05$. This is also in agreement with experimental observations [13–18].

Bharadwaj modified the tortuosity factor to include the orientational order (S), writing the relative permeability as follows:

$$\frac{P_s}{P_p} = \frac{1 - \phi_s}{1 + (L/2W)\phi_s(2/3)(S + 1/2)}. \quad (3)$$

The above expression reduces to (2) when $S = 1$ (planar arrangement, i.e., maximum tortuosity) and provides approximately the permeability of the neat polymer when $S = -1/2$ (orthogonal arrangement). Further, Bharadwaj concluded that incorporating sheets with $L > 500$ nm with random orientation was more beneficial for the barrier properties than the case where the sheets were aligned perpendicular to the diffusing path.

Exfoliation appears to be the critical factor in determining the maximum performance of polymer nanocomposites for barrier applications. A significant decrease in the permeability of O₂ gas through the near exfoliated PLA-nanocomposite relative to the neat polymer (PLA) was clearly observed [8]. Nielsen [10] explained that at $L = 1000$ nm the relative permeability was ~0.05 for $W = 1$ nm and 0.2 for $W = 7$ nm. While for $L = 500$ nm, relative permeability changed from 0.1 to 0.3, respectively, for $W = 1$ to 7 nm, thus underscoring the need for complete delamination of the silicate sheets.

Messersmith and Giannelis [19] observed a dramatic reduction in water permeability through composite films of poly(epsilon caprolactone)/organically modified mica-type silicate containing modest amounts of silicate. This reduction was due to the dispersion of impermeable, high aspect ratio silicate layers within the polymer matrix. On the other hand, Cava et al. [20] compared the barrier properties of biodegradable plastics and their nanocomposites with PET for food packaging applications. Biodegradable materials showed higher oxygen permeability compared to PET at 21°C and 40% relative humidity; however, their nanocomposites demonstrated marginally lower permeability to the test gas than the neat polymer.

Both the Nielsen [10] and Bharadwaj [12] models are based on arguments related to the tortuosity factor. Further, equations related to the permeability and tortuosity were developed to understand the diffusion of small molecules in conventional composites; however, they do extremely well in predicting and relating the experimental results for the relative permeability in polymer/layered silicate nanocomposites. The main assumption of the above models is that the sheets are oriented, such that the sheet normal is

coincident with the direction of diffusion ($S = 1$). Clearly, this arrangement results in the highest tortuosity. Any deviation from this arrangement would lead to deterioration in the barrier properties. Also, a sheet-like morphology ($W = 1$) is particularly efficient at maximizing the path length of the penetration due to the large length-to-width ratio compared to spheres or cubes.

The purpose of this research was to better understand the influence of clay concentration on the gas barrier properties and morphology of biodegradable nanocomposites of PLA/PBS/C30BX (an experimental grade related to Cloisite 30B) nanocomposites having a fixed composition of PLA and PBS, at 80 wt% and 2 wt%, respectively, with various clay loadings. Various aspects of selected morphological, oxygen, and water vapour permeability properties of the nanocomposites were compared to those of the polymer blend without clay. In particular, this study mainly aimed to obtain an extensive understanding of the gas barrier properties of biodegradable polymer nanocomposites using the Bharadwaj model based on detailed morphological analysis from TEM images. Comparison of oxygen relative permeabilities obtained through experimental investigations with relative permeabilities calculated from the Bharadwaj model was done. Bharadwaj model predictions were also discussed in terms of the morphological structure of the nanocomposites reanalyzed from TEM images reported [21].

3. Experimental

3.1. Materials. Both biodegradable poly(lactic acid) (4032D-grade, Nature Works, Cargill Dow LLC) and poly(butylene succinate) (PBS) (grade G4460, Ire Chem. Co., Republic of Korea) were used in this study for blending. Densities of PLA and PBS were 1.240 g/cm³ and 1.230 g/cm³, respectively. The PLA had crystalline melting point range between 150 and 170°C, while PBS had a melting range between 95 and 114.7°C. Furthermore, an experimental grade of Cloisite 30B (SCPX 3016, Southern Clay Products (SCP) Inc., USA) organoclay, indexed as C30BX, was used. The experimental grade clay is known to provide better dispersion in biodegradable polymers, such as PLA and PBS matrices, as compared to the commercially used C30B. This clay has basically the same chemical treatment as C30B but it was achieved via a different mechanism. The C30BX, was produced by a cation exchange reaction whereby natural MMT (Na⁺-MMT) was chemically modified with bis-(2-hydroxyethyl) methyl (hydrogenated tallow alkyl) ammonium cations (C₁₈H₃₇)-N⁺(C₂H₄OH)₂CH₃).

3.2. Preparation of PLA/PBS/Clay Nanocomposites. Before processing through an extruder, the pellets of both PLA and PBS were first dried in a vacuum oven at a temperature of 50°C for 48 h to remove moisture. Drying of these polymers is very essential as moisture in these polymers induces in hydrolytic chain scission during the processing at high temperature. All the PLA/PBS/clay nanocomposites were prepared by melt compounding using a Brabender twin-screw extruder at temperature 180°C and screw speed at

40 rpm. All the nanocomposites were passed twice through the extruder to achieve better and homogeneous mixing of all the compositions. The composition of the binary blends of the PLA/PBS was kept fixed at 80/20 (wt%/wt%) for all the nanocomposites. Nanocomposites of various clay loadings, 1, 3, 5, 7, and 10 by wt%, were prepared for the investigations in this study.

All the components were premixed in a plastic bag by tumbling well and were fed simultaneously into the extruder to maintain the overall consistency. The extruded nanocomposites were pelletized and dried again at 50°C in a vacuum oven overnight. For the determination of oxygen and water vapour transmission rates, film samples of approximately 0.3 mm thickness, obtained by compression molding at 200°C and pressure of 40 kN for 5 minutes, were used and the samples were then cooled under pressure (20 MPa) for 2–3 min. All these samples were used for morphological and gas barrier property evaluations.

3.3. Analysis of PLA/PBS/Clay Nanocomposites. To examine morphology of the nanocomposites, wide angle X-ray diffraction (WAXD) (Philips PW1847 X-ray diffractometer) was carried out with a reflection geometry and $\text{CuK}\alpha$ radiation (wavelength $\lambda = 0.154$ nm) operated at 40 kV and 30 mA within the range of scattering angles (2θ) from 1 to 10°. To investigate the internal structure and dispersion state of the nanocomposites, ultrathin sections (less than 100 nm) were microtomed using a Super NOVA instrument with diamond knife. Consequently, the ultrathin samples were investigated using a transmission electron microscopy (TEM) (Philips CM200) operated at 100-kV accelerating voltage [22].

For gas permeability study, at first oxygen permeability was examined with a MOCON Ox-Tran 2/21 instrument (Modern Controls Inc., USA) according to ASTM D3985 standard as previously described [23]. The values of oxygen permeability were obtained at 23°C and 0% RH, with the exposed area and thickness of 50 cm² and 0.3 mm, respectively. A mixture of 97% N₂ with 3% H₂ was used as a carrier gas and 99.9% oxygen was used as the test gas. The permeability of Mylar (polyester) film (MOCON manufacturer) was used to calibrate the instrument, in which the permeability of this Mylar film was already known. The film samples were placed in two test (permeability) cells. After installing the samples, a continuous flow of gas was maintained on both sides of the barrier material. Firstly, nitrogen gas was passed through both surfaces to remove any oxygen in the sample. The nitrogen on one side was then replaced by oxygen, and the nitrogen flow on the other side then swept the surface to extract any oxygen that diffused through the material. The diffusing oxygen was measured by a coulometric sensor detector that is sensitive only to oxygen. For the completion of one test after films were loaded in the test cells, it takes 12 to 16 h. Before each measurement, the samples were kept at 50°C in a vacuum oven for an overnight, at least four samples of each film for their analysis.

The water vapour transmission rate (WVTR) of each PLA/PBS/C30BX nanocomposite sample was measured

using a Modern Controls Inc. (MOCON) Permatran-W1 (USA), according to ASTM standard F 1249 at 100% relative humidity (RH) and 37.8°C temperature. The exposure area for the WVTR measurements was 50 cm² and thickness of the film sample was 0.3 mm, as above. Water vapour transmission rate through the plastic film was measured using a modulated infrared sensor. Water vapour transmission rates can be evaluated for the films by using other solutions, that is, sodium chloride, sodium acetate, and magnesium chloride giving different relative humidity (RH). In this study, very pure water (100% RH) was used as the samples did not absorb much water. Calibration of this instrument was also done using a Mylar (polyester) film of 5 mil thickness supplied by MOCON, which has a WVTR of 4.55 g/m²·day at 37.8°C and 100% RH. Test films mounted in the diffusion cell were initially exposed to a continuous flow of air across the upper side, while the bottom side was exposed to water vapour from the moistened pad (reverse osmosis water) in the humid cavity. This is called conditioning which took one night. Conditioning of the sample is required to allow the establishment of an equilibrium transmission rate. The flow rate of the air during the test was set to 60 cm³/min. After conditioning, actual water vapour transmission (WVTR) was noted, usually after 12–16 hours. An average of five values is reported in this work after normalizing the unit values according to the thickness of the sample.

4. Results and Discussion

The characteristic peak of pristine C30BX in WAXD patterns occurred at the diffraction angle 4.96°. By using Bragg's law, the *d*-spacing, also called the basal spacing, was calculated as 1.78 nm for C30BX [23]. This is in close agreement with that of commercially available C30B organoclay (i.e., 1.75 nm). The WAXD patterns of the PLA/PBS/C30BX nanocomposites from our previous work (Figure 1 [23]) demonstrated that the nanocomposite having 1 wt% of the C30BX did not show any diffraction peak in the range used, probably due to its low clay content. The nanocomposite of 3 wt% of C30BX exhibited a broad and extremely weak reflection at approximately 2° diffraction angle. Moreover, it also showed a slightly visible peak at approximately 6° diffraction angle. However, it is not sufficiently clear to be called a peak. For 5, 7, and 10 wt% of clay nanocomposites the peak shifted to lower angles at 2.3°, 2.2°, and 2.2°, respectively. This indicated that the polymer chains were intercalated into the C30BX layers. The peak for the 5 wt% sample was relatively broad. Compared to the characteristic peak of neat C30BX the gave an interlayer spacing (*d*₀₀₁) of 1.78 nm, the interlayer *d*-spacing increased to 3.84 nm, 4.01 nm, and 4.01 nm in nanocomposites having 5, 7, and 10 wt% of C30BX concentration, respectively. Shifting of the peak occurred due to the intercalation of the polymer chains into the clay galleries, while broadening of the peak in 3 and 5 wt% of polymer/clay nanocomposite indicated a distribution of intercalated layer spacings. Krikorian and Pochan [24] revealed that the broadening of the peak can also occur due to the partial disruption of parallel stacking

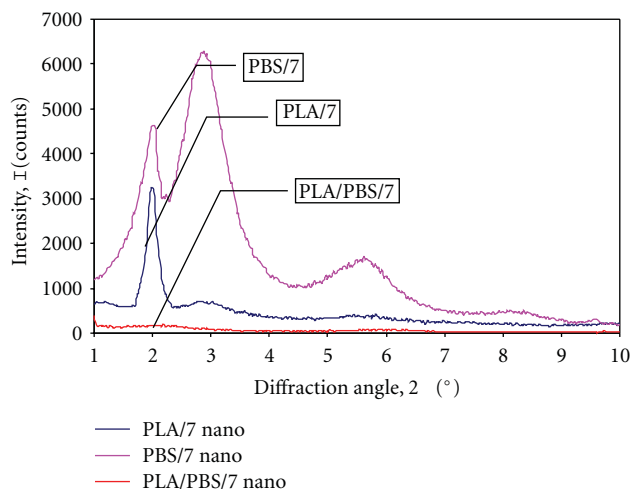


FIGURE 1: WAXD profiles of PLA/PBS/C30BX, PLA/C30BX, and PBS/C30BX nanocomposites. The content of C30BX was 7 wt% in all these nanocomposites.

or layer registry of the pristine organoclay, which means the existence of some delamination of clay platelets. Therefore, it can be concluded that a mixture of delaminated and intercalated structure was observed. On the other hand, nanocomposites with 7 and 10 wt% of clay clearly demonstrated predominantly intercalated structure, in which the intensity of these intercalated clay peaks gradually increased with the addition of the clay, due to more diffracted X-rays from the parallel assembly of the additional intercalated clay [24]. Interestingly, it was noticed that for the 3, 5, 7, and 10 wt% clay, the main diffraction peaks were accompanied by the appearance of another peak at 2θ of approximately 6° , at the same location with the same basal spacing for each nanocomposite. Note that an additional small peak at a diffraction angle (2θ) below 10° for various PLA/organoclay nanocomposites has been reported [25]. Based on this assumption, the secondary peak could be correlated to the XRD spectra of the PLA and PBS polymers itself in PLA/PBS/C30BX nanocomposites.

On the other hand, the WAXD profiles of nanocomposites of PLA/7, PBS/7 and PLA/PBS/7 are shown in Figure 1. The nanocomposite of 7 wt% of C30BX clay in PLA had an increased interlayer distance of 3.08 nm ($2\theta = 2.86^\circ$), while the PBS/C30BX (93/7 wt%) nanocomposite had a clay interlayer distance of 3.06 nm ($2\theta = 2.88^\circ$), which indicated that PBS polymer also had a tendency to intercalate between C30BX layers. A better association or interaction between C30BX clay and PLA polymer could be concluded because of the larger interlayer distance of PLA/C30BX nanocomposite than that of PBS/C30BX nanocomposite. It was interesting to note further that when both PLA and PBS polymers were mixed with C30BX (PLA/PBS/C30BX: 80/20/7 wt%), intercalation occurred. On the other hand, Wang et al. [26] studied the effect of clay in polypropylene (PP)/polystyrene (PS) blends, finding that when organophilic clay montmorillonite (OMMT) was mixed with either PP or PS, the

layer distance of OMMT was around 3.2–3.3 nm. But, when both PP and PS were mixed with OMMT, the layer distance was increased further to 3.79 nm. Thus, it was concluded that both immiscible polymers intercalated between the OMMT clay layers. Lim et al. [27] and Chen et al. [28] also confirmed the intercalation of immiscible polymer blend matrices within OMMT, which is in contrast to the results obtained in this study. It is noted that Chen et al. [28] also used a blend of PLA and PBS, but normal C30B, and they did not study the barrier properties.

It can also be found from Figure 1 that the addition of PBS to the PLA/C30BX (C30BX-7 wt%) nanocomposite system shifted the basal peak towards the lower diffraction angles (2θ) from 2.86° to 2.2° for PLA/PBS/C30BX (C30BX-7 wt%). Intercalated peaks for both nanocomposites (PLA/C30BX and PBS/C30BX nanocomposites) were obtained at almost similar diffraction angles but the intensities were quite different. The characteristic peak height in PLA/C30BX nanocomposite was smaller as compared to PBS/C30BX nanocomposite. The low intensity of the peak can be explained by the tendency for delamination of C30BX in the PLA/C30BX mixture [29]. Whether C30BX has better affinity with PLA or PBS polymers can be determined by using the X-ray data of the ternary mixture. Figure 1 also showed that both PLA and PBS nanocomposites have peaks at the same diffraction angle; however, peak of PBS/C30BX nanocomposite is very sharp and has high intensity as compared to PLA/C30BX nanocomposite. This suggested that PLA chains have better affinity towards C30BX clay. Lee et al. [30] also reported similar results with biodegradable aliphatic polyester blends.

Meanwhile, our previously reported SEM image of the PLA/PBS blend of 80/20 by wt% showed that the blend was immiscible [21]. Bhatia et al. [31] noticed a clear dispersed phase of PBS in all their compositions of PLA/PBS blends while investigating the compatibility between PLA and PBS polymers and concluded that for PBS contents higher than that in the 80/20 (PLA/PBS) blends, that is, 20%, the traditional morphology of immiscible blends could be seen. A similar type of immiscible morphology trend was reported for PLA and poly(butylene succinate adipate) blends by S. Lee and J. W. Lee [32]. On the other hand, TEM can further confirm the observations and the conclusions made from the WAXD data for the PLA/PBS/C30BX nanocomposites as previously reported [21]. Nonetheless for detailed analysis of gas barrier properties using Bharadwaj model, we need to reanalyze TEM images. Figure 2 shows TEM images of the PLA/PBS/C30BX nanocomposites with various clay loadings with the images chosen to show clay rich regions. Although the WAXD pattern of the nanocomposite having 1 and 3 wt% of C30BX showed featureless diffraction, which was interpreted as a delaminated morphology, in the TEM image (Figures 2(a) and 2(b)), delaminated/intercalated and stacked structure of the silicate layers could be readily observed for both 1 and 3% clay loadings. More precisely, 1 and 3 wt% of C30BX exhibited a disordered intercalated structure of stacked silicates. Therefore, nanocomposites with 1 and 3 wt% of C30BX are expected to achieve the greater enhancement in barrier properties.

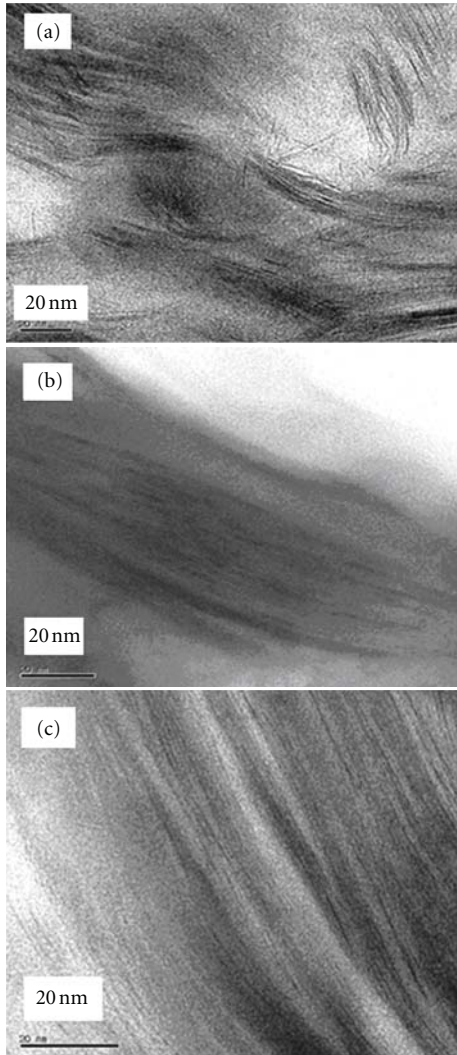


FIGURE 2: TEM images of PLA/PBS/Cloisite 30BX nanocomposites containing: (a) 1 wt%, (b) 3 wt%, and (c) 5 wt% clay. PLA/PBS ratio was 80/20 by wt% for all the nanocomposites.

Big, clear, and flocculated silicate layers tactoids can be seen in the clay content 5 wt% (Figure 2(c)) and higher contents of nanocomposites as we previously observed [21]. It can be seen that with the increase of clay concentration, the thickness of the tactoids increased. However, these tactoids themselves gain some degree of disorderliness, which may be due to the clay concentration as well as the shearing forces during the melt extrusion process in the preparation of the nanocomposite. TEM images (not shown) clearly demonstrated that the stacked and intercalated silicate layers were nicely dispersed in the PLA and PBS matrices which were supported by WAXD analysis also. A previous section proved that both polymers were intercalated between the clay layers of C30BX (refer to Figure 1).

Sheet-like platelets (clay particles) are believed to increase the gas barrier properties in nanocomposites. The barrier property improves due to the tortuous path being created by the clay particles which retards the diffusion of the gas

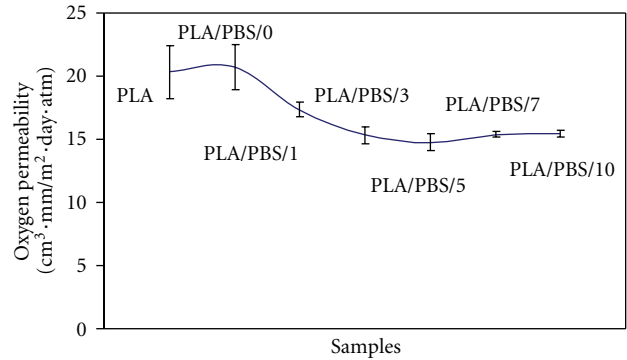


FIGURE 3: Effect of clay (C30BX) on oxygen permeability of PLA/PBS (80/20) blend and various PLA/PBS/C30BX (80/20/clay) nanocomposites of different clay loadings [23].

molecules through the matrix region. The theory behind the improvement in the gas barrier properties of the polymer layered nanocomposites was explained above.

All the nanocomposite films showed better oxygen barrier properties than neat PLA films as well as PLA/PBS blend films, as shown in Figure 3, which is previously observed [23]. Amongst all the nanocomposites, the nanocomposite having 5 wt% of C30BX content exhibited the highest reduction in oxygen permeability, approximately 26%. XRD and TEM (Figures 2(a) and 2(b)) results indicated that a mixture of exfoliated and disordered intercalated morphology occurred for 1 and 3 wt% of clay nanocomposites. However, improvement in 5 wt% of nanocomposite was the maximum. As the clay content was increased, aggregates of the clay particles formed which gave less improvement in oxygen barrier property. Research has shown that the degree of tortuosity also reflects geometrical influences like shape and state of delamination/intercalation of platelets and their orientation in the polymer matrix [12, 33–37]. For instance, Ray et al. [34] found a significant decrease in oxygen permeability for compression molded PLA nanocomposites samples, while observing some difference between the experimental value and calculated value due to the coexistence of intercalated stacked and disordered/delaminated clay layers. On the other hand, compression-molded specimens are generally known to give lower transmission rates than extruded specimens, while blown films generally show a good improvement in barrier properties [35], probably due to the fact that the biaxial orientation of silicate platelets in the polymer matrix produced during the blown film process would increase the tortuosity enough to enhance the barrier properties [36]. Therefore, the overall improvement in the barrier property was not that high because the specimens used in this study for obtaining oxygen permeability were compression molded. Nonetheless, it is interesting to note that, even though the oxygen permeability did not decrease further at higher clay contents (7 and 10 wt%) in the PLA/PBS/C30BX nanocomposites, the decrease can be considered significant in comparison to the PLA/PBS (80/20) blend due to the presence of impermeable crystalline clay particles restricting the passage of oxygen.

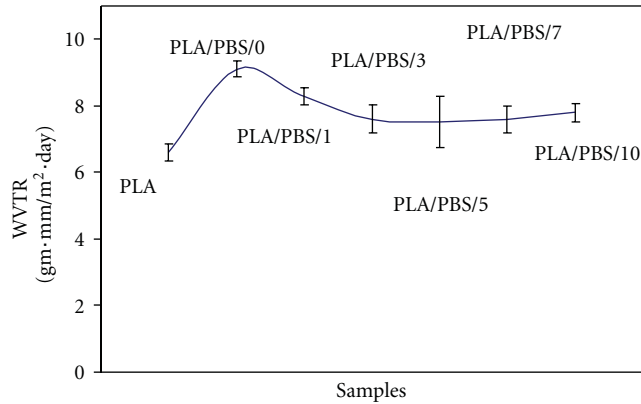


FIGURE 4: Water vapour transmission rates (WVTR) of PLA/PBS (80/20) blend and their nanocomposites (PLA/PBS/C30BX) with various loadings of C30BX organoclay.

For the relatively modest improvement of the barrier properties in their compression molded nanocomposites, Krook et al. [35] explained two reasons of the void-content, which provided means for non-diffusion transport through the film and the nonuniformity of the clay particles. The improvement of the barrier properties of PLA/PBS/C30BX nanocomposites compared to PLA and PBS blend alone prepared by compression molding was probably because of the presence of the clay which served as barriers.

The PLA/PBS/C30BX nanocomposites also exhibited a modest improvement in water vapour barrier properties relative to those of the PLA/PBS blend films. Water vapour transmission rates (WVTR) of all the samples are shown in Figure 4. Nielsen [10] and Gerlowski [37] suggested a general principle for the transportation of water vapour. They stated that water penetrates the galleries between the montmorillonite layers, forming water clusters in the nanocomposites, and does not allow the water to pass through quickly, and thus the diffusivity and the overall transport of water across the films is decreased.

In the PLA/PBS/C30BX nanocomposites, the water vapour permeation rate was not reduced as much as in the case of the oxygen permeation rate due to the hydrophilic nature of the polymers. When the PBS was added to the PLA in the ratio of 80/20 wt% (PLA/PBS), the water vapour transmission rate increased. During the transport of water through the PLA/PBS films, water first absorbed through the one side of the film and once the saturation level was attained, the water started to diffuse through the film to the other side and transportation took place. The water vapour transmission rates decreased the most, up to 18%, when only 5 wt% of C30BX was added in the binary blend. This decrease in water vapour transmission rate should be considered as quite modest, which implies that the C30BX also acted as impermeable layers which decreased the amount of tortuosity.

Note that the polymer crystalline regions in PLA and PBS polymers are considered to be impermeable to small molecules such as gases, which can lead to modifications in the final properties. It has been suggested that the presence

of the filler (clay) may nucleate [38] crystallization, which leads to an increase in degree of crystallinity. This can have a direct effect on the transport properties. The significant drop in permeability with an increased crystallinity is usually explained in two ways [39, 40]. Firstly, inclusion of impermeable crystallites decreases the amount of amorphous material through which the permeant can diffuse. Secondly, impermeable clay crystallites increase the tortuosities of the transport path. This improvement in the gas barrier properties can be attributed to the achievement of the mixed morphology suggested by XRD and TEM results and a decrease in void density. Gas barrier properties were improved due to the distribution of clay in the polymer matrix. On the other hand, regarding the effect of clay on crystallization, it was observed from our previous study using DSC that while 1 and 3 wt% of clay present in PLA/PBS/clay nanocomposites may not be enough to notice effect on crystallinity, the crystallinity was the highest for 5 wt% of clay content [23].

As discussed earlier, according to the Nielsen model [10], the permeability of the nanocomposite (P_s) is related to the permeability of the neat polymer (P_p) and the volume fraction of the sheets (Φ_s), length (L), and width (W) of the sheets (clay particles), as given in (3), when S is equal to 1. The thickness of the basic structural unit of montmorillonite is well defined and is approximately given as $W \sim 1$ nm; however, the length and width show large distribution, ranging from 100 nm to several microns depending upon the concentration of the filler in the polymer. The effective width of the sheets of the nanocomposites can change through aggregation of clay layers. As seen from (2), the volume fractions of the sheets and the sheet length and sheet width are the required parameters for the calculations of relative permeability for nanocomposites.

Importantly, two main reasons made the estimation of sheet length quite complicated. Firstly, on the micrograph images of the nanocomposites, only the projections of the particle transect were seen. Therefore, the real dimensions could not be estimated. Secondly, the features appearing on the micrograph images were not straight; therefore, a computer assisted analysis method was required [41]. Unfortunately, a fully automated image analysis was excluded, because of the poor visibility of the particles on the image. However, a semiautomated image analysis was used to estimate the sheet length of the clay particles as given in Figure 5. The volume fractions of the sheets in the nanocomposites were calculated from the weight fraction using the density (1980 kg/m^3) of C30BX.

TEM images of polymers normally consist of different shades of gray colour which primarily indicate electron density contrast through the sample. Regions of high atomic number appear dark, while those of low atomic number appear light. The discrimination between the greyish polymeric regions and the dark lines corresponding to the alumino silicate platelets was relatively easy by eye. In our semiautomated image analysis method, conversion of the original TEM photomicrograph into a black and white image was necessary.

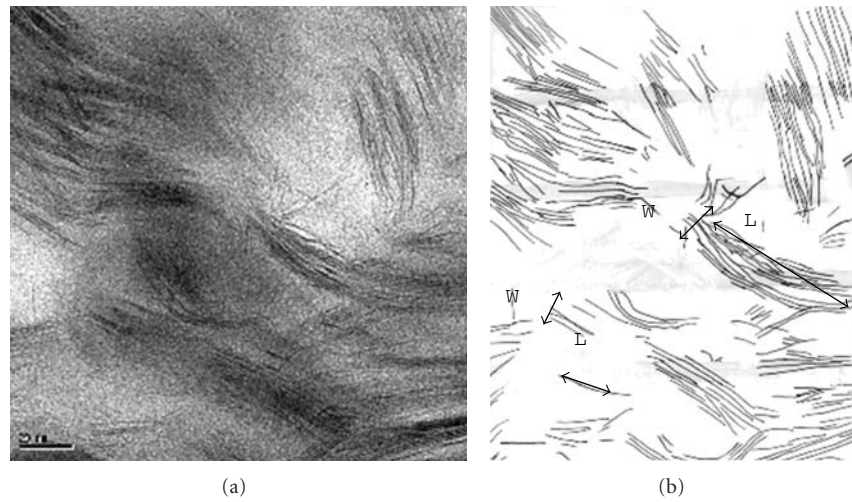


FIGURE 5: TEM (a) and its scanned image (b) of a transparent film obtained by manually tracing the particles by superimposing the film on the micrograph print. TEM image shown here is for PLA/PBS/C30BX nanocomposite containing 1 wt% of C30BX at 20 nm.

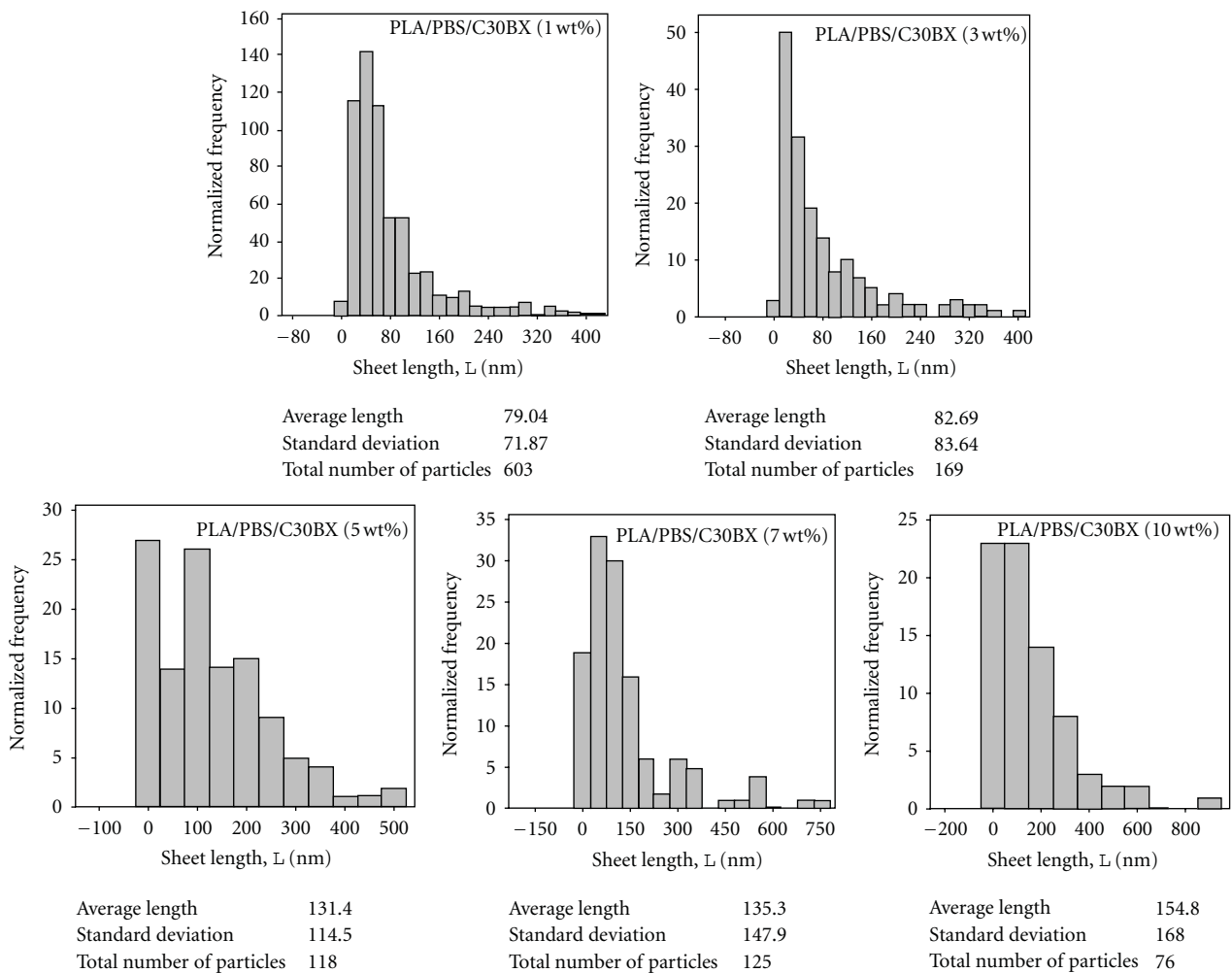


FIGURE 6: Particles length distribution for PLA/PBS/C30BX nanocomposites. Number in the bracket indicates loadings of C30BX.

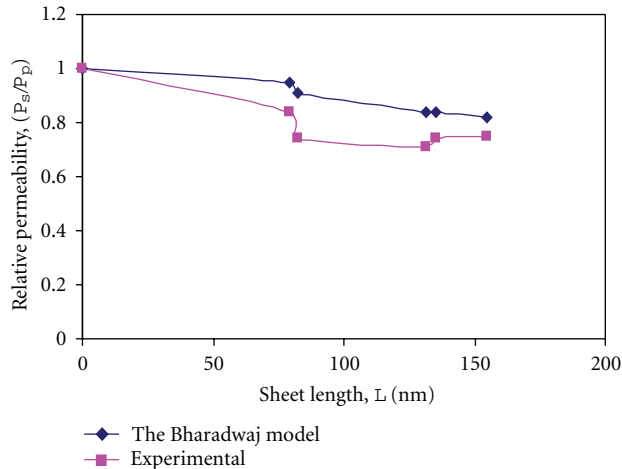


FIGURE 7: Relative permeabilities obtained from (1) and (2) taking exact values of effective width and experimental data (MOCON, oxygen permeability unit), showing the validation of the Bharadwaj model.

The semi-automated method [7] consisted of, first, manually tracing the dispersed platelets that were parallel to the beam and the agglomerates on a transparent film overlaid on the micrograph image print using a black permanent pen. The isolated platelets were considered as single platelets. The resulting transparent film was then electronically scanned and converted into a greyscale tagged-image film format (TIFF) image file. A micrograph image and its scanned image obtained by manually tracing the particles are shown in Figure 5. This greyscale image can then be converted into a black and white or binary image by using image analysis software (Scion Image Beta 4.02, Scion Corporation, USA). This software easily converts a TIFF file into a binary image and creates a duplicate of the image. From this file, the sheet lengths of the particles were calculated to obtain histograms for the various nanocomposites using Minitab 15 software.

Figure 6 shows histograms of the C30BX particle lengths and pertinent statistical data obtained on all the PLA/PBS/C30BX nanocomposites having various clay loadings. Here, the effects of clay concentration can be easily seen as sheet length increased with the addition of C30BX clay. Thus, average sheet lengths along with standard deviations were obtained. The calculated values of tortuosity and relative permeability of all PLA/PBS/C30BX nanocomposites using (2) are presented in Table 1. By comparing the relative permeabilities of oxygen obtained from the experiments and from the model, it can be seen that the experimental data very well validate the the Bharadwaj model for nanocomposites for the lower concentrations of C30BX. The nanocomposite of 1 wt% had the shortest sheet length and with the increase in clay loadings sheet length increased. At low concentrations of clay content, the clay particles were dispersed well as compared to the nanocomposites of higher content of C30BX (discussed earlier in XRD and TEM results). Therefore, lower concentration gave short clay lengths, while at higher concentrations, sheet length

started to increase. From TEM images, it was seen that as concentration of clay increased more stacks of clay particles were formed. Therefore, the effective thickness of the clay sheets (tactoids) also increased. Instead of 1 nm, it becomes 10 or 14 nm or more, depending upon the number of clay layers in the intercalated tactoids. However, here $S = 1$ (planar arrangement of silicate layers to the path of gas molecule to diffuse) was taken as assumptions while doing the calculations using the Bharadwaj model based on the clay being a gas barrier. Due to the stacking of the clay layers, now the width of the clay particles becomes effective width with the value like 6, 10, 14, 21, and 33 nm approximately for the clay loading of 1, 3, 5, 7, and 10 wt%. If these values are used in the Bharadwaj model while calculating the relative permeability, then curves for both the relative permeability of experimental and Bharadwaj model would match as shown in Figure 7.

Figure 7 shows that experimental data validated the Bharadwaj model up to a sheet length of approximately 80 nm (for 1 and 3 wt%). After that, at high sheet lengths larger and larger deviations from the Bharadwaj model were observed. The reason behind this may be that certain assumptions, like good dispersion of clay particles in the polymer matrix, $S = 1$ and $W \sim 1$ nm were used in this model. Due to agglomeration/intercalation in PLA/PBS nanocomposites, the thickness of the sheet did not remain as 1 nm. At high concentrations, thickness becomes effective thickness (effective width), which depends on the number of sheets in the stacks. The tendency of the silicate sheets to agglomerate was indeed expected to become more severe as the clay concentration increased. Due to the change in the thickness of the silicate stacks, its aspect ratio ($L/2W$) also changed and the high enhancement in gas barrier was not noted. Thus, for high content of C30BX particles, the Bharadwaj model was not validated by the experimental data of PLA/PBS/C30BX nanocomposites.

If the actual values of width instead of 1 nm were used in (2), the relative permeability of PLA/PBS/C30BX nanocomposites would validate the Bharadwaj model for all the concentrations of C30BX.

5. Conclusion

PLA/PBS/Cloisite 30BX clay nanocomposites containing 1, 3, 5, 7, and 10 wt% of clay were prepared by a melt extrusion method, and their morphology was examined using both XRD and TEM. Improvement in oxygen permeability was significantly noticed for PLA/PBS/C30BX nanocomposites with the addition of C30BX; however, the water vapour permeation rate showed only modest improvements in this system. In this study, compression molded samples were used for the determination of gas permeabilities. Due to the stacks of clay and non-uniform dispersion of clay particles, tortuosity path for the gas molecules did not increase sufficiently to make a significant improvement in gas barrier properties. PLA/PBS/C30BX nanocomposites validated Bharadwaj model for only up to 3 wt% of clay content. For higher concentrations of C30BX, deviation from

TABLE 1: Permeability parameters used to validate the Bharadwaj model. Number in the bracket indicates loadings of C30BX.

| Samples | Volume fraction, Φ_s | | Tortuosity factor, τ | Relative permeability | |
|------------------------|------------------------------|--|---------------------------|-----------------------|--------------|
| | Sheet length, L (nm) | | | Model | Experimental |
| | Width of the sheet, W (nm) | | | | |
| PLA/PBS/C30BX (0 wt%) | 0 | | 1 | 1 | 1 |
| | 0 | | | | |
| | 0 | | | | |
| PLA/PBS/C30BX (1 wt%) | 0.0065 | | 1.25 | 0.95 | 0.84 |
| | 79.04 | | | | |
| | 6 | | | | |
| PLA/PBS/C30BX (3 wt%) | 0.0187 | | 1.77 | 0.91 | 0.74 |
| | 82.69 | | | | |
| | 10 | | | | |
| PLA/PBS/C30BX (5 wt%) | 0.0314 | | 3.06 | 0.84 | 0.71 |
| | 131.4 | | | | |
| | 14 | | | | |
| PLA/PBS/C30BX (7 wt%) | 0.0443 | | 3.99 | 0.84 | 0.74 |
| | 135.3 | | | | |
| | 21 | | | | |
| PLA/PBS/C30BX (10 wt%) | 0.0625 | | 5.83 | 0.82 | 0.75 |
| | 154.8 | | | | |
| | 33 | | | | |

the Bharadwaj model was observed due to the presence of clusters and agglomerates.

Acknowledgment

The authors would like to thank Mr. Hwang Sun Jae for his valuable assistance with the transmission electron microscopy (TEM).

References

- [1] S. S. Ray and M. Okamoto, "Polymer/layered silicate nanocomposites: a review from preparation to processing," *Progress in Polymer Science*, vol. 28, no. 11, pp. 1539–1641, 2003.
- [2] D. Garlotta, "A literature review of poly(lactic acid)," *Journal of Polymers and the Environment*, vol. 9, no. 2, pp. 63–84, 2001.
- [3] T. Fujimaki, "Processability and properties of aliphatic polyesters, "BIONOLLE", synthesized by polycondensation reaction," *Polymer Degradation and Stability*, vol. 59, no. 1–3, pp. 209–214, 1998.
- [4] N. S. Oliveira, J. Oliveira, T. Gomes, A. Ferreira, J. Dorgan, and I. M. Marrucho, "Gas sorption in poly(lactic acid) and packaging materials," *Fluid Phase Equilibria*, vol. 222–223, pp. 317–324, 2004.
- [5] K. Bahari, H. Mitomo, T. Enjoji, F. Yoshii, and K. Makuuchi, "Radiation crosslinked poly(butylene succinate) foam and its biodegradation," *Polymer Degradation and Stability*, vol. 62, no. 3, pp. 551–557, 1998.
- [6] Y. Doi, "Biodegradable plastics and polymer," *Journal of Pesticide Science*, vol. 19, no. 1, pp. S11–S14, 1994.
- [7] T. D. Fornes and D. R. Paul, "Modeling properties of nylon 6/clay nanocomposites using composite theories," *Polymer*, vol. 44, no. 17, pp. 4993–5013, 2003.
- [8] S. S. Ray, K. Yamada, M. Okamoto, A. Ogami, and K. Ueda, "New polylactide/layered silicate nanocomposites. 3. High-performance biodegradable materials," *Chemistry of Materials*, vol. 15, no. 7, pp. 1456–1465, 2003.
- [9] S. S. Ray, K. Okamoto, and M. Okamoto, "Structure-property relationship in biodegradable poly(butylene succinate)/layered silicate nanocomposites," *Macromolecules*, vol. 36, no. 7, pp. 2355–2367, 2003.
- [10] L. E. Nielsen, "Models for the permeability of filled polymers systems," *Journal of Macromolecular Science, Part A*, vol. 1, no. 5, pp. 929–942, 1967.
- [11] A. S. Michaels and R. B. Parker, "Sorption and flow of gases in polyethylene," *Journal of Polymer Science*, vol. 41, no. 138, pp. 53–71, 1959.
- [12] R. K. Bharadwaj, "Modeling the barrier properties of polymer-layered silicate nanocomposites," *Macromolecules*, vol. 34, no. 26, pp. 9189–9192, 2001.
- [13] K. Yano, A. Usuki, A. Okada, T. Kurauchi, and O. Kamigaito, "Synthesis and properties of polyimide-clay hybrid," *Journal of Polymer Science, Part A*, vol. 31, no. 10, pp. 2493–2498, 1993.
- [14] E. P. Giannelis, R. Krishnamoorti, and E. Manias, "Polymer-silicate nanocomposites: model systems for confined polymers and polymer brushes," *Advances in Polymer Science*, vol. 138, pp. 107–147, 1999.
- [15] P. C. Lebaron, Z. Wang, and T. J. Pinnavaia, "Polymer-layered silicate nanocomposites: an overview," *Applied Clay Science*, vol. 15, no. 1–2, pp. 11–29, 1999.
- [16] K. Yano, A. Usuki, and A. Okada, "Synthesis and properties of polyimide-clay hybrid films," *Journal of Polymer Science, Part A*, vol. 35, no. 11, pp. 2289–2294, 1997.
- [17] E. P. Giannelis, "Polymer layered silicate nanocomposites," *Advanced Materials*, vol. 8, no. 1, pp. 29–35, 1996.
- [18] K. E. Strawhecker and E. Manias, "Structure and properties of poly(vinyl alcohol)/Na⁺ montmorillonite nanocomposites," *Chemistry of Materials*, vol. 12, no. 10, pp. 2943–2949, 2000.

- [19] P. B. Messersmith and E. P. Giannelis, "Synthesis and barrier properties of poly(epsilon-caprolactone)-layered silicate nanocomposites," *Journal of Polymer Science Part A*, vol. 33, pp. 1047–1057, 1995.
- [20] D. Cava, A. L. Rubio, L. Cabedo et al., "Comparative performance and barrier properties of biodegradable thermoplastics and nanobiocomposites versus PET for food packaging applications," in *Proceedings of the Society of Plastics Engineers Annual Technical Conference (ANTEC'05)*, pp. 83–86, May 2005.
- [21] A. Bhatia, R. K. Gupta, S. N. Bhattacharya, and H. J. Choi, "An investigation of melt rheology and thermal stability of poly(lactic acid)/poly(butylene succinate) nanocomposites," *Journal of Applied Polymer Science*, vol. 114, no. 5, pp. 2837–2847, 2009.
- [22] S. W. Ko, R. K. Gupta, S. N. Bhattacharya, and H. J. Choi, "Rheology and physical characteristics of synthetic biodegradable aliphatic polymer blends dispersed with MWNTs," *Macromolecular Materials and Engineering*, vol. 295, no. 4, pp. 320–328, 2010.
- [23] A. Bhatia, R. K. Gupta, S. N. Bhattacharya, and H. J. Choi, "Effect of clay on thermal, mechanical and gas barrier properties of biodegradable poly(lactic acid)/poly(butylene succinate) (PLA/PBS) nanocomposites," *International Polymer Processing*, vol. 25, no. 1, pp. 5–14, 2009.
- [24] V. Krikorian and D. J. Pochan, "Poly (L-lactic acid)/layered silicate nanocomposite: fabrication, characterization, and properties," *Chemistry of Materials*, vol. 15, no. 22, pp. 4317–4324, 2003.
- [25] J. H. Chang, Y. U. An, and G. S. Sur, "Poly(lactic acid) nanocomposites with various organoclays. I. Thermomechanical properties, morphology, and gas permeability," *Journal of Polymer Science Part B*, vol. 41, no. 1, pp. 94–103, 2002.
- [26] Y. Wang, Q. Zhang, and Q. Fu, "Compatibilization of immiscible poly(propylene)/polystyrene blends using clay," *Macromolecular Rapid Communications*, vol. 24, no. 3, pp. 231–235, 2003.
- [27] S. K. Lim, J. W. Kim, I. Chin, Y. K. Kwon, and H. J. Choi, "Preparation and interaction characteristics of organically modified montmorillonite nanocomposite with miscible polymer blend of poly(ethylene oxide) and poly(methyl methacrylate)," *Chemistry of Materials*, vol. 14, no. 5, pp. 1989–1994, 2002.
- [28] G. X. Chen, H. S. Kim, E. S. Kim, and J. S. Yoon, "Compatibilization-like effect of reactive organoclay on the poly(l-lactide)/poly(butylene succinate) blends," *Polymer*, vol. 46, no. 25, pp. 11829–11836, 2005.
- [29] G. Chen, X. Chen, Z. Lin, W. Ye, and K. Yao, "Preparation and properties of PMMA/clay nanocomposite," *Journal of Materials Science Letters*, vol. 18, no. 21, pp. 1761–1763, 1999.
- [30] C. H. Lee, H. B. Kim, S. T. Lim, H. J. Choi, and M. S. Jhon, "Biodegradable aliphatic polyester-poly (epichlorohydrin) blend/organoclay nanocomposites; synthesis and rheological characterization," *Journal of Materials Science*, vol. 40, no. 15, pp. 3981–3985, 2005.
- [31] A. Bhatia, R. K. Gupta, S. N. Bhattacharya, and H. J. Choi, "Compatibility of biodegradable poly (lactic acid) (PLA) and poly (butylene succinate) (PBS) blends for packaging application," *Korea Australia Rheology Journal*, vol. 19, no. 3, pp. 125–131, 2007.
- [32] S. Lee and J. W. Lee, "Characterization and processing of biodegradable polymer blends of poly(lactic acid) with poly(butylene succinate adipate)," *Korea Australia Rheology Journal*, vol. 17, no. 2, pp. 71–77, 2005.
- [33] T. C. Bissot, *Barrier Polymers and Structures*, ACS Symposium Series, American Chemical Society, Washington, DC, USA, 1989, edited by W. J. Koros.
- [34] S. S. Ray, K. Yamada, A. Ogami, M. Okamoto, and K. Ueda, "New polylactide/layered silicate nanocomposite: nanoscale control over multiple properties," *Macromolecular Rapid Communications*, vol. 23, no. 16, pp. 943–947, 2002.
- [35] M. Krook, A. C. Albertsson, U. W. Gedde, and M. S. Hedenqvist, "Barrier and mechanical properties of montmorillonite/polyesteramide nanocomposites," *Polymer Engineering and Science*, vol. 42, no. 6, pp. 1238–1246, 2002.
- [36] C. Thellen, C. Orroth, D. Froio et al., "Influence of montmorillonite layered silicate on plasticized poly(l-lactide) blown films," *Polymer*, vol. 46, no. 25, pp. 11716–11727, 2005.
- [37] L. Gerlowski, *Barrier Polymers and Structures*, ACS Symposium Series, American Chemical Society, Washington DC, USA, 1989, edited by W. J. Koros.
- [38] D. J. Sekelick, E. V. Stepanov, S. Nazarenko, D. Schiraldi, A. Hiltner, and E. Baer, "Oxygen barrier properties of crystallized and talc-filled poly(ethylene terephthalate)," *Journal of Polymer Science Part B*, vol. 37, no. 8, pp. 847–857, 1999.
- [39] W. R. Vieth, *Diffusion in and Through Polymers*, Hanser, Munich, Germany, 1991.
- [40] M. Hedenqvist and U. W. Gedde, "Diffusion of small-molecule penetrants in semicrystalline polymers," *Progress in Polymer Science*, vol. 21, no. 2, pp. 299–333, 1996.
- [41] M. Vincent, *Characterisation of exfoliation and intercalation in polymer/layered silicate nanocomposites [M.S. thesis]*, Department of Chemical Engineering, McGill University, Montreal, Canada, 2004.

Research Article

Layer-by-Layer Nanoassembly of Copper Indium Gallium Selenium Nanoparticle Films for Solar Cell Applications

A. Hemati, S. Shrestha, M. Agarwal, and K. Varahramyan

Integrated Nanosystems Development Institute (INDI), Indiana University-Purdue University Indianapolis (IUPUI), Indianapolis, IN 46202, USA

Correspondence should be addressed to S. Shrestha, sudshres@iupui.edu

Received 5 June 2012; Accepted 4 September 2012

Academic Editor: Gaurav Mago

Copyright © 2012 A. Hemati et al. This is an open access article distributed under the Creative Commons Attribution License, which permits unrestricted use, distribution, and reproduction in any medium, provided the original work is properly cited.

Thin films of CIGS nanoparticles interdigitated with polymers have been fabricated through a cost-effective nonvacuum film deposition process called layer-by-layer (LbL) nanoassembly. CIGS nanoparticles synthesized by heating copper chloride, indium chloride, gallium chloride, and selenium in oleylamine were dispersed in water, and desired surface charges were obtained through pH regulation and by coating the particles with polystyrene sulfonate (PSS). Raising the pH of the nanoparticle dispersion reduced the zeta-potential from +61 mV at pH 7 to -51 mV at pH 10.5. Coating the CIGS nanoparticles with PSS (CIGS-PSS) produced a stable dispersion in water with -56.9 mV zeta-potential. Thin films of oppositely charged CIGS nanoparticles (CIGS/CIGS), CIGS nanoparticles and PSS (CIGS/PSS), and PSS-coated CIGS nanoparticles and polyethylenimine (CIGS-PSS/PEI) were constructed through the LbL nanoassembly. Film thickness and resistivity of each bilayer of the films were measured, and photoelectric properties of the films were studied for solar cell applications. Solar cell devices fabricated with a 219 nm CIGS film, when illuminated by 50 W light-source, produced 0.7 V open circuit voltage and 0.3 mA/cm² short circuit current density.

1. Introduction

Layer-by-layer (LbL) nanoassembly is considered as one of the most precise, readily scalable, and cost-effective techniques for the thin film deposition of polymers and nanoparticles [1, 2]. Cu(InGa)Se₂ (CIGS) nanoparticles have been widely considered in thin film solar cells due to their high theoretical efficiency and tunable band gap. Typically, CIGS solar cells are fabricated using a coevaporation technique requiring a vacuum environment, and therefore resulting in higher cost [3, 4]. Manufacturing costs for CIGS-based solar cells must be reduced to make economically viable. Many researchers have focused on lowering fabrication costs through alternate, nonvacuum deposition processes, such as blade coating and spray deposition techniques [5, 6]. However, these methods do not provide sufficient and accurate film thickness and produce undesirable rough surfaces [7]. LbL processes can be used to fabricate precisely tailored thin film on various types of substrates, both rigid and flexible. In LbL nanoassembly, positive and negatively charged species are sequentially deposited on a substrate via alternate dipping

[8]. LbL nanoassembly does not require sophisticated lab facilities or precise process control, thus yields a cost-effective thin film manufacturing process.

In this study, LbL nanoassembly is utilized to deposit controlled thin films of oppositely charged CIGS nanoparticles and polymers. Film deposition and electrical characterization results are presented and discussed. Novel aspects of this research include the functionalization of CIGS nanoparticles to create stable aqueous dispersions with desired surface charges, fabrication of thin CIGS film using LbL nanoassembly, and characterization and utilization of the films for solar cell application.

2. Experimental

2.1. CIGS Nanoparticle Synthesis. CIGS nanoparticles were synthesized using copper chloride (CuCl), indium chloride (InCl₃), gallium chloride (GaCl₃), and selenium (Se) in oleylamine (OLA) solvent. OLA (70%) was heated at 200°C for 2 hours under nitrogen. Then, in nitrogen-filled glove box, 10 ml of heated OLA was added to Se and heated at 250°C

for 1 hour while being stirred. At the same time OLA was added into two different flasks containing InCl_3 and CuCl , each heated at 250°C for 30 min while being stirred. All three flasks were then mixed and GaCl_3 was added. This reaction mixture was heated at 250°C for 75 min while being stirred [9–11]. The resulting nanoparticles were washed through suspension in chloroform and precipitation by ethanol. The size of the synthesized nanoparticles was analyzed using Malvern Nanosizer, size and zeta-potential measurement instrument, and atomic force microscopy (AFM), and material composition was studied through electron dispersive spectroscopy (EDS).

CIGS nanoparticles were cleaned through sonicating in ethanol for several hours and precipitating by centrifuging at a high speed. The resulting nanoparticles were dispersed in water. Zeta-potential (ζ) of the nanoparticles dispersed in water was controlled through pH regulation by slowly adding 0.1 g/ml NaOH solution to the CIGS dispersion. In another process, CIGS nanoparticles were coated with polystyrene sulfonate (PSS) to allow the uniform dispersion in water (CIGS-PSS).

2.2. Film Fabrications and Characterization. LbL nanoassembly is based on the sequential deposition of oppositely charged polyelectrolytes or nanoparticles. LbL films can be deposited on a wide variety of rigid and flexible substrates of different shapes and sizes [8]. LbL nanoassembly of oppositely charged CIGS nanoparticles (CIGS/CIGS), CIGS nanoparticles and PSS (CIGS/PSS), and PSS-coated CIGS nanoparticles and polyethylenimine (CIGS-PSS/PEI) was conducted.

To study the film development process, LbL nanoassembly was performed on a quartz crystal microbalance (QCM) [12]. The aqueous dispersion of CIGS nanoparticles and polymers was used for the deposition through alternately dipping the substrate in oppositely charged materials. The samples were washed in deionized water following each deposition. Separate LbL films of CIGS dispersed in water at pH 7 ($\zeta = +61$ mV) and at pH 10.5 ($\zeta = -51$ mV) (CIGS/CIGS film), CIGS at pH 7 and PSS ($\zeta = -58$ mV) (CIGS/PSS film), CIGS at pH 10.5 and PEI ($\zeta = +16$ mV) (CIGS/PEI film), and CIGS coated with PSS (CIGS-PSS, $\zeta = -56.9$ mV) and PEI (CIGS-PSS/PEI film) were deposited on QCM.

To measure thickness, films were scratched using micro-manipulator probe and were analyzed using atomic force microscopy (AFM). Confocal scanning microscopy was used to take the images of the first and last layer of a CIGS-PSS/PEI film composed of 25 bilayers. The bottom layer was labelled using Invitrogen's 20 nm fluorospheres in Nile red (red-colored fluorescent dye) and the top layer was labelled using fluorescein isothiocyanate (FITC) (green-colored fluorescent dye). To study the resistivity and the photoelectric properties CIGS/CIGS, CIGS/PSS, and CIGS-PSS/PEI LbL films were deposited across a $200\ \mu\text{m} \times 58$ cm channel on indium-tin-oxide- (ITO-) coated glass substrate. The current-voltage measurements of the films were conducted using Keithly Semiconductor Characterization instrument.

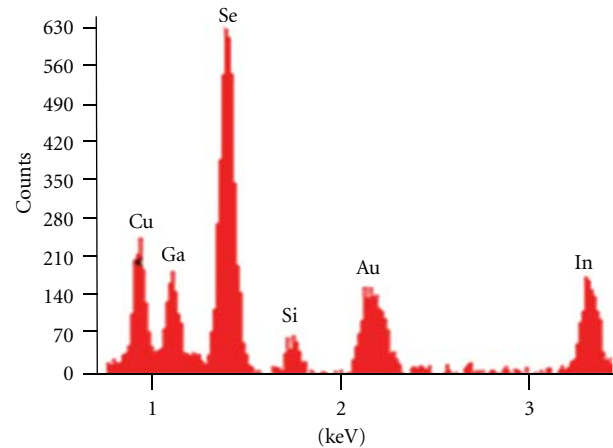


FIGURE 1: EDS results showing the material composition of CIGS nanoparticles placed on a gold-coated silicon substrate.

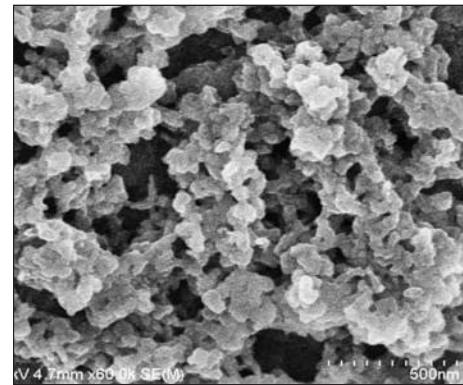


FIGURE 2: SEM image of CIGS nanoparticles in water.

The optical absorbance of a CIGS-PSS/PEI film deposited on a glass substrate was measured with ultraviolet-visible-near infrared (UV-Vis-NIR) spectroscopy.

2.3. Solar Cell Fabrications and Testing. A solar cell device consisting of CIGS-PSS/PEI absorbing layer, cadmium sulfide (CdS) n-type layer, intrinsic zinc oxide ($\text{ZnO}_2(\text{i})$) buffer layer, and aluminum-doped zinc oxide ($\text{ZnO}_2(\text{n})$) layer was fabricated and tested. A 219 nm thick CIGS-PSS/PEI LbL film was deposited on an ITO-coated glass substrate. A thin cadmium sulfide film was deposited on the CIGS-PSS/PEI through chemical bath deposition. Intrinsic zinc oxide $\text{ZnO}_2(\text{i})$ and $\text{ZnO}_2(\text{n})$ films were deposited by spin-coating of the nanopowders dispersed in isopropyl alcohol. The J/V characteristics of the solar cell were measured with the Keithly Semiconductor Characterization instrument.

3. Results and Discussion

3.1. CIGS Nanoparticles Characterization. The EDS results showing the material composition of the synthesized CIGS nanoparticles are presented in Figure 1. The gold and silicon peaks are attributed to the gold-coated silicon substrate used.

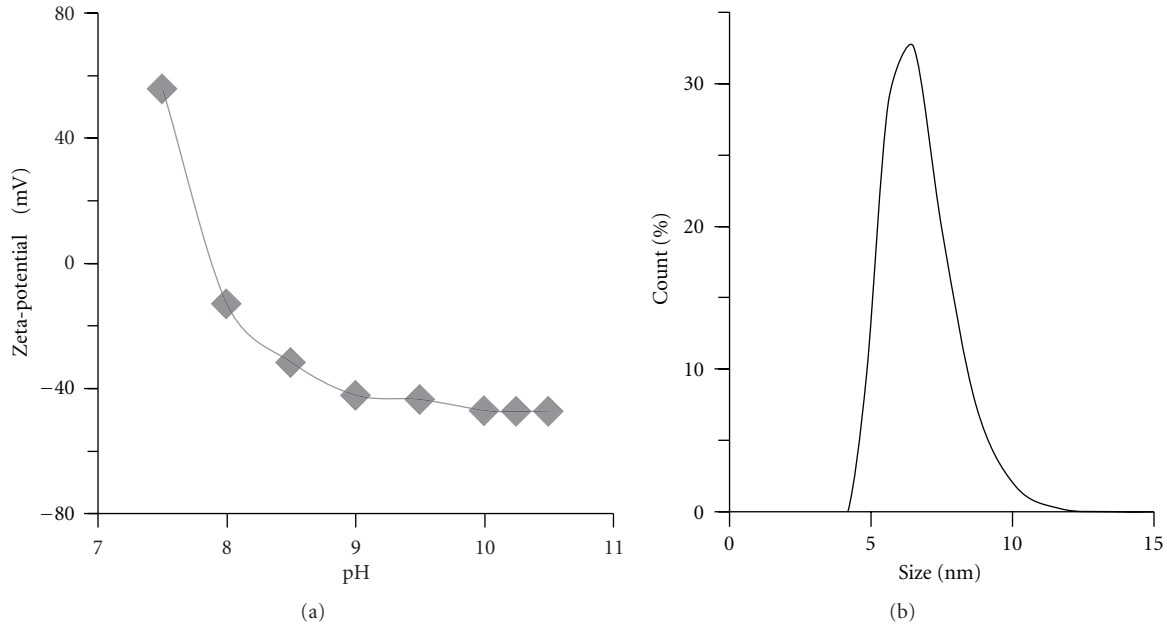


FIGURE 3: pH-dependent zeta-potential (ζ) of the CIGS nanoparticles dispersed in water. (b) CIGS-PSS nanoparticles dispersed in water.

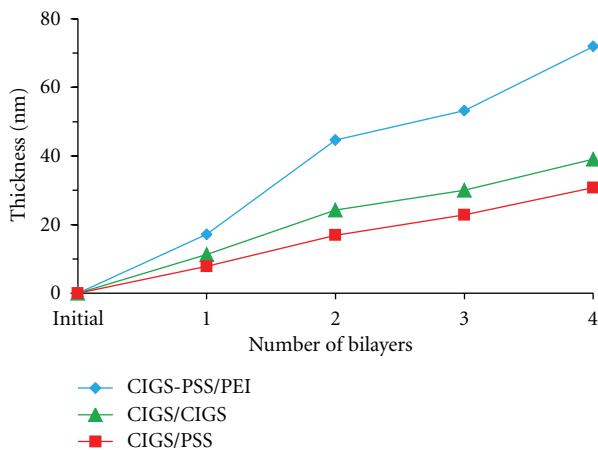


FIGURE 4: QCM results showing the film deposition of CIGS-PSS/PEI, CIGS/CIGS, and CIGS/PSS.

A scanning electron microscopy (SEM) image of the CIGS nanoparticles is shown in Figure 2. The sample for the image was prepared by drying a drop of CIGS dispersion on a gold-coated silicon substrate. It is observed that while the individual particle sizes are in 10 nm range, it forms an aggregation when dried. Zeta-potential (ζ) of the CIGS nanoparticles dispersed in water was measured to be +61 mV. The pH of the solution was raised by slowly adding 0.1 g/ml NaOH solution to the CIGS dispersion. The change in the ζ of the nanoparticles dispersed in water with increasing pH is shown in Figure 3(a). It is observed that the ζ changes from +61 mV at pH 7 to -51 mV at pH 10.5. As PSS was slowly added to the CIGS dispersed in water at pH 7, the ζ of the nanoparticles slowly decreased from

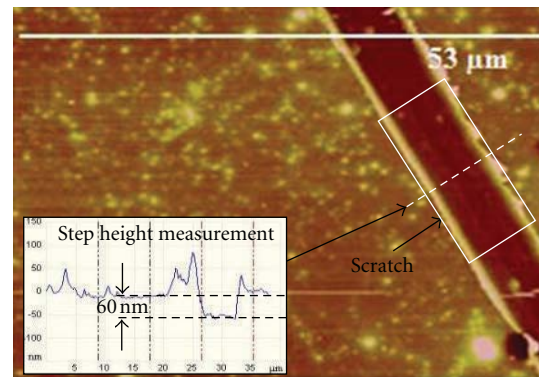


FIGURE 5: AFM image showing the top surface of a CIGS-PSS/PEI film. The inset shows the step height measurement of the scratch.

+61 mV to -56.9 mV. The size distribution of the CIGS-PSS nanoparticles in water after separating bigger particles by centrifuging the dispersion at 15000 rpm for 15 minutes is shown in Figure 3(b). The size distribution of the particle is observed to spread from 5–10 nm.

3.2. LbL Film Fabrications and Characterization. LbL film development processes of CIGS/CIGS, CIGS CIGS/PSS, CIGS/PEI, and CIGS-PSS/PEI films measured on a QCM are shown in Figure 4. The measured thicknesses after the addition of each bilayer of the films are presented. The thicknesses of 4 bilayers of CIGS/CIGS, CIGS CIGS/PSS, CIGS/PEI, and CIGS-PSS/PEI films were measured to be 31 nm, 38 nm, and 70 nm, respectively. The CIGS-PSS/PEI film shows the best film development among the three despite having good zeta-potentials of the CIGS in water at pH 7 (+61 mV) and pH 10.5 (-51 mV). The CIGS coated

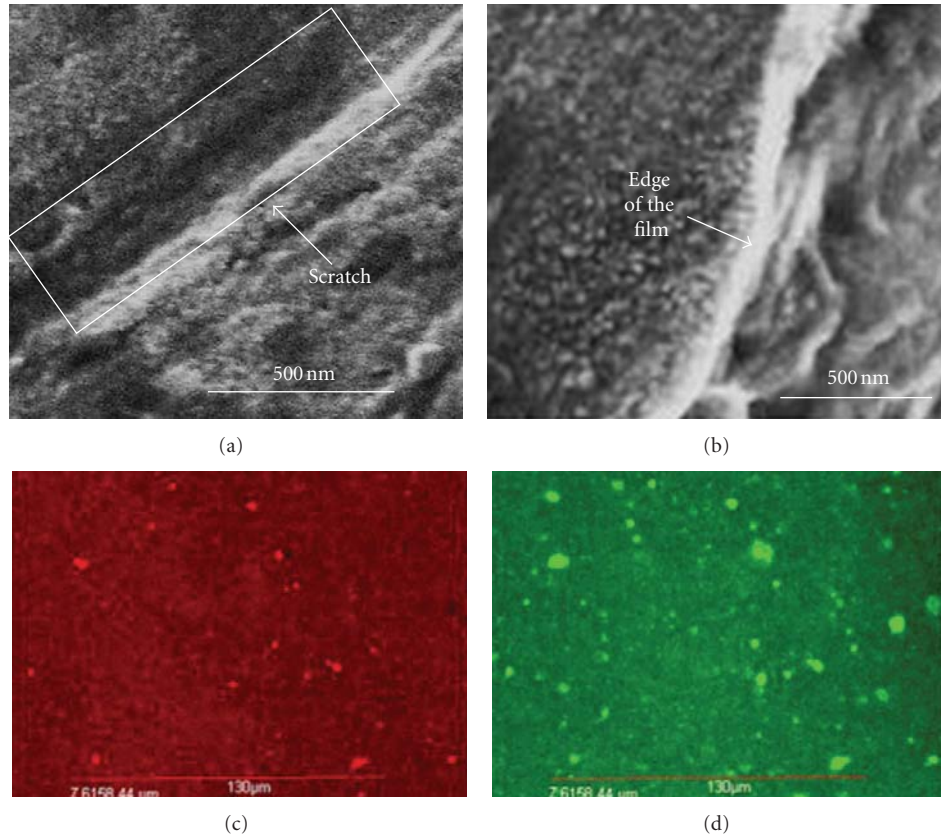


FIGURE 6: SEM images of a 6 bilayer LbL nanoassembled CIGS film. (a) Top surface. (b) The edge of the film. Confocal images of the (c) bottom and (d) top layer of a CIGS-PSS/PEI film.

with PSS shows a better adsorption to the surface than bare particles. It is attributed to a better attachment between the two polymers PSS and PEI, compared to the attachments between CIGS and PSS or CIGS and CIGS. Moreover, the comparable thicknesses of CIGS/CIGS and CIGS/PSS films further show that the attachment of CIGS to PSS is better than CIGS to CIGS.

AFM image showing the top surface of a CIGS-PSS/PEI film composed of 6 bilayers is presented in Figure 5. A scratch made using micromanipulator probe is also seen in the figure. The depth of the scratch was measured to be 60 nm using step height measurement tool within AFM. The depth of the scratch measured is smaller than the film thickness given by the QCM result. It shows that the scratch does not completely penetrate through the film. SEM images of a 6 bilayer CIGS-PSS/PEI film are shown in Figure 6. Figure 6(a) shows the top surface of the film illustrating a scratch made by the micromanipulator probe. Figure 6(b) shows the edge of the film. The SEM images confirm the solid film formed of the nanoparticles. Confocal scanning microscopy images of the first (bottom) and last (top) layers of a CIGS-PSS/PEI film taken with the help of fluorescent dyes are shown in Figures 6(c) and 6(d), respectively. The distinct colors of the bottom and the top surfaces of the film show that the layers are separated.

The resistivity of a $200\ \mu\text{m} \times 58\ \text{cm}$ channel on an ITO-coated glass was $47\ \text{M}\Omega\cdot\text{m}$. The decrease in measured

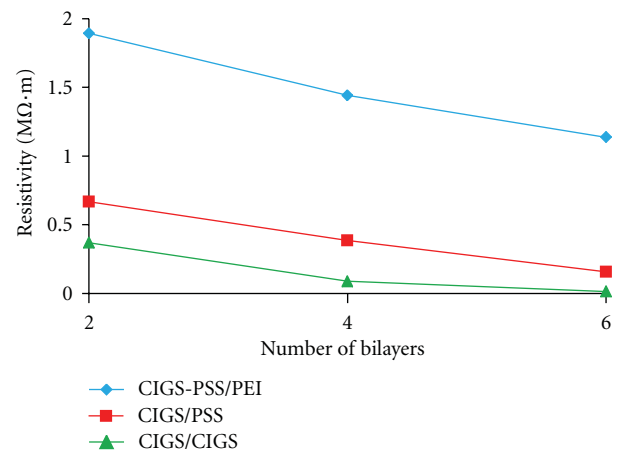


FIGURE 7: Resistivity versus number of bilayers of the deposited film of CIGS/CIGS, CIGS-PSS/PEI, and CIGS/PSS.

resistivity of the films with the deposition of every 2 bilayers of the films is shown in Figure 7. The resistivity for 6 bilayers of CIGS-PSS/PEI, CIGS/PSS, and CIGS/CIGS films was measured to be $1.13\ \text{M}\Omega\cdot\text{m}$, $0.15\ \text{M}\Omega\cdot\text{m}$, and $0.01\ \text{M}\Omega\cdot\text{m}$, respectively. The CIGS-PSS/PEI film has a higher resistivity due to the introduced PSS and PEI polymers. The CIGS/CIGS film has the lowest resistivity as expected.

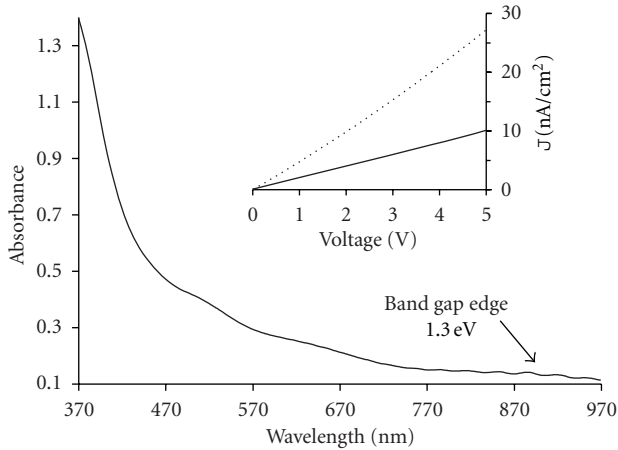


FIGURE 8: Absorbance spectrum of a CIGS-PSS/PEI film. The inset shows the current-voltage (J/V) characteristics of 6 bilayers of CIGS-PSS/PEI film in the dark (solid line) and under illumination (dotted line).

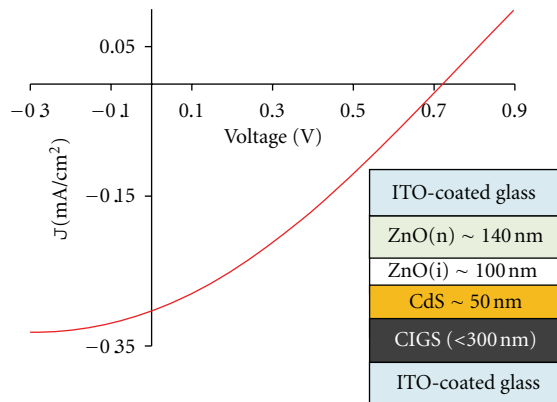


FIGURE 9: J/V characteristic of a solar cell device consisting of CIGS-PSS/PEI, CdS, ZnO(n), and ZnO(i) films with ITO as both back and front contacts, when illuminated by 50 W light source. The inset shows the schematic of the device structure.

The optical absorbance of a CIGS-PSS/PEI film deposited on a glass substrate is shown in Figure 8. The results show that the absorbance spectrum edge of the film is near 920 nm wavelength (1.3 eV band edge). The inset of Figure 8 shows the current-voltage (J/V) characteristic of a 6-bilayer CIGS-PSS/PEI film deposited on a $200\ \mu\text{m} \times 58\ \text{cm}$ channel, in the dark and when illuminating with a 100 W light source. It is observed that the current density increases by three folds when illuminated by the light source. However, the polymers employed in the LbL deposition process might be susceptible to photodegradation effects, which will be studied in the future, and may require further material design.

3.3. Solar Cell Results. The measured J/V characteristic of the solar cell with $1.0\ \text{cm}^2$ active area, when illuminated by a 50 W light-source, is shown in Figure 9. The considered solar cell structure is shown in the inset of the figure. The open circuit voltage (V), short circuit current density (J),

and power density under the illumination were measured to be 0.7 V, 0.3 mA/cm^2 , and 0.168 mW/cm^2 , respectively. The efficiency of the presented solar cell was measured to be 3.5%, which is comparable to the recently reported devices by emerging fabrication techniques such as spray-deposition, but lower than the devices fabricated through coevaporation of the CIGS materials. The LbL assembled CIGS films contain defects that increase carrier recombination. These films are also loosely packed and include polymers that contribute to lower the carrier mobility and thus affect the efficiency of the solar cell. However, it should also be noted that LbL assembly is simple, cost-effective, and highly scalable.

4. Conclusions

Fabrication of thin CIGS films using cost-effective, nonvacuum, and highly scalable LbL nanoassembly process has been presented. CIGS nanoparticles were synthesized, dispersed in water, and desired zeta-potential were obtained through pH regulation (from +61 mV at pH 7 to -51 mV at pH 10.5) and coating with PSS (-56.9 mV). The LbL film deposition process of the oppositely charged CIGS nanoparticles (CIGS/CIGS), CIGS nanoparticles and PSS (CIGS/PSS), and PSS-coated CIGS nanoparticles and polyethylenimine (CIGS-PSS/PEI) was studied. The J/V and photoelectric characterization results of the films have been presented and discussed. Prototype solar cell devices using the developed films have been fabricated and tested. LbL deposited CIGS films are applicable in cost-effective solar manufacturing.

Acknowledgments

Acknowledgments are due to the Integrated Nanosystems Development Institute (INDI) for providing the support and facility for this research. The authors are thankful to Jason Cambridge, Mark Canner, Parvin Ghane, Robert Vittoe, and Dr. Daniel Minner for their laboratory assistance.

References

- [1] M. Agarwal, S. Shrestha, P. Ghane, and K. Varahramyan, "Layer-by-Layer nanoassembly of CIS nanoparticles," in *Proceedings of the ASME International Manufacturing Science and Engineering Conference*, vol. 2, pp. 415–418, Erie, Pa, USA, 2010.
- [2] F. N. Crespilho, V. Zucolotto, O. N. Oliveria Jr., and F. C. Nart, "Electrochemistry of layer-by-layer films: a review," *International Journal of Electrochemical Science*, vol. 1, pp. 194–214, 2006.
- [3] I. Repins, M. A. Contreras, B. Egaas et al., "19.9%-efficient ZnO/CdS/CuInGaSe₂ solar cell with 81.2% fill factor," *Progress in Photovoltaics: Research and Applications*, vol. 16, no. 3, pp. 235–239, 2008.
- [4] M. Powalla, G. Voorwinden, D. Hariskos, P. Jackson, and R. Kniese, "Highly efficient CIS solar cells and modules made by the co-evaporation process," *Thin Solid Films*, vol. 517, no. 7, pp. 2111–2114, 2009.
- [5] V. K. Kapur, A. Bansal, P. Le, and O. I. Asensio, "Non-vacuum processing of CuIn_{1-x}Ga_xSe₂ solar cells on rigid and

- flexible substrates using nanoparticle precursor inks,” *Thin Solid Films*, vol. 431-432, pp. 53–57, 2003.
- [6] F. Bensebaa, C. Durand, A. Aouadou et al., “A new green synthesis method of CuInS_2 and CuInSe_2 nanoparticles and their integration into thin films,” *Journal of Nanoparticle Research*, vol. 12, no. 5, pp. 1897–1903, 2010.
- [7] A. R. Uhl, Y. E. Romanyuk, and A. N. Tiwari, “Thin film $\text{Cu}(\text{In,Ga})\text{Se}_2$ solar cells processed from solution pastes with polymethyl methacrylate binder,” *Thin Solid Films*, vol. 519, no. 21, pp. 7259–7263, 2011.
- [8] K. Varahramyan and Y. Lvov, “Nanomanufacturing by layer-by-layer assembly—from nanoscale coating to device applications,” *Journal of Nanoengineering and Nanosystems*, vol. 220, no. 1, pp. 29–37, 2006.
- [9] M. G. Panthani, V. Akhavan, B. Goodfellow et al., “Synthesis of CuInS_2 , CuInSe_2 , and $\text{Cu}(\text{In}_x\text{Ga}_{1-x})\text{Se}_2$ (CIGS) nanocrystal “inks” for printable photovoltaics,” *Journal of the American Chemical Society*, vol. 130, no. 49, pp. 16770–16777, 2008.
- [10] A. de Kergommeaux, A. Fiore, N. Bruyant et al., “Synthesis of colloidal CuInSe_2 nanocrystals films for photovoltaic applications,” *Solar Energy Materials and Solar Cells*, vol. 95, supplement 1, pp. S39–S43, 2011.
- [11] V. A. Akhavan, M. G. Panthani, B. W. Goodfellow, D. K. Reid, and B. A. Korgel, “Thickness-limited performance of CuInSe_2 nanocrystal photovoltaic devices,” *Optics Express*, vol. 18, no. S3, pp. A411–A420, 2010.
- [12] Y. Lvov, K. Ariga, I. Ichinose, and T. Kunitake, “Assembly of multicomponent protein films by means of electrostatic layer-by-layer adsorption,” *Journal of the American Chemical Society*, vol. 117, no. 22, pp. 6117–6123, 1995.

Research Article

Gold/Chitosan Nanocomposites with Specific Near Infrared Absorption for Photothermal Therapy Applications

Guandong Zhang,¹ Xinghua Sun,¹ Jacek Jasinski,² Dhruvin Patel,¹ and Andre M. Gobin¹

¹Department of Bioengineering, Speed School of Engineering, University of Louisville, Louisville, KY 40292, USA

²Conn Center for Renewable Energy Research and Speed School of Engineering, University of Louisville, Louisville, KY 40292, USA

Correspondence should be addressed to Andre M. Gobin, andre.gobin@louisville.edu

Received 5 May 2012; Revised 27 July 2012; Accepted 27 August 2012

Academic Editor: Gaurav Mago

Copyright © 2012 Guandong Zhang et al. This is an open access article distributed under the Creative Commons Attribution License, which permits unrestricted use, distribution, and reproduction in any medium, provided the original work is properly cited.

Gold/chitosan nanocomposites were synthesized and evaluated as a therapeutic agent for the photothermal therapy. Gold nanoparticles (Au NPs) with controllable optical absorption in the near infrared (NIR) region were prepared by the reaction of chloroauric acid and sodium thiosulfate. To apply these particles to cancer therapy, the bare Au NPs were coated with chitosan (CS), O-carboxymethyl chitosan (CMCS), and a blend of CS and CMCS for utilizations in physiologic conditions. The surface properties, optical stability, and photothermal ablation efficiency on hepatocellular carcinoma cells (HepG2) and human dermal fibroblast cells (HDF) demonstrate that these gold nanocomposites have great potential as a therapeutic agent in *in vitro* tests. The CS-coated nanocomposites show the highest efficiency for the photo-ablation on the HepG2 cells, and the CS and CMCS blended coated particles show the best discrimination between the cancer cell and normal cells. The well-controlled NIR absorption and the biocompatible surface of these nanocomposites allow low-power NIR laser activation and low-dosage particle injection for the cancer cell treatment.

1. Introduction

The use of nanoparticles (NPs) in biomedical field is one of the most important branches of nanobiotechnology. Many biomedical applications require nanoparticles with low toxicity, biocompatibility, and stability with high preferential accumulation in the target tissue or organ [1]. Polymer-nanoparticle composites may possess the unique property superior to that of either the polymer or nanoparticles. Metal nanoparticles with polymer coatings or dispersed in polymeric matrices display the increased stability, improved processability, recyclability, and solubility in a variety of solvents [2].

Gold nanoparticles (Au NPs) are attracting enormous attentions in applications for immunoassay [3, 4], drug delivery [5], contrast enhancement, and thermal therapy for tumor treatment [6–8], due to their nanoscale size, oxide-free components, bioconjugation property, biocompatibility, and unique optical properties.

Thermal therapy, also termed as hyperthermia, has thousands years history as one of most important methods for the

tumor treatment [9]. In this technique, moderate heating is generated in the target region, resulting in tumors selectively destroyed, due to their reduced heat tolerance compared to normal tissue [10]. In the past decades, because many new heating sources such as radiofrequency [11], microwave [12], magnetic field [13], and laser [9] were employed, there were remarkable progresses achieved in this area. Photothermal therapy (PT) is a promising field within thermal therapy, incorporating laser techniques and photoabsorbing agents. Light absorbing dyes, chemical photosensitizers, and solid optically responsive nanomaterials have been applied as the photoabsorbing agents in PT [9]. For small metal nanoparticles, their optical properties are dominated by collective oscillation of conduction electrons. An absorption band results when the incident photon frequency is resonant with the collective oscillation of the conduction band electrons, and this is known as the surface plasmon resonance (SPR) [14]. Au NPs possess strongly enhanced visible and near infrared light absorption, which is several orders of magnitude more intense compared to conventional chromophores. Various gold-based nanostructures with NIR

absorption have been developed. Gold nanospheres [15], gold nanoshells [7], gold nanorods [16], and gold nanocages [17] are the popular nanostructures that have been demonstrated in photothermal therapeutics due to their strongly enhanced absorption in the visible and NIR regions on account of their SPR effects.

In our work, Au NPs with NIR absorption were prepared by the one step reaction of chloroauric acid and sodium thiosulfate. Their NIR absorption wavelengths were well controlled by adjusting molar ratio of $\text{HAuCl}_4/\text{Na}_2\text{S}_2\text{O}_3$ [18]. These Au NPs were coated with chitosan- (CS)-based coatings and used as a therapeutic agent for the photothermal ablation of cancer cells. Chitosan is a biobased polysaccharide derived from shrimp and crab shells [19]. It is nontoxic, biodegradable and biocompatible, and has good processability [20, 21]. The cost associated with chitosan is much lower than that of other polymer coatings or chemical compounds, for example, polyethylene glycol (PEG) that are often used to protect and stabilize the nanoparticles by many researchers [5]. Hepatocellular carcinoma is the most common primary malignant tumor of the liver. It affects greater than half a million patients worldwide. US liver-related cancer deaths account for 4% of all cancers or about 20,000 deaths annually. Two anchorage-dependent cell lines, hepatocellular carcinoma cell line (HepG2), and control cell line of human dermal fibroblast (HDF) were selected for the estimation of laser ablation efficiency of these novel gold nanocomposites. The efficacy was evaluated by live/dead stain images following photothermal ablation. These gold nanocomposites show great ability for laser ablation, and the surface coating components plays a very important role for selectivity to certain cancer cells. In addition, this composite material offers new and desirable advantages for cancer treatment. Beside the optically tunable gold nanoparticle for efficient conversion of light to heat, chitosan-based coatings provide tunable surface charges for applications in a variety of physiological pH environments and also allow further modification with targeting molecules or drug molecules by chemical reaction or electrostatic interaction.

2. Experimental

2.1. Preparation of Au Nanoparticles. Au NPs were prepared by the method we reported before [18, 22]. In which, 3 mM sodium thiosulfate ($\text{Na}_2\text{S}_2\text{O}_3 \cdot 5\text{H}_2\text{O}$, Aldrich, 99.999%) solution was added into 1.71 mM chloroauric acid ($\text{HAuCl}_4 \cdot 3\text{H}_2\text{O}$, Alfa Aesar, Au 49.68%) solutions with desired volume ratio at room temperature and vortexed for 20 seconds for uniform mixing. All the water used in the experiments was purified by a Thermo Scientific Easypure II system, with a resistivity of 18.2 M Ω cm.

2.2. Preparation of Carboxymethylated Chitosan. Low molecule weight chitosan (Sigma-Aldrich, MW 50–190 K) was used for the surface coating of the Au NPs. Based on this chitosan, O-carboxymethyl chitosan (CMCS) was synthesized as the reported method [23, 24]. Briefly, 15 g sodium hydroxide was dissolved in a 20:80 mixture of deionized water and isopropanol (100 mL) in a 500 mL flask. 10 g chitosan was

added to the flask to swell and alkalize at 50°C for 1 h. 15 g monochloroacetic acid ($\text{ClCH}_2\text{CO}_2\text{H}$, 99%, Acros Organics) was dissolved in 20 mL isopropanol and added into the reaction mixture dropwisely in 30 min and reacted under vigorous agitation for 4 h at 55–60°C. Adding 200 mL 80% ethyl alcohol stopped the reaction. The product was filtered and repeatedly rinsed by 80% ethyl alcohol, to desalt and dewater, until the pH value of the washing solution was less than 8.0. Finally, the product was vacuum dried for 1 day at 40°C.

2.3. Preparation and Purification of Au NPs with Chitosan Based Coatings. Stock solution of chitosan was prepared by dispersing chitosan (1 g) in 0.7% acetic acid solution (100 mL). CMCS solution was prepared by directly dissolving CMCS (1 g) in 100 mL DI water. CS and CMCS solutions were purified by centrifuge at 1000 rpm for 10 min, to remove the little amount of insoluble residuals, and then were dialyzed (Spectrum Dialysis Membranes, MWCO 3 KDa) for 2 days. The chitosan-coated Au NPs (Au/CS), CMCS coated Au NPs (Au/CMCS), and CS and CMCS blended coated Au NPs (Au/(CS+CMCS)) were prepared by, respectively, adding CS solution, CMCS solution, or CS and CMCS blending solution (CS and CMCS solutions were premixed) dropwisely into the as-synthesized gold particle suspensions, with vigorous agitation. The ratio between CS or CMCS to Au NPs was controlled as 0.2 mg CS or CMCS per OD Au NP suspension and between CS and CMCS blending to Au NPs is (0.15 mg CS + 0.05 mg CMCS) per OD Au NP suspension (OD is the optical density). Then these samples were set on the rocking bed for 1 day. In the end the gold nanocomposite suspensions were concentrated and separated from the solution by centrifugation at 1000 g for 20 min. This step will remove the byproducts in solution and the extra chitosan. Then the centrifuged pellets were dispersed in sterilized DI water to a concentration of 25 OD/mL and stored at 4°C for the subsequent studies.

2.4. Characterization of Au NPs. The optical absorption of Au NPs was measured by a UV-Visible spectrophotometer (Cary-50Bio, Varian). A Zetasizer (Nano-ZS90, Malvern) was used to assess the surface charge of the nanoparticle suspensions. A FEI Tecnai F30 transmission electron microscope (TEM) operated at 200 KV was used to determine the morphology of Au NPs. Several Au NPs suspensions that have different NIR peak wavelength were carefully prepared for the photo-induced temperature rising measurement. 1 mL of the Au NP suspensions were added into the wells of tissue culture plate (Multiwell, Primaria 24 Well), with the concentration of 1 OD/mL. A laser with 817 nm centered wavelength generated by FAT-System (Coherent, CA) was shone on the gold suspension. The laser spot has the same area with the well, and the power of the laser was fixed as 1 W/cm². An infrared thermometer (CSmicro, Optris GmbH, Germany) detecting the temperature of the Au NP suspension was fixed 10 cm above the media.

2.5. Photothermal Ablation Study. All cell lines were obtained from ATCC (Manassas, MA). Human dermal fibroblasts cell

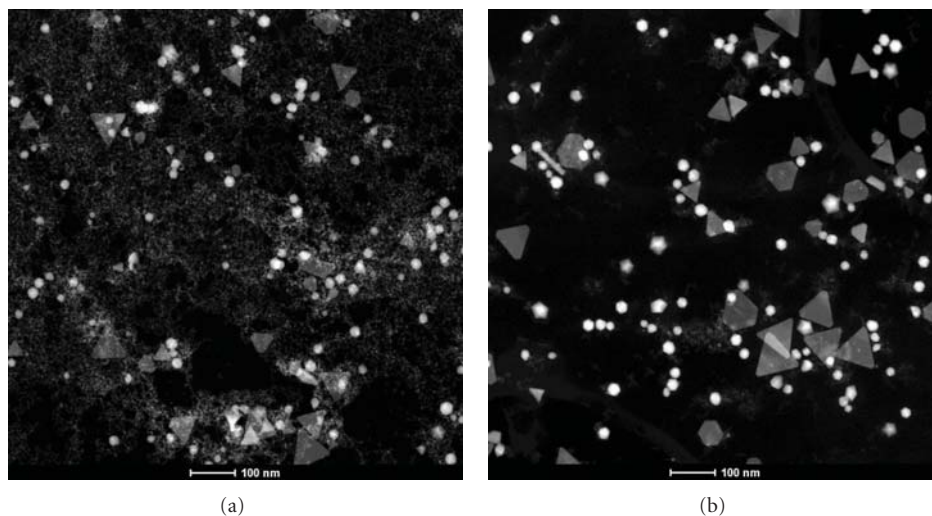


FIGURE 1: Z-contrast STEM images of the Au NPs synthesized from reaction of HAuCl_4 and $\text{Na}_2\text{S}_2\text{O}_3$ before and after centrifugation process. (a) As-synthesized Au NPs; (b) Au NPs after purification by centrifugation. The purified product has the NIR absorption peak at 820 nm.

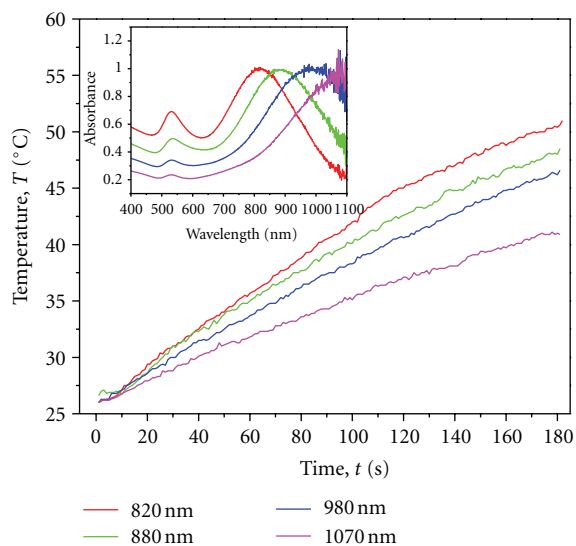


FIGURE 2: Heating effect of the gold nanoparticles with NIR absorption peaks at 820 nm, 880 nm, 980 nm, and 1070 nm, respectively, under the 817 nm wavelength laser exposures. The laser power is 1 W/cm^2 , and the Au NPs were dispersed in water at a concentration of 1 OD/mL. Inset shows the UV-visible-NIR spectra of the four Au NPs samples.

line (HDF, ATCC: PCS-201-012 male source) and hepatocellular carcinomas cell line (HepG2, ATCC: 59194) were seeded at monolayer confluence to allow for easier cell counting following staining (within 15 passages). All the cells were cultured at 37°C in a 5% CO_2 environment in Dulbecco's modified eagle medium (DMEM) supplemented with 4 mM l-glutamine, 1% penicillin, and 10% fetal bovine serum. Prior to laser ablation experiments, cells were detached from culture flask with trypsin (0.25%) and resuspended in DMEM media and injected into the 24-well tissue culture plate (Multiwell, Primaria), cultured for 36–48 hours to achieve confluence. Laser ablation was performed based on

methods described in [7]. Cells were incubated with 1 mL DMEM media which contains 1 OD Au NPs for 2 h to obtain the binding of the Au NPs on the cell. For this experiment, Au NPs and gold/chitosan nanocomposites were prepared with NIR absorption in the range of 820 nm to 850 nm, close to the wavelength of the laser source. Media were removed, and cells were rinsed with 0.5 mL PBS buffer, followed by addition of 0.5 mL fresh media to the culture wells. Next, the cells were exposed to 817 nm NIR laser at optimized conditions (5 W/cm^2 , 2 min). Well plates were incubated overnight after photothermal treatment, and a live/dead stain (Invitrogen, Carlsbad, CA) was performed, and fluorescent images were obtained and analyzed. Images were taken with a Nikon D90 camera on an Accu-Scope 3032 Microscope for green/red fluorescence, respectively, and cell numbers were counted manually.

3. Results and Discussion

3.1. Preparation of Gold Nanoparticles with Desired Near Infrared Absorption. In our previous work [18, 25], a convenient method was developed to synthesize Au NPs with controllable NIR absorption. Au NPs were synthesized by one-step reaction of chloroauric acid and sodium thiosulfate, without assistance of additional templates, capping reagents, or seeds assembly. The synthesized products consist of nanoparticles with different shape and size including small spherical colloid gold particles ($<5 \text{ nm}$) and nonspherical gold crystals. The nonspherical gold crystals are mainly the truncated octahedron, pentagons, and cuboctahedron, as well as the triangular-shaped plate structures [18]. Two absorption peaks due to the surface plasmon resonance are observed from these samples. The first SPR peak centered at around 530 nm is the characteristic SPR of the spherical colloid gold particles, and the second SPR component is higher at NIR band, which is attributed to the multipolar SPR band from the nonspherical Au NPs [18, 25]. Since the NIR absorption wavelengths increase with increasing

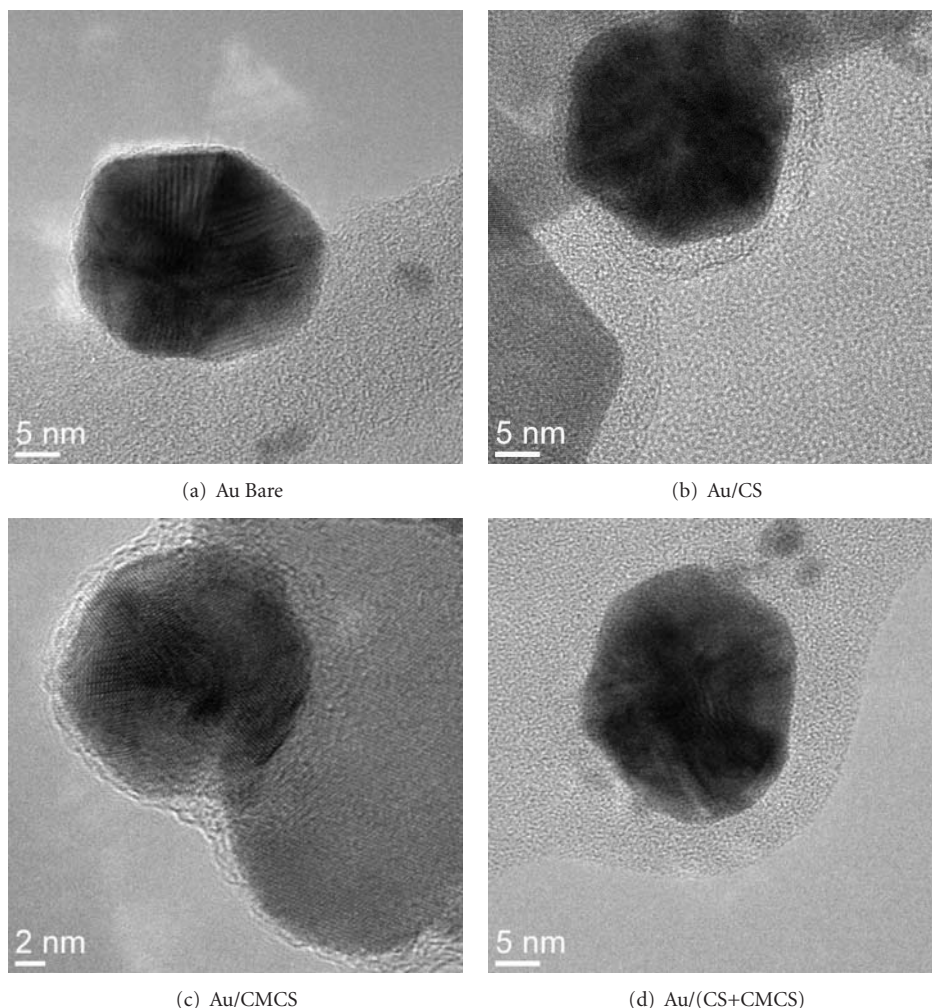


FIGURE 3: High-resolution TEM images of the Au NPs: (a) Au NPs without coating, (b) Au/CS nanocomposite, (c) Au/CMCS nanocomposite, and (d) Au/(CS+CMCS) nanocomposite.

molar ratio of $\text{HAuCl}_4/\text{Na}_2\text{S}_2\text{O}_3$, adjusting the molar ratio of $\text{HAuCl}_4/\text{Na}_2\text{S}_2\text{O}_3$ during the reaction controlled the absorption wavelength of the Au NPs. These products were further purified by the centrifugation to remove the spherical colloid gold particles, improving the NIR absorption. Figures 1(a) and 1(b) are the Z-contrast STEM images of the as-synthesized Au NPs and the same batch sample purified with centrifugation. The purified product possesses the NIR absorption wavelength at 820 nm. The temperature of the NIR absorbing Au NP suspension induced by the NIR laser radiation is affected by the concentration of nanoparticles, laser power, exposure time, and the absorbing wavelength of the Au NPs [26]. Figure 2 compares the heating effect of the Au NPs suspensions with NIR peak at 820 nm, 880 nm, 980 nm, and 1070 nm, respectively (showing in the insert figure) under the 817 nm wavelength diode laser (1 W/cm^2) exposures. After 3 minutes, the temperature reaches to 50.8, 48.2, 46.4, and 41.2°C for the particles from low wavelength to high wavelength, respectively. The gold sample that has the NIR peak more close to the wavelength of laser source shows the best heating effect. The effective control of the NIR absorption of the gold nanoparticles for matching the

wavelength of the laser source enhances the hyperthermia treatment. Meanwhile, the NIR wavelength is considered as the best light source for the photothermal therapy, because it is minimally absorbed by the normal tissues components of water and hemoglobin and can transmit deeply in the body.

3.2. Chitosan-Based Coatings on the Gold Nanoparticles. Chitosan is a cationic polysaccharide of D-glucosamine and N-acetyl-D-glucosamine and has been shown to be a highly biocompatible material and have antibiotic properties. To improve its solubility or achieve new functionality, chemical modifications of chitosan were conducted and many derivatives have been synthesized. For example, modifications can be synthesized by carboxylation of the hydroxyl or amine groups in chitosan structure [20], resulting in the O-carboxymethyl chitosan or N-carboxymethyl chitosan respectively. O-carboxymethyl chitosan is achieved by substituting parts of the $-\text{OH}$ at C-6 position of glucosamine units with $-\text{CH}_2\text{COOH}$. Therefore, the reactive ligands such as $-\text{COOH}$ and $-\text{NH}_2$ groups are amenable to chemical functions. Others have reported the stabilization of GNPs with chitosan. As chitosan in solution is protonated and

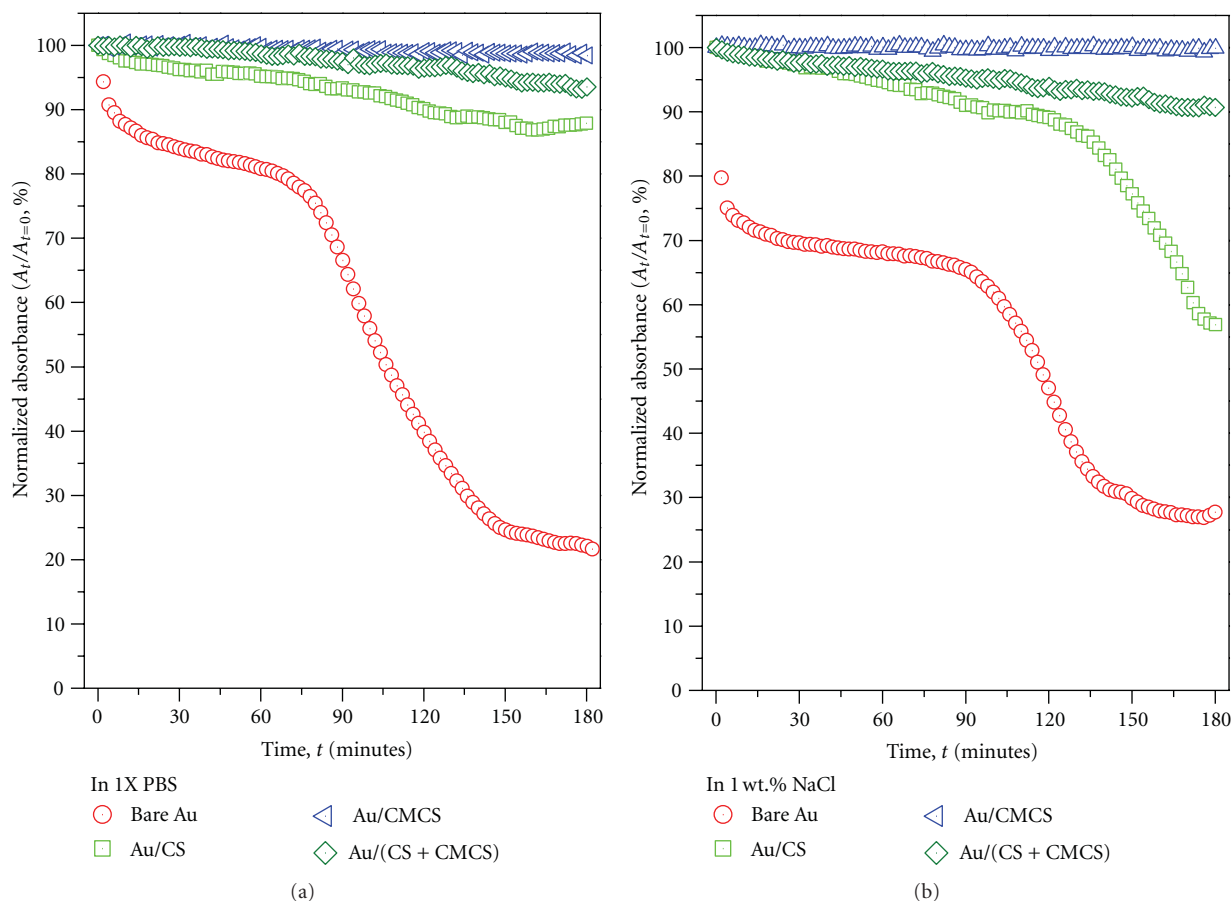


FIGURE 4: Optical stability of the Au NPs with different chitosan coatings in (a) PBS solution and in (b) 1 wt.% NaCl solution.

positively charged, it can be adsorbed onto the surfaces of gold nanoparticles, stabilizing and protecting the nanoparticles [27–29]. As-synthesized Au NPs present strongly negative surface charge (around -40 mV) allowing the positive charged chitosan tightly coated onto gold surface *via* electrostatic interaction.

Figures 3(a), 3(b), 3(c), and 3(d) show the high-resolution TEM images of the Au NPs without coating, Au/CS, Au/CMCS, and Au/(CS+CMCS) nanocomposites, respectively. The as-synthesized bare Au NPs have a 1–2 nm thin layer on their surface. Comparing to the bare Au NPs, Figures 3(b)–3(d) show the chitosan-based coatings effectively cover the gold NPs uniformly, forming a 2–5 nm thick layer on the gold surface.

Table 1 lists the hydrodynamic diameter and the surface charge of the gold nanoparticles with different chitosan-based coatings in water. The chitosan-based coating significantly changed the surface property of the gold nanoparticles. The average particle size of the bare gold nanoparticles is 36 nm; after being coated with polymer, the hydrodynamic diameter of Au/CS, Au/CMCS, and Au/(CS+CMCS) reaches 290, 236, and 262 nm, respectively. Meanwhile, their surface charge changes from -43.5 mV to $+43.8$, $+20.2$ and $+24.3$ mV, respectively.

Figure 4 shows the optical stability of the Au NPs with different coatings in PBS and 1 wt% NaCl solution. Since

the physiologic salinity is near 1%, optical properties of Au NPs were simulated in these solutions. The optical stabilities were measured by monitoring the optical absorbance of the Au NPs at their NIR peak wavelength as function of time. These nanoparticles have similar behavior in the PBS and NaCl solution. CMCS-coated particles show the highest stability, and there is no obvious decrease in its optical absorption in 3h. The CS and CMCS blended coated particles also show good stability, with a decrease in its absorbance less than 10%. The most unstable particles are the bare Au NPs. Its absorbance decreases more than 70% in saline environment. The Au/CS nanocomposites are more stable than the bare particles, but less stable than the Au NPs with CMCS component in the coating. The decrease of NIR absorption of the bare Au NPs results from interparticle coupling effect [30, 31], in which its stabilized surface layer was disturbed due to the high ion strength, causing the particle aggregation (irreversible coalescence). This behavior may greatly decrease the efficiency of photothermal ablation. Chitosan-based coatings greatly improve the optical stability of the Au NPs. The instability of the Au/CS NPs mainly results from the sedimentation of particles caused by the agglomeration (reversible coalescence) of chitosan coating. At the pH value above 6, the solubility of chitosan becomes worse. CMCS has the best solubility in all pH ranges except its isoelectrical point [23]. The good solubility and the

TABLE 1: Surface property of the gold nanoparticles with different chitosan-based coatings. Particles are dispersed in DI water with a concentration of 1 OD/mL.

| Nanoparticles | Coating components | Hydrodynamic diameter (nm, mean \pm STD) | Zeta Potential (mV, mean \pm STD) |
|----------------|-----------------------------|--|-------------------------------------|
| Au Bare | None | 36.0 \pm 1.78 | -43.5 \pm 2.92 |
| Au/CS | CS | 290.4 \pm 52.7 | +43.8 \pm 4.36 |
| Au/CMCS | CMCS | 235.5 \pm 9.05 | +20.2 \pm 0.68 |
| Au/(CS + CMCS) | 75 wt.% CS+ 25 wt.% CMCS | 262.3 \pm 58.9 | +24.3 \pm 0.80 |

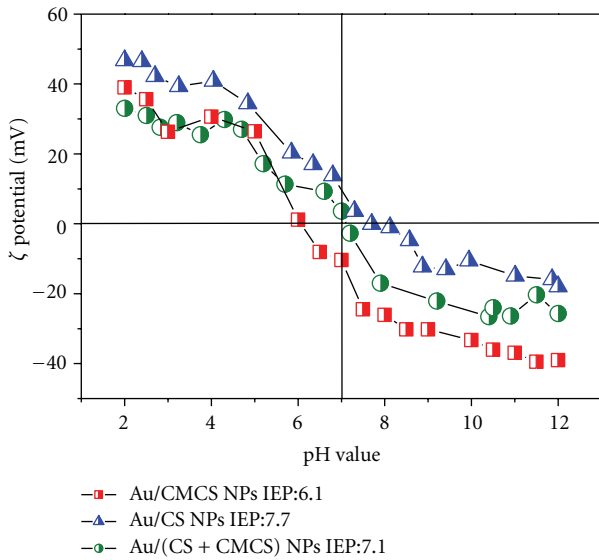


FIGURE 5: Effect of pH on Zeta potential of Au NPs with different coatings. Square point: Au/CMCS NPs, Triangle point: Au/CS NPs, Sphere point: Au/(CS+CMCS) NPs.

increased chain flexibility [32] of CMCS may prevent the coupling effect and the sedimentation of the particles.

By adjusting the surface components, the surface charge of the Au NPs can be modified. Figure 5 shows the zeta potential of Au NPs with different chitosan coatings as function of the pH value. The isoelectric points (IEPs) of Au/CMCS, Au/(CS+CMCS), and Au/CS nanocomposites are 6.1, 7.1, and 7.7, respectively. IEP of CMCS is close to value (5.5) reported by Zhao et al. [33]. CMCS presents amine and carboxylic acid groups in its structure. In solution, the groups turn to the ion state, $-\text{NH}_3^+$ and $-\text{COO}^-$, respectively, which improves the solubility of CMCS. Only at its IEP, the number of $-\text{NH}_3^+$ is equal to that of $-\text{COO}^-$, resulting in the decreasing of solubility. Au/CS particle shows much higher IEP value than that of the Au/CMCS particles, since the CS only presents the positively charged groups ($-\text{NH}_3^+$). The IEP of the Au/(CS+CMCS) particle is 7.1, between the those of Au/CMCS and Au/CS. This shows that the surface charge of Au NPs can be tuned by the chitosan components on their surface, since CMCS possesses more negatively charged characteristic than CS.

3.3. *Photothermal Ablation of the HepG2 Cells.* Figures 6 and 7 show the live/dead stain images of the HDF and HepG2

cells after being exposed to the 817 nm NIR laser at 5 W/cm², 2 min. The live/dead stain provides a two-color fluorescence assay of cell viability based on plasma membrane permeability, for reliably and quantitatively distinguishing live and dead cells. The live cells show the green color and dead cells show the red color. The statistical cell death ratio of HDF cells and HepG2 cells counted from the live/dead stain images are shown in Figure 8.

Without incubation with Au NPs, cells do not exhibit obvious ablation after the laser irradiation at 5 W/cm², 2 min, as shown in Figures 6(b) and 7(b). The bare Au NPs do not show significant photo-destruction on either cell lines (Figures 6(c) and 7(c)), due to the interparticle coupling effect [31]. The relatively low photothermal ablation efficiency of Au/CMCS NPs is probably due to their less adsorption on the cell membrane (Figures 6(e) and 7(e)). The highest efficiency of the photothermal ablation is observed from the cells treated with Au/CS NPs. There are almost 100% HepG2 cells, and 90% HDF cells were killed after the laser treatment (Figures 6(d) and 7(d)). The CS and CMCS blended coated gold NPs present the promising result: around 96% HepG2 cancer cells were ablated and less than 30% HDF normal cells died (Figures 6(f) and 7(f)). The differences of the Au NPs in the photothermal ablation result from the density of the Au NPs adsorbed on the cell surface. The negatively charged cell surface allows Au/CS NPs to highly accumulate on the cell surface, and high density particles generate extraordinary heat, damaging the HepG2 cells as well as the HDF cells under the laser radiation. Au/(CS+CMCS) particles bind to the cell surface uniformly and generate suitable heat, which was high enough to kill the cancer cells but not enough to damage all the normal cells. This consists with laser ablation results by using gold nanorod [16]. It was reported that after exposure to continuous red laser, malignant cells require about half the laser energy to be photothermally destroyed than the nonmalignant cells [16].

4. Conclusions

Gold/chitosan nanocomposites were synthesized for the photothermal therapy applications. Au NPs were prepared by the reaction of chloroauric acid with sodium thiosulfate, and they have specific NIR absorption matching the wavelength of laser source. These Au NPs were coated with chitosan or O-carboxymethyl chitosan as well as a blending. These chitosan coatings protect the gold nanoparticles, avoiding irreversible coalescence of the bare Au NPs and improving

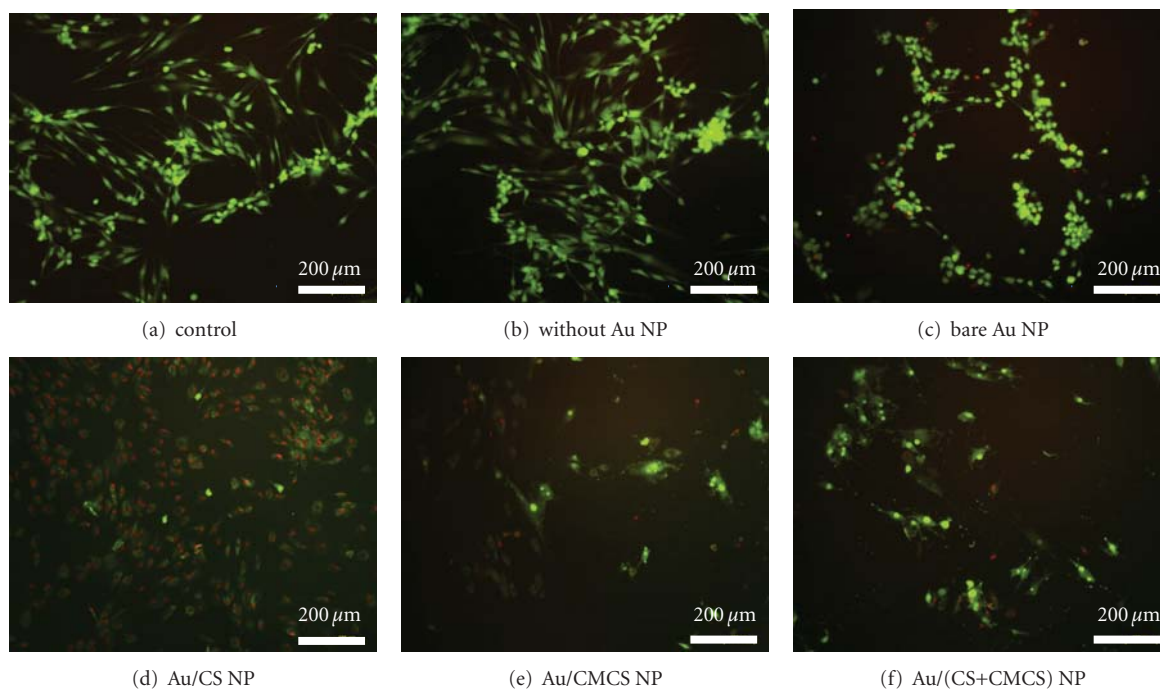


FIGURE 6: Live/dead stain images of the HDF cells treated with different Au NPs after the laser ablation (5 W/cm^2 , 2 min). (a) control cells with no laser exposure, (b) cells without NPs, (c) cells treated with bare Au NPs, (d) cells treated with Au/CS NPs, (e) cells treated with Au/CMCS NPs, and (f) cells treated with Au/(CS+CMCS) NPs.

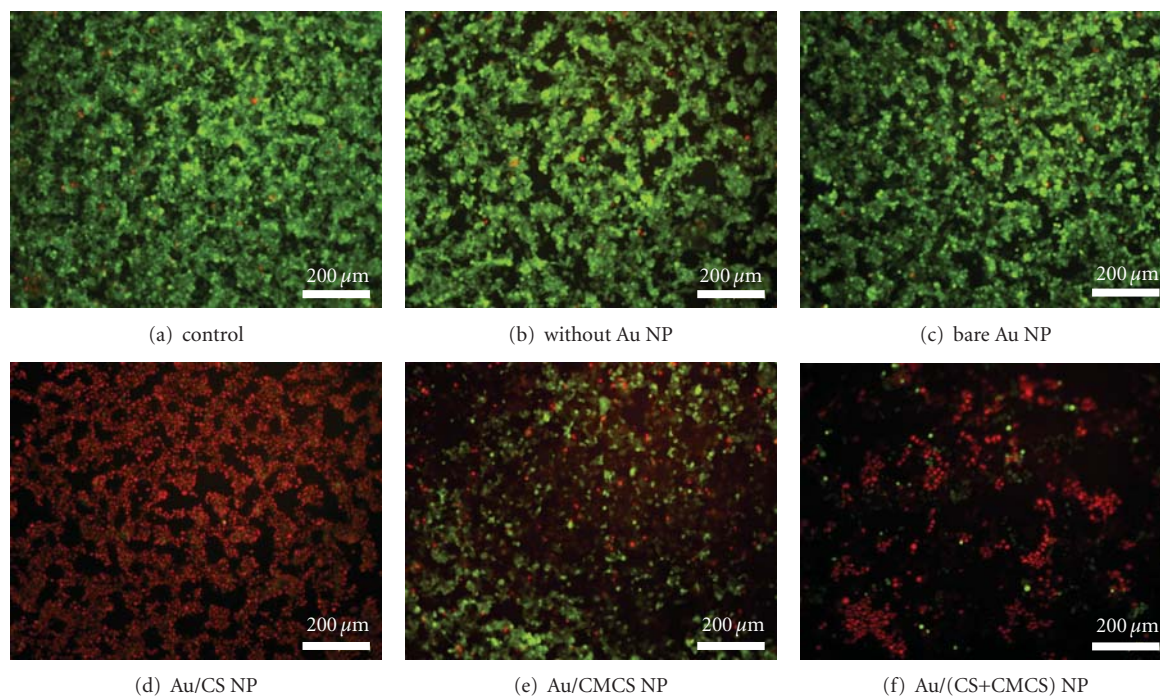


FIGURE 7: Live/dead stain images of the HepG2 cells treated with different Au NPs after the laser ablation (5 W/cm^2 , 2 min). (a) control cells with no laser exposure, (b) cells without NPs, (c) cells treated with bare Au NPs, (d) cells treated with Au/CMCS NPs, (e) cells treated with Au/CS NPs, and (f) cells treated with Au/(CS+CMCS) NPs.

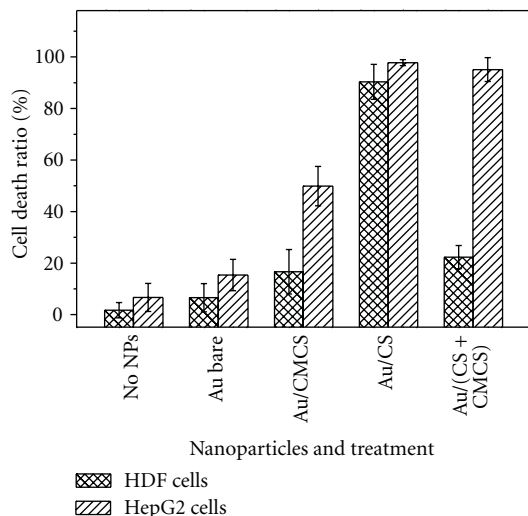


FIGURE 8: Death percentage of HDF cell and HepG2 cell cells treated with different Au NPs after the laser ablation at 5 W/cm^2 , 2 min. (Average \pm STD, $n = 3$).

their optical stability, making photothermal ablation possible. The surface charge of the Au/chitosan nanocomposites can be modified by adjusting the CS and CMCS components on the gold surface to achieve suitable binding of the Au NPs on the cell surface. The Au/CS nanocomposites show high accumulation on the cell surface and present the highest laser ablation efficiency. The CS and CMCS blended coatings allow Au NPs uniformly binding to the cells, showing higher selectivity between the cancer cells and normal cells during the photothermal ablation. These novel gold/polymer nanocomposites have great potential for photothermal therapy, due to low-dosage particle injection, low-power NIR laser radiation, and quick ablation. More broad clinical relevance can be envisioned, such as the breast cancer treatment, skin cancer treatment, esophageal cancer treatment, and laryngocarcinoma cancer treatment.

Acknowledgments

Authors greatly acknowledge Deborah Hickman and Dr. Andrea Gobin for help with experiments and sample characterization. Research is supported by grants from Wallace Coulter Foundation: Early Career Phase 1 Award and the School of Medicine Summer Research Scholar Program.

References

- [1] A. K. Gupta and M. Gupta, "Synthesis and surface engineering of iron oxide nanoparticles for biomedical applications," *Biomaterials*, vol. 26, no. 18, pp. 3995–4021, 2005.
- [2] R. Shenhar, T. B. Norsten, and V. M. Rotello, "Polymer-mediated nanoparticle assembly: structural control and applications," *Advanced Materials*, vol. 17, no. 6, pp. 657–669, 2005.
- [3] L. R. Hirsch, J. B. Jackson, A. Lee, N. J. Halas, and J. L. West, "A whole blood immunoassay using gold nanoshells," *Analytical Chemistry*, vol. 75, no. 10, pp. 2377–2381, 2003.
- [4] D. S. Grubisha, R. J. Lipert, H. Y. Park, J. Driskell, and M. D. Porter, "Femtomolar detection of prostate-specific antigen: an immunoassay based on surface-enhanced raman scattering and immunogold labels," *Analytical Chemistry*, vol. 75, no. 21, pp. 5936–5943, 2003.
- [5] T. Niidome, M. Yamagata, Y. Okamoto et al., "PEG-modified gold nanorods with a stealth character for *in vivo* applications," *Journal of Controlled Release*, vol. 114, no. 3, pp. 343–347, 2006.
- [6] M. C. Daniel and D. Astruc, "Gold nanoparticles: assembly, supramolecular chemistry, quantum-size-related properties, and applications toward biology, catalysis, and nanotechnology," *Chemical Reviews*, vol. 104, no. 1, pp. 293–346, 2004.
- [7] A. M. Gobin, M. H. Lee, N. J. Halas, W. D. James, R. A. Drezek, and J. L. West, "Near-infrared resonant nanoshells for combined optical imaging and photothermal cancer therapy," *Nano Letters*, vol. 7, no. 7, pp. 1929–1934, 2007.
- [8] C. Alric, J. Taleb, G. Le Duc et al., "Gadolinium chelate coated gold nanoparticles as contrast agents for both X-ray computed tomography and magnetic resonance imaging," *Journal of the American Chemical Society*, vol. 130, no. 18, pp. 5908–5915, 2008.
- [9] X. Huang, P. K. Jain, I. H. El-Sayed, and M. A. El-Sayed, "Plasmonic photothermal therapy (PPTT) using gold nanoparticles," *Lasers in Medical Science*, vol. 23, no. 3, pp. 217–228, 2008.
- [10] P. R. Stauffer, "Evolving technology for thermal therapy of cancer," *International Journal of Hyperthermia*, vol. 21, no. 8, pp. 731–744, 2005.
- [11] S. N. Goldberg, "Radiofrequency tumor ablation: principles and techniques," *European Journal of Ultrasound*, vol. 13, no. 2, pp. 129–147, 2001.
- [12] R. Valdagni, M. Amichetti, and G. Pani, "Radical radiation alone versus radical radiation plus microwave hyperthermia for N_3 (TNM-UICC) neck nodes: a prospective randomized clinical trial," *International Journal of Radiation Oncology Biology Physics*, vol. 15, no. 1, pp. 13–24, 1988.
- [13] R. Hergt, S. Dutz, R. Müller, and M. Zeisberger, "Magnetic particle hyperthermia: nanoparticle magnetism and materials development for cancer therapy," *Journal of Physics Condensed Matter*, vol. 18, no. 38, pp. S2919–S2934, 2006.
- [14] W. Fink, H. van der Piepen, and W. Schneider, "Optical surface plasmon resonance as a measurement tool," pp. 419–423, 1975.
- [15] I. H. El-Sayed, X. Huang, and M. A. El-Sayed, "Selective laser photo-thermal therapy of epithelial carcinoma using anti-EGFR antibody conjugated gold nanoparticles," *Cancer Letters*, vol. 239, no. 1, pp. 129–135, 2006.
- [16] X. Huang, I. H. El-Sayed, W. Qian, and M. A. El-Sayed, "Cancer cell imaging and photothermal therapy in the near-infrared region by using gold nanorods," *Journal of the American Chemical Society*, vol. 128, no. 6, pp. 2115–2120, 2006.
- [17] M. Hu, H. Petrova, J. Chen et al., "Ultrafast laser studies of the photothermal properties of gold nanocages," *Journal of Physical Chemistry B*, vol. 110, no. 4, pp. 1520–1524, 2006.
- [18] G. Zhang, J. B. Jasinski, J. L. Howell, D. Patel, D. P. Stephens, and A. M. Gobin, "Tunability and stability of gold nanoparticles obtained from chloroauric acid and sodium thiosulfate reaction," *Nanoscale Research Letters*, vol. 7, article 337, 2012.
- [19] Y. Shigemasa and S. Minami, "Applications of chitin and chitosan for biomaterials," *Biotechnology and Genetic Engineering Reviews*, vol. 13, pp. 383–420, 1996.

- [20] M. J. Laudenslager, J. D. Schiffman, and C. L. Schauer, "Carboxymethyl chitosan as a matrix material for platinum, gold, and silver nanoparticles," *Biomacromolecules*, vol. 9, no. 10, pp. 2682–2685, 2008.
- [21] I. Wedmore, J. G. McManus, A. E. Pusateri, and J. B. Holcomb, "A special report on the chitosan-based hemostatic dressing: experience in current combat operations," *Journal of Trauma-Injury, Infection and Critical Care*, vol. 60, no. 3, pp. 655–658, 2006.
- [22] X. Sun, G. Zhang, D. Patel, D. Stephens, and A. M. Gobin, "Targeted cancer therapy by immunoconjugated gold-gold sulfide nanoparticles using protein G as a cofactor," *Annals of Biomedical Engineering*, vol. 40, no. 10, pp. 2131–2139, 2012.
- [23] X. G. Chen and H. J. Park, "Chemical characteristics of O-carboxymethyl chitosans related to the preparation conditions," *Carbohydrate Polymers*, vol. 53, no. 4, pp. 355–359, 2003.
- [24] Y. Y. Liang and L. M. Zhang, "Bioconjugation of papain on superparamagnetic nanoparticles decorated with carboxymethylated chitosan," *Biomacromolecules*, vol. 8, no. 5, pp. 1480–1486, 2007.
- [25] G. Zhang, J. B. Jasinski, D. Patel, K. James, X. Sun, and A. M. Gobin, "Gold nanoparticles with tuning near infrared absorption via reaction of HAuCl_4 and $\text{Na}_2\text{S}_2\text{O}_3$ for low power photothermal cancer therapy," *MRS Proceedings*, vol. 1416, 2012.
- [26] A. M. Gobin, E. M. Watkins, E. Quevedo, V. L. Colvin, and J. L. West, "Near-infrared-resonant gold/gold sulfide nanoparticles as a photothermal cancer therapeutic agent," *Small*, vol. 6, no. 6, pp. 745–752, 2010.
- [27] H. Huang and X. Yang, "Synthesis of chitosan-stabilized gold nanoparticles in the absence/presence of tripolyphosphate," *Biomacromolecules*, vol. 5, no. 6, pp. 2340–2346, 2004.
- [28] D. S. Dos Santos, P. J. G. Goulet, N. P. W. Pieczonka, O. N. Oliveira, and R. F. Aroca, "Gold nanoparticle embedded, self-sustained chitosan films as substrates for surface-enhanced Raman scattering," *Langmuir*, vol. 20, no. 23, pp. 10273–10277, 2004.
- [29] P. R. Selvakannan, S. Mandal, S. Phadtare, R. Pasricha, and M. Sastry, "Capping of gold nanoparticles by the amino acid lysine renders them water-dispersible," *Langmuir*, vol. 19, no. 8, pp. 3545–3549, 2003.
- [30] K. H. Su, Q. H. Wei, X. Zhang, J. J. Mock, D. R. Smith, and S. Schultz, "Interparticle coupling effects on plasmon resonances of nanogold particles," *Nano Letters*, vol. 3, no. 8, pp. 1087–1090, 2003.
- [31] S. K. Ghosh and T. Pal, "Interparticle coupling effect on the surface plasmon resonance of gold nanoparticles: from theory to applications," *Chemical Reviews*, vol. 107, no. 11, pp. 4797–4862, 2007.
- [32] E. Guibal, "Interactions of metal ions with chitosan-based sorbents: a review," *Separation and Purification Technology*, vol. 38, no. 1, pp. 43–74, 2004.
- [33] Z. P. Zhao, Z. Wang, and S. C. Wang, "Formation, charged characteristic and BSA adsorption behavior of carboxymethyl chitosan/PES composite MF membrane," *Journal of Membrane Science*, vol. 217, no. 1-2, pp. 151–158, 2003.

Research Article

Influence of Lauro lactam Content on the Clay Intercalation of Polyamide 6,12/Clay Nanocomposites Synthesized by Open Ring Anionic Polymerization

**E. N. Cabrera Álvarez, L. F. Ramos de Valle,
F. J. Rodríguez González, F. Soriano-Corral, and R. E. Díaz De León**

Polymer Processing Department, Centro de Investigación en Química Aplicada (CIQA), Boulevard Enrique Reyna, No. 140, 25294 Saltillo, COAH, Mexico

Correspondence should be addressed to E. N. Cabrera Álvarez, enazareo@posgrado.ciqa.mx and L. F. Ramos de Valle, devalle@ciqa.mx

Received 4 May 2012; Accepted 23 July 2012

Academic Editor: Sadhan C. Jana

Copyright © 2012 E. N. Cabrera Álvarez et al. This is an open access article distributed under the Creative Commons Attribution License, which permits unrestricted use, distribution, and reproduction in any medium, provided the original work is properly cited.

In situ anionic homo- and copolymerization of caprolactam (CL) and lauro lactam (LL) with sodium montmorillonite clay (NaMMT) was carried out using two different initiators, sodium caprolactamate (CLNa) and caprolactam magnesium bromide (CLMgBr). Degree of conversion and final molecular weight were used to assess the advancement and efficiency of the polymerization reaction and X-ray diffraction and electron microscopy were used to evaluate the sodium montmorillonite clay intercalation/exfoliation. The use of CLNa as initiator produced a higher conversion degree and molecular weight than the use of CLMgBr. Through DSC, it was observed that CLNa and CLMgBr tended to produce random and block copolymer structures, respectively, and either random or block, this eventually has an effect on the clay dispersion within the polymer matrix. In all cases, increasing the LL content produced a decrease in the conversion degree and in the molecular weight of the resulting polymer.

1. Introduction

Fast-activated anionic polymerization has been successfully used for the polymerization of lactams. The intended high-polymerization rate of the anionic polymerization is achieved by introducing an activator, which is a compound containing an N-acyllactam structure. In this sense, sodium hydride in caprolactam [1] and sodium caprolactamate (CLNa) [2] have been used as initiators for the initiation stage.

The technology of the *in situ* polymerization with sodium montmorillonite clay (NaMMT) was first established at the Toyota laboratories via the hydrolytic polymerization of ϵ -caprolactam intercalated in a complex of 12-aminododecanoic acid-NaMMT, in order to obtain a polyamide 6/clay nanocomposite (PA6/Clay) [3, 4]. Combination of the

in situ polymerization techniques with the anionic polymerization of lactams has been reported, where polyamide nanocomposites are readily obtained [5, 6]. Jung et al. [7] recently reported the obtaining of PA6/Clay nanocomposites via the *in situ* anionic polymerization of caprolactam (CL) with clay, using CLNa as initiator and N-acetyl-caprolactam (ACL) as activator. While studying the synthesis of PA6/clay nanocomposites, Liu et al. [8] reported that when using NaMMT, they obtained exfoliated nanocomposites whereas when using organomodified montmorillonite they obtained intercalated nanocomposites. Ahmed and Lee [9] studied the effect of clay concentration on the mechanical and viscoelastic properties of PA6/clay nanocomposites synthesized via anionic polymerization.

On the other hand, studies on the synthesis of composites based on the *in situ* anionic copolymerization of CL and

lauro lactam (LL) with NaMMT have not received so much attention. In this sense, Ricco et al. [10] studied the copolymerization of CL with LL, using CLNa and sodium lauro lactamate or a mix of both, as initiators, and found that the greatest conversion resulted when using CLNa. Budín et al. [11] studied the anionic copolymerization of CL with LL using either, CLNa or caprolactam magnesium bromide (CLMgBr) as initiators, and found that when using CLNa, there was a tendency to produce random copolymers, whereas when using CLMgBr, the tendency was to produce block copolymers. Although, the structure type of the copolymer was also dependant on the temperature of reaction and on the monomers molar ratio.

The purpose in this work, therefore, was to study the effect of the initiator type on the conversion degree and molecular weight of the final polymer, as well as the effect of the copolymer structure on the clay intercalation-exfoliation.

2. Experimental

2.1. Material. The materials used in this study were caprolactam (CL), from Univex; lauro lactam (LL), from Aldrich; sodium caprolactamate (CLNa) in Caprolactam at 18.5 wt% concentration from Brüggemann Chemicals; caprolactam magnesium bromide (CLMgBr) in caprolactam at 17 wt% concentration from Brüggemann Chemicals; N-acetyl caprolactam (ACL) from Aldrich; sodium montmorillonite clay (NaMMT) from Southern Clay Inc.

2.2. Copolymerization. The *in situ* anionic polymerization was carried out in test tubes, where CL, LL, or a mix of both were introduced and heated to 180°C. Thereafter, 0.5 mol% of CLNa or CLMgBr was added as initiator, then, 2 wt% of NaMMT was added, and finally, 0.5 mol% of N-acetyl caprolactam was added as activator, all percentages with respect to the total mols of CL + LL. The reaction was allowed to proceed for 30 min in a nitrogen atmosphere. The copolymerizations of CL with LL were carried out using 100/0, 80/20, 60/40, 40/60, 20/80, and 0/100 mol% of CL/LL, respectively. Nanocomposites obtained were then grounded, purified through Soxhlet extraction with methanol, and vacuum-dried at 110°C for 8 hours.

2.3. Characterization. Conversion was determined gravimetrically by Soxhlet extraction with methanol of the material from the test tubes, where the reaction took place, for 24 hours, using a 2:1 methanol-water mixture as the solvent, in order to extract the unreacted monomers and initiators. Thereafter, the remaining material in the Soxhlet tube was dried at 110°C until constant weight. The conversion was taken as the final weight in the Soxhlet divided by the initial weight and multiplied by 100.

An Alliance 2695 Gel Permeation Chromatograph, with a UV detector model 2487 (248 nm) and styragel columns, was used to determine the evolution of molecular weight of all samples. Samples were first dissolved in trifluoroacetic acid and run in the GPC at a flow rate of 1 mL/min.

X-ray diffraction (XRD) analyses were carried out in a Siemens D5000 using an anode of CuK α X-ray of 1.54 Å at

35 Kv and 25 mA. Samples were scanned at diffraction angles from 2 to 12° in $2(\theta)$. Runs were performed with a step size of 0.02° and step time of 1.0 s. Bragg's law ($n\lambda = 2d \sin\theta$) was used to convert the data of diffraction angle (2θ) to distance (d). Samples for X-ray analysis were obtained from the compression molded process.

Differential Scanning Calorimetry (DSC) analysis was performed on a TA Instruments 2920 Modulated DSC to establish the thermal transitions and structural characteristics of all samples. Samples of ca 10 mg were analyzed under a nitrogen atmosphere. Thermal analysis was carried out as follows: samples were first heated up to 250°C at a heating rate of 10°C/min and then cooled down to 0°C at -10°C/min. Finally, samples were heated again up to 250°C at 10°C/min.

The clay structural organization was studied through STEM observations using a Jeol-JSM7104F electron microscope equipped with STEM modulus and a field emission gun, at an accelerating voltage of 30 kV, using a LEI (low electron image) detector. Ultrathin sections for STEM analysis were previously cut from compression molded samples with a diamond knife at -30°C using a Leica cryogenic ultramicrotome.

3. Results and Discussion

3.1. Physicochemical Properties. Figure 1 shows the conversion and molecular weight of the *in situ* anionic homo- and copolymerizations of CL, LL, and CL with LL, respectively. The NaMMT content was kept at 2 wt%. All polymerizations were carried out for 30 min, using either CLNa or CLMgBr as initiators.

It can be observed in Figure 1(a), that the highest conversion was achieved during the homopolymerization of CL for obtaining polyamide 6/NaMMT (PA6/NaMMT), independently of the initiator used. Also, it was observed that conversion decreased as the LL/CL ratio increased in the nanocomposites of poly (caprolactam-co-lauro lactam)/NaMMT (PA6:12/NaMMT), but this seems to be dependent on the initiator used, since conversion was higher when using CLNa as initiator at all LL/CL ratios, except above ca. 90/10. This diminished catalytic activity of CLMgBr, as compared to CLNa, is attributed to the steric hindrance of the larger CLMgBr molecular size.

Figure 1(b) shows that in all cases, the molecular weight of the resulting homo- or copolymer was greater when using CLNa as initiator. Additionally, with any of the two initiators, the molecular weight of the homopolymers was greater than that of the copolymers, showing a minimum when the LL content was ca. 60 mol%.

As expected, upon increasing the LL concentration, the molecular weight decreases. This is attributed to the much lower reactivity of the LL anions, as compared to those of CL [12]. These results coincide with those reported by Budín et al. [11], while studying the polymerization of CL or LL, without clay.

In all cases, CLNa produced a greater conversion and also a greater molecular weight, which coincides with Odian [13], who mentions that the ring opening anionic polymerization

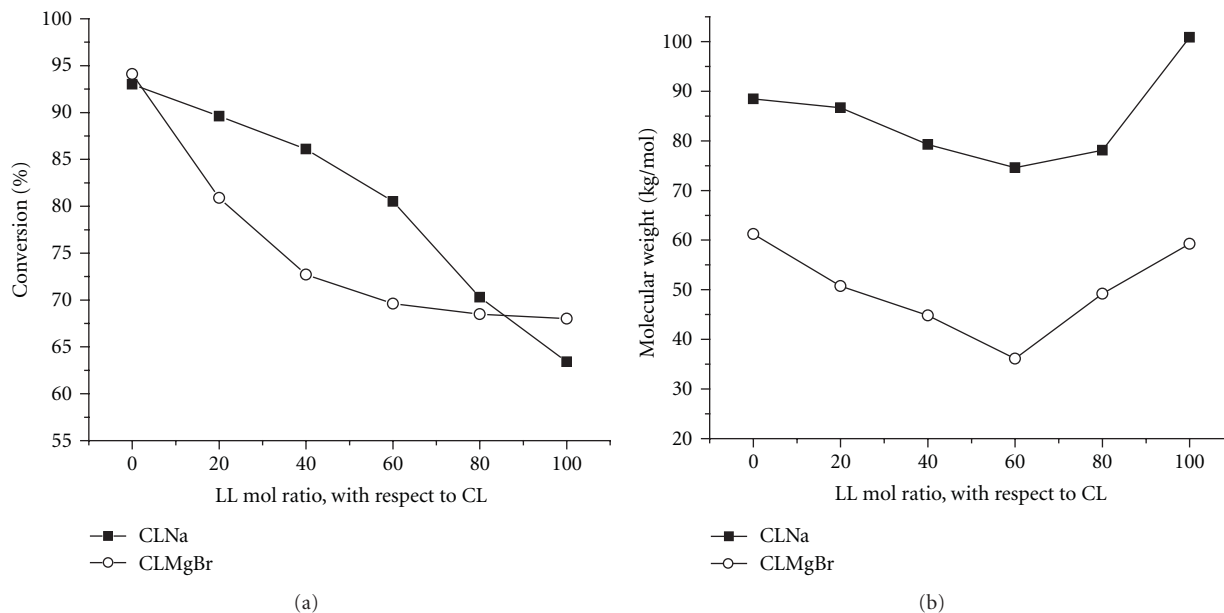


FIGURE 1: Effect of initiator type (CLNa or CLMgBr) and LL mol ratio on (a) conversion and (b) molecular weight during the *in situ* homo- and copolymerization of CL, LL, and CL/LL, with 2 wt% of NaMMT.

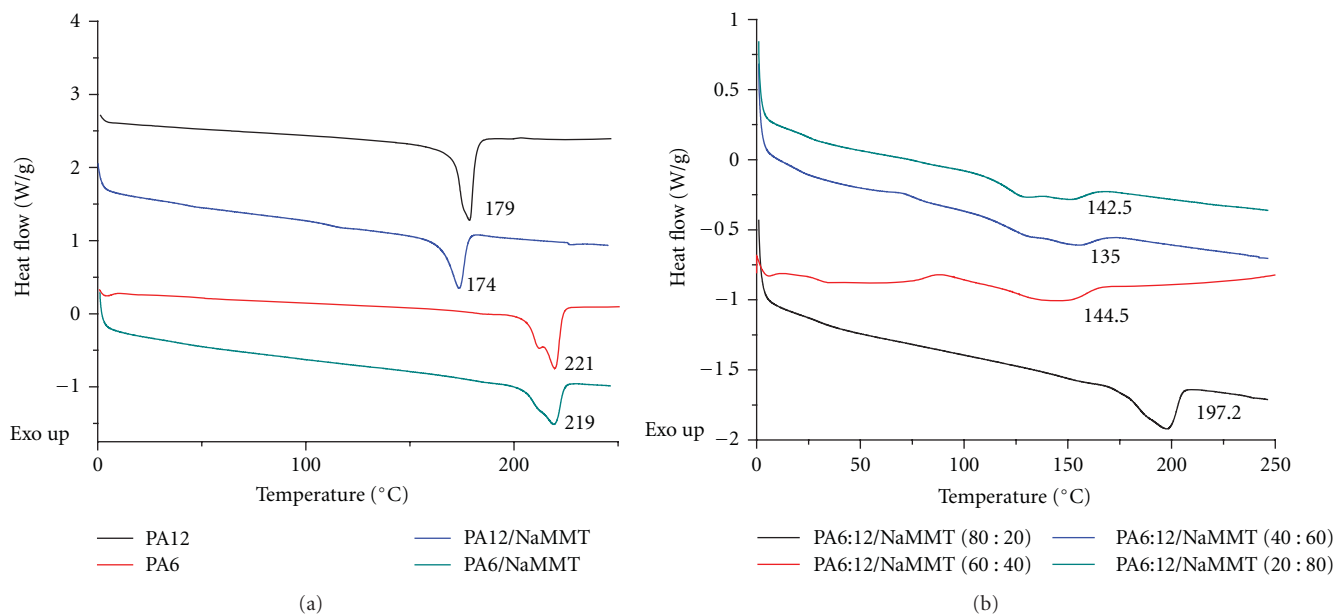


FIGURE 2: DSC curves for (a) homopolymers with and without MMT and (b) nanostructured copolymers of PA6:12 (at with 2 wt% of nanoclay). The initiator used in this case was CLNa.

proceeds in a way that the attained molecular weight varies linearly with conversion.

In addition, the greater molecular weights, when using CLNa, were indirectly assumed, as it was observed that during the copolymerization (CL/LL), the magnetic stirrer ceased turning after just 20 s of reaction when using CLNa, due to the viscosity increase, as a result of a greater molecular weight; whereas it took 35 s when using CLMgBr.

3.2. Thermal Properties. Figure 2 presents the effect of composition of the nanostructured polymeric compounds on the fusion temperature T_m . First, from Figure 2(a), it can be observed that the T_m of the homopolymer compounds is not altered significantly, by the inclusion of the NaMMT, it remains at 221°C ($\pm 1^\circ\text{C}$) for PA6/NaMMT and 179°C for Polyamide 12/NaMMT (PA12/NaMMT), in agreement with that reported elsewhere [14]. Second, from Figure 2(b),

TABLE 1: Fusion temperature (T_m) and enthalpy of fusion (ΔH_m) of the obtained homo- and copolymer compounds of CL and LL with NaMMT, using CLNa and CLMgBr.

| Using CLNa as initiator | LL concentration (% mol) | T_m ($^{\circ}\text{C}$) | | ΔH_m (J/g) | |
|---------------------------|--------------------------|---------------------------------|---------------------------------|-----------------------|-----------------------|
| PA6/NaMMT | 0 | 219.3 | | 42.2 | |
| | 20 | 197.2 | | 35.1 | |
| | 40 | 144.5 | | 19.9 | |
| PA6:12/NaMMT | 60 | 135.0 | | 22.1 | |
| | 80 | 142.5 | | 21.7 | |
| | 100 | 174.0 | | 35.1 | |
| Using CLMgBr as initiator | LL concentration (% mol) | T_{m1} ($^{\circ}\text{C}$) | T_{m2} ($^{\circ}\text{C}$) | ΔH_{m1} (J/g) | ΔH_{m2} (J/g) |
| PA6/NaMMT | 0 | 219.5 | — | 44.8 | — |
| | 20 | 201.8 | 183.5 | 7.3 | 26.5 |
| PA6:12/NaMMT | 40 | 175.2 | 154.3 | 4.1 | 15.8 |
| | 60 | 152.6 | 131.4 | — | 21.7 |
| | 80 | 149.9 | 145.6 | 11.3 | 21.2 |
| PA12/NaMMT | 100 | — | 172.3 | — | 31.5 |

the T_m of the copolymer PA6:12/NaMMT compounds, on the other hand, decreased as the concentration of LL increased, reaching a minimum (135°C) at a LL content of 60 mol%.

It is also observed that the fusion temperature of the copolymers is below that of the two homopolymers. This abatement is attributed to alpha and gamma crystalline phases of Polyamide 6 (PA6) and Polyamide 12 (PA12), respectively, trying to coexist in the copolymers, as reported by Budín et al. [11]. As the LL concentration increases, the alpha crystalline phase of PA6 tends to coexist with the gamma crystalline phase of PA12, generating many crystallite imperfections. On the other hand, upon increasing the LL content in the copolymers, the crystal size and the crystalline content decrease, decreasing the fusion temperature, as reported by Kubota and Nowell [15].

Finally, it can also be observed in Figure 2(b) that the crystallinity (associated with the fusion enthalpy ΔH_m) of the copolymer compounds is less than that of the homopolymers and it decreases with the concentration of LL, as can be determined from the enthalpies of fusion (Table 1).

Figure 3 shows the thermograms of the copolymers obtained using a CL/LL composition equal to 40/60. An important difference observed in the copolymers, when comparing that obtained with CLNa versus that obtained with CLMgBr initiator, is that, when using CLNa, the copolymer shows just one fusion peak, at 144.5°C . This is indicative of a random copolymer. When using CLMgBr, on the other hand, the copolymer shows two fusion peaks, at 154.2 and 175.2°C . This, on the other hand, is indicative of a block copolymer. These present a fair agreement with results reported by Budín et al. [11].

With respect to the fusion temperatures of the synthesized block copolymers, when using CLMgBr, it can be assumed that one block is a random block of CL (PA6) and LL (PA12) units. This randomness would hinder the formation of regular-perfect crystals, resulting in a diminished crystalline fusion temperature. The other block, on

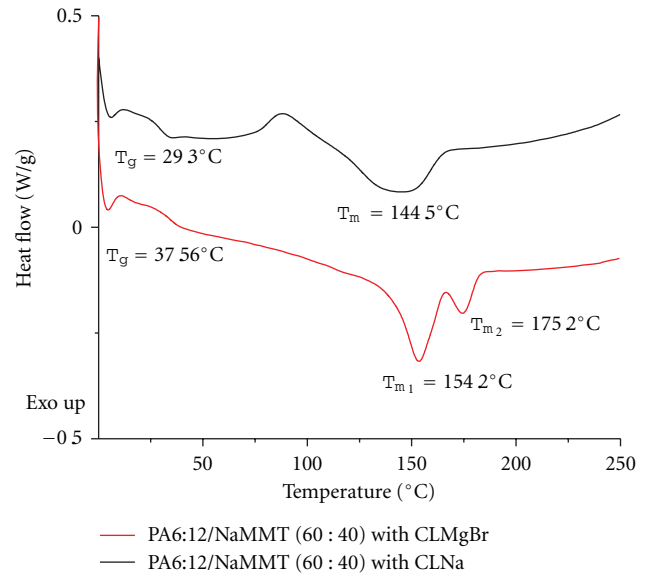


FIGURE 3: DSC curves of the two nanostructured polymer compounds of PA6:12, with CL/LL ratio of 60/40, obtained with CLNa and with CLMgBr as initiators.

the other hand, would be composed mostly of CL units, though not sufficiently long as to show the T_m of the PA6 homopolymer, but sufficiently long as to permit the formation of more regular-perfect crystals, with higher crystalline fusion temperature.

In addition, the insertion of the long aliphatic chains of PA12 into the structure of the PA6 in the growing PA6/PA12 copolymer chains, would give rise to a change in the crystalline type, from alpha, typical of PA6, to gamma, typical of PA12. These changes in the crystalline structure of PA would also tend to abate the fusion temperature, as has been reported elsewhere [16]. Table 1 presents the fusion temperature (T_m) and the enthalpy of fusion (ΔH_m) for all the nanostructured polymer compounds studied, using

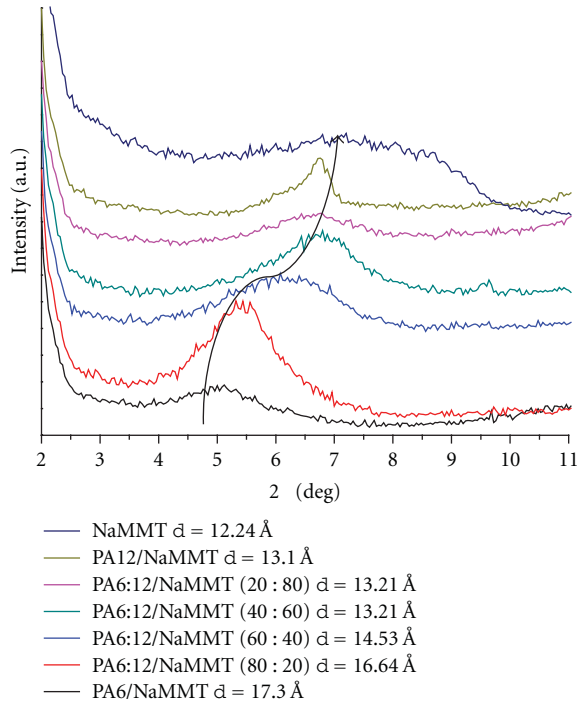


FIGURE 4: X-Ray diffraction curves of the homo- and copolymers of CL and LL, with 2 wt% of nanoclay, obtained using CLNa as initiator.

either CLNa or CLMgBr as initiators. It can be observed that the fusion temperature and the enthalpy of fusion of the copolymers are clearly affected by the increasing concentration of LL, as reported by Ricco et al. [10].

As an outcome, it can be said that the initiator type is the one that determines if the result is going to be a random or a block copolymer. In addition, the effect of LL content upon the fusion temperature of the copolymer is the same, no matter if the initiator is CLNa or CLMgBr. Finally, the addition of NaMMT has no apparent effect on the homopolymers fusion temperature (PA6 221°C; PA12 179°C) as shown in Figure 2(a).

3.3. Exfoliation and Dispersion of the Nanoclay. For the case of the polyamide/clay nanocompounds obtained using CLNa as initiator, Figure 4 shows that all the nanocompounds present a progressive shift of the X-Ray diffraction peak to lower 2θ , with respect to that of the pure NaMMT. This indicates an increase in the gallery spacing, producing an intercalated structure, attributed primarily to the insertion of the CL and LL monomeric units into the clay galleries prior to the *in situ* polymerization. It is important to bear in mind that when using CLNa as initiator, there is a tendency to produce random type copolymers.

In Figure 4, it can also be observed that the diffraction peak of the PA6/NaMMT nanocompound occurs at the lowest 2θ angle, which would correspond to the largest intergallery spacing (17.3 Å). On the contrary, the peak of the PA12/NaMMT nanocompound occurs at the highest

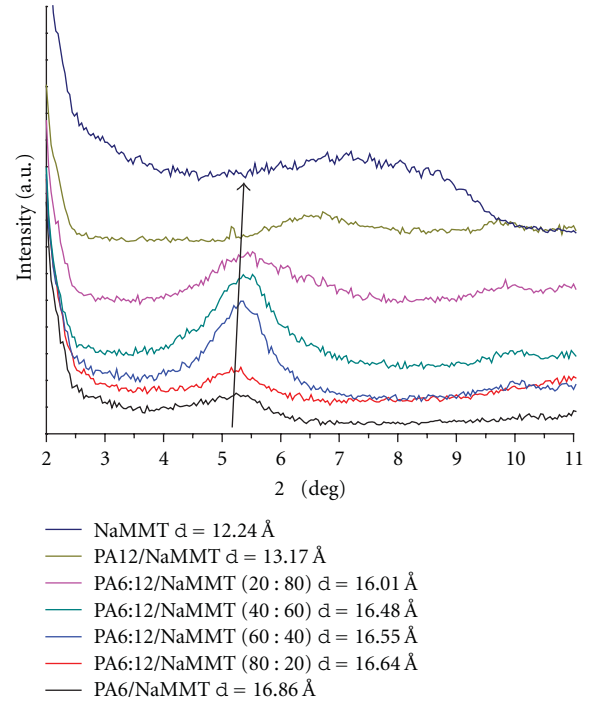


FIGURE 5: X-Ray diffraction curves of the homo- and copolymers of CL and LL, with 2 wt% of nanoclay, obtained using CLMgBr as initiator.

2θ angle, corresponding to the smallest intergallery spacing (13.1 Å).

In all the PA6:12/NaMMT nanocompounds, the peak occurs at higher 2θ angles as the LL content increases. That is, the intergallery spacing diminishes with the concentration of LL. These differences can be attributed to the lower polarity of PA12, compared to that of PA6, due to the longer aliphatic, nonpolar segments (12 C atoms) along its chains, as compared to the shorter aliphatic segments (6 C atoms) in the PA6 chains. That is, for a given polymer chain length, the PA12 shows a smaller content of the polar amide groups than the PA6. This diminished polarity of the PA12 chains makes them less compatible to the highly polar NaMMT. Thus, the decreasing intergallery spacing with increasing LL content, up to the smallest spacing for the PA12/NaMMT nanocompound.

For the case of the polyamide/clay nanocompounds obtained using CLMgBr as initiator, Figure 5 shows that all the nanocompounds present the same shift of the X-Ray diffraction peak to lower 2θ , which would correspond to an intergallery spacing of ca. 16.5 Å, with the exception of the PA12/NaMMT nanocompound, which presents an intergallery spacing of 13 Å.

When using CLMgBr as initiators, there is no effect of the LL content on the 2θ angle of the X-ray diffraction peak, as observed in Figure 4. This no-effect is assumed to be due to the block copolymer structure formed when using CLMgBr as initiator, in which case, the CL short blocks act as the highly polar PA6 homopolymer does and shows the

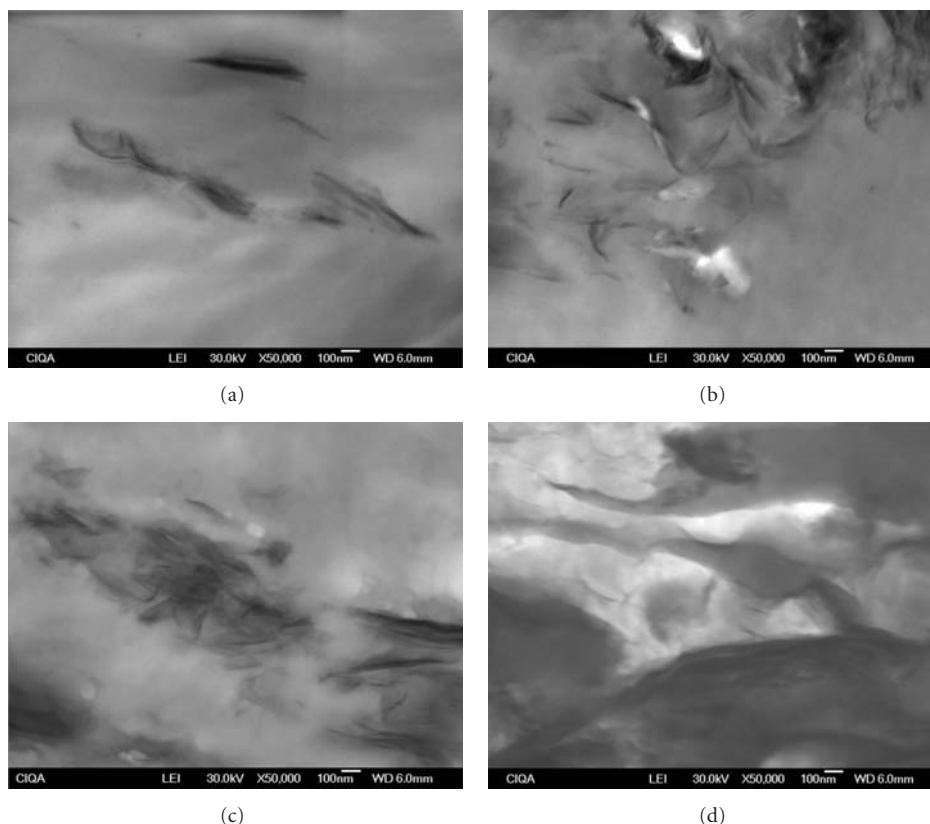


FIGURE 6: Electron micrographs of (a) PA6/NaMMT, (b) PA6:12/NaMMT (80 : 20), (c) PA6:12/NaMMT (60 : 40), and (d) PA12/NaMMT obtained with CLMgBr (scale bar at 100 nm).

capability to intercalate into the clay galleries, as the highly polar PA6 homopolymer does.

The micrographs in Figures 6(a), 6(b), and 6(c) show similar levels of exfoliation/intercalation, but not that in Figure 6(d), which corresponds to the PA12/NaMMT homopolymer compound, where very little or no exfoliation/intercalation is obtained. These results agree with those obtained via the XRD analysis, where the PA6/NaMMT as well as all the PA6:12/NaMMT copolymers prepared in the presence of CLMgBr initiator, present the same intergallery spacing of ca. 16.5 Å, with the exception of the PA12/NaMMT homopolymer.

The incomplete clay exfoliation, even though the high affinity between the highly polar PA6 and NaMMT, can be attributed to the lack of application of any shear stresses during the preparation of the nanostructured PA compounds. It might be expected that the preparation of the same PA compounds, via reactive extrusion, could render a much higher level of clay exfoliation.

4. Conclusions

Homo- and copolyamide type nanocompounds were obtained, via *in situ* anionic polymerization of caprolactam and lauro lactam with NaMMT, using two initiator types.

The use of CLNa as initiator tended to produce a random-type copolymer, whereas the use of CLMgBr tended to produce a block-type structure, which affected both the crystallinity of the copolymers and the intercalation/exfoliation of the nanoclay. In the random type copolymers, the intergallery spacing decreased with the LL content, whereas in the block type copolymer, the intergallery spacing remained the same (as that for PA6) for all the copolymers. The intergallery spacing of the PA12/NaMMT remained the lowest in all cases. The use of CLNa as initiator produced a higher conversion degree and higher molecular weight than the use of CLMgBr.

In all cases, increasing the LL content produced a decrease in the conversion degree and in the molecular weight of the resulting polymer compound.

Crystallinity of the copolymer compounds was found to be less than that of the homopolymers. Also, crystallinity was greatly affected by the LL concentration; as the LL concentration increased, crystallinity decreased, as observed from the enthalpies of fusion.

Acknowledgments

The authors thank CONACYT for its financial support to carry out this study through project 84424. And the authors

thank M. Sanchez, J. F. Zendejo, E. Hurtado-Suarez, and P. Siller-Flores for their technical support.

References

- [1] I. Kim and J. L. White, "Anionic copolymerization of lauryl lactam and polycaprolactone to produce polyesteramide triblock copolymer," in *Proceedings of the 61st Annual Technical Conference ANTEC 2003*, pp. 1653–1657, May 2003.
- [2] E. Šimůnková, J. Zelinger, V. Kubanek, and J. Kralicek, "The structure and physical properties of copolymers of lactams," *Journal of Applied Polymer Science*, vol. 21, no. 1, pp. 65–81, 1977.
- [3] A. Okada, Y. Fukushima, M. Kawasumi et al., "Composite material and process to manufacturing same," 4, 739, 007 US Patent, 1988.
- [4] M. Kawasumi, M. Kohzaki, Y. Kojima, A. Okada, and O. Kamigaito, "Process for producing composite material," 4, 810, 734 US Patent, 1989.
- [5] Y. Kojima, A. Usuki, M. Kawasumi, A. Okada, T. Kurauchi, and O. Kamigaito, "Synthesis of nylon 6-clay hybrid by montmorillonite intercalated with ϵ -caprolactam," *Journal of Polymer Science A*, vol. 31, no. 4, pp. 983–986, 1993.
- [6] A. Usuki, M. Kawasumi, Y. Kojima, A. Okada, T. Kurauchi, and O. Kamigaito, "Swelling behavior of montmorillonite cation exchanged for ω -amino acids by ϵ -caprolactam," *Journal of Materials Research*, vol. 8, no. 5, pp. 1174–1178, 1993.
- [7] H. P. Jung, N. K. Woo, H. S. Kye et al., "Disordering of clay layers in the nylon 6/clay nanocomposites prepared by anionic polymerization," *Macromolecular Research*, vol. 13, no. 5, pp. 367–372, 2005.
- [8] A. Liu, T. Xie, and G. Yang, "Comparison of polyamide-6 nanocomposites based on pristine and organic montmorillonite obtained via anionic ring-opening polymerization," *Macromolecular Chemistry and Physics*, vol. 207, no. 13, pp. 1174–1181, 2006.
- [9] R. Ahmed and S. J. Lee, "Polyamide-clay nanocomposites and their non-linear viscoelastic characterization," *Journal of Advanced Materials*, vol. 2, pp. 127–133, 2007.
- [10] L. Ricco, S. Russo, G. Orefice, and F. Riva, "Caprolactam-lauro lactam copolymers: fast activated anionic synthesis, thermal properties and structural investigations," *Macromolecular Chemistry and Physics*, vol. 202, no. 10, pp. 2114–2121, 2001.
- [11] J. Budín, J. Brožek, and J. Roda, "Polymerization of lactams, 96* anionic copolymerization of ϵ -caprolactam with ω -lauro lactam," *Polymer*, vol. 47, no. 1, pp. 140–147, 2006.
- [12] T. M. Frunze, V. A. Kotel'nikov, V. V. Kurashev, S. L. Ivanova, L. I. Komarova, and V. V. Korshak, "The relative reactivities of ϵ -caprolactam and ω -dodecalactam in activated anionic copolymerization," *Polymer Science U.S.S.R.*, vol. 18, no. 2, pp. 348–353, 1976.
- [13] G. Odian, *Principles of Polymerization*, Wiley Intersciences, 3rd edition, 1991.
- [14] J. Brandrup, E. H. Immergut, E. A. Grulke, A. Abe, and D. R. Bloch, *Polymer Handbook*, John Wiley & Sons, 4th edition, 2003.
- [15] H. Kubota and J. B. Nowell, "Changes in the morphology of cast nylon 6 through copolymerization," *Journal of Applied Polymer Science*, vol. 19, no. 6, pp. 1521–1538, 1975.
- [16] D. P. Garner and P. D. Fasulo, "Effect of composition on the properties of nylon 612 copolymers," *Journal of Applied Polymer Science*, vol. 36, no. 3, pp. 495–509, 1988.

Research Article

Electrically Conductive Compounds of Polycarbonate, Liquid Crystalline Polymer, and Multiwalled Carbon Nanotubes

Penwisa Pisitsak,^{1,2} Rathanawan Magaraphan,¹ and Sadhan C. Jana³

¹ Polymer Processing and Polymer Nanomaterials Research Unit, The Petroleum and Petrochemical College, Chulalongkorn University, Bangkok 10330, Thailand

² Department of Textile Science and Technology, Faculty of Science and Technology, Thammasat University, Rangsit Center, Pathum Thani 12121, Thailand

³ Department of Polymer Engineering, University of Akron, Akron, OH 44325-0301, USA

Correspondence should be addressed to Rathanawan Magaraphan, rathanawan.k@chula.ac.th

Received 24 April 2012; Revised 12 July 2012; Accepted 29 July 2012

Academic Editor: Suprakas Sinha Ray

Copyright © 2012 Penwisa Pisitsak et al. This is an open access article distributed under the Creative Commons Attribution License, which permits unrestricted use, distribution, and reproduction in any medium, provided the original work is properly cited.

A thermotropic liquid crystalline polymer (LCP) was blended with polycarbonate (PC) and multiwalled carbon nanotube (CNT) with the goal of improving electrical conductivity and mechanical properties over PC. The LCP was anticipated to produce fibrillar domains in PC and help improve the mechanical properties. The study was carried out using two grades of LCP—Vectra A950 (VA950) and Vectra V400P (V400P). The compounds contained 20 wt% LCP and 0.5 to 15 wt% CNT. The compounds were prepared by melt-blending in a twin-screw minicomponenter and then injection molded using a mini-injection molder. The fibrillar domains of LCP were found only in the case of PC/VA950 blend. However, these fibrils turned into droplets in the presence of CNT. It was found that CNT preferentially remained inside the LCP domains as predicted from the value of spreading coefficient. The electrical conductivity showed the following order with the numbers in parenthesis representing the electrical percolation threshold of the compounds: PC/CNT (1%) > PC/VA950P/CNT (1%) > PC/V400P/CNT (3%). The storage modulus showed improvements with the addition of CNT and VA950.

1. Introduction

Over the last two decades, blends of thermoplastic polymers with liquid crystalline polymer (LCP) received considerable interests from both academic and industrial researchers. The dispersed LCP domains tend to elongate during melt processing and subsequently form aligned fibrils capable of reinforcing the matrix polymer. The aligned fibril formation in these *in situ composites* greatly depended on the choice of polymer matrix and the selection of proper processing conditions. The droplets, short fibrils, networks of droplets and fibrils, and continuous fibrous LCP structures in thermoplastic polymers have been reported [1–7]. The research on *in situ composites* mainly dealt with unique morphology and consequent enhancement of mechanical properties, while those addressing the electrical properties are limited [8–10]. In this context, introduction of carbon

nanotubes (CNTs) in thermoplastic polymer/LCP blends can offer additional improvements in mechanical properties in addition to offering excellent electrical and thermal conductivity. However, high cost and limited availability of CNTs often serve as deterrent to development of more widespread applications of composites containing CNTs. In this study, CNTs were introduced in blends of polycarbonate (PC) and LCP with the aim of obtaining synergistic effects, such as strong mechanical properties from fibrillar LCP domains and electrical conductivity from CNTs. The interplay of CNTs with the morphology of PC/LCP blends or the possibility of selective localization of CNTs in PC or LCP was not known a priori. A summary of existing literature on electrically conductive immiscible blends, especially those of carbon black, carbon nanofibers (CNFs), and CNTs is presented below.

Immiscible polymer blend systems have been effectively used in the production of electrically conductive composites via preferential localization of the conductive fillers, for example, carbon black, in one of the phases [11–14]. This gives rise to double percolation—whereby electrically conductive percolation networks develop in one of the cocontinuous phases. This phenomenon was mostly observed for blends with close to 50:50 weight ratios of the component polymers. Dharaiya and coworkers recently exploited chaotic mixing conditions to produce fibrillar morphology of polypropylene (PP) in blending of 90 parts by weight of polyamide 6 (PA6) with 10 parts by weight of PP and used the cocontinuous fibrils of PP to obtain electrically conductive PP/PA6 compounds at only 1 wt% conductive grade carbon black [15].

Other researchers also exploited the preferential localization concept in immiscible blends filled with carbon nanofibers [16, 17], or CNTs [18–21], and reported success in terms of much reduced electrical percolation threshold compared to individual polymer compounds. A schematic representation of the double percolation phenomenon involving CNTs is shown in Figure 1. Pötschke et al. [18, 19] studied electrical conductivity of polycarbonate (PC)/polyethylene blends filled with CNTs and claimed that CNT connected the two polymer phases. The resulting composites showed electrical percolation threshold at 0.41 vol.% CNT. Pötschke et al. [20] used metallocene-based complex for *in-situ* polymerization of ethylene directly from the CNT surface which resulted in good filler dispersion upon blending with polycarbonate and reduced the electrical percolation from 0.75 to 0.25 wt%.

It should be noted that the key factors governing the preferential localization of typical fillers are thermodynamic, kinetic, and polymer melt viscosity [22]. Thermodynamic considerations state that the filler might reside in one of the polymer phases or at the interface as a result of the overall free energy of the existence of three types of interfaces: polymer 1/polymer 2, filler/polymer 1, and filler/polymer 2. Thermodynamically, the filler location might be predicted from the spreading coefficient parameters [23]. Kinetic effects, on the other hand, are related to the mixing process. An equilibrium state of filler dispersion may not be reached in typical mixing experiments due to high viscosity of the polymers. If the system is quenched before reaching an equilibrium state of filler dispersion, incomplete migration of the filler to the thermodynamically favored phase may result [24]. Another important factor is the melt viscosity of the blend component. It has been reported that the melt viscosity factor promotes the localization of filler in a less viscous phase [21, 22, 24].

The concept of selective localization was used in this study to develop electrically conductive *in situ* composites of LCP in PC. It was hypothesized in view of fibrillar domains of LCP that the selective localization of CNTs in the continuous LCP fibrils would facilitate the anisotropic electrical conductivity in PC/LCP blends and consequently reduce the electrical percolation threshold compared to PC/CNT composites. Continuous fibrils of LCP have been observed previously in blends of polycarbonate [2], polypropylene [25], poly(ether

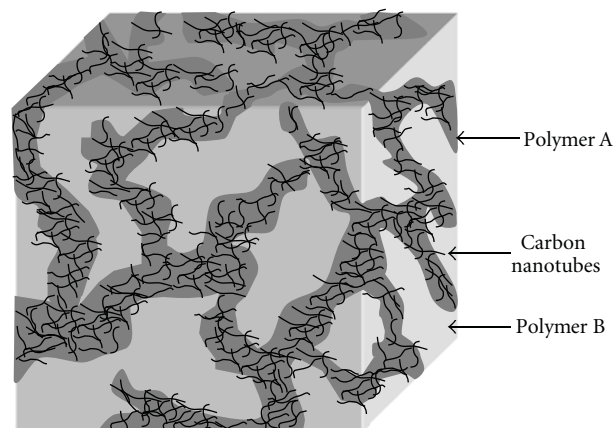


FIGURE 1: Schematic showing double percolation phenomena for carbon black-containing polymer composites.

imide) [26], and polyamide 66 [3], with LCP content in the range of 15–35 wt%. Mukherjee et al. [27] recently reported improvements in mechanical properties of PC/LCP blends in the presence of up to 5 wt% carboxylated CNTs and attributed such improvements to compatibilization effects produced by hydrogen bonding interactions between the COOH groups on CNTs and the carbonyl groups in PC and LCP. These authors observed much smaller droplets of LCP phase with the increase of CNT concentration. Although not explicitly stated in their paper, such interactions would be most effective if carboxylated CNTs remained at the PC-LCP interfaces. Electrical conductivity also showed an increase from an insulator at 1 wt% loading of carboxylated CNT to conductive composite with volume electrical conductivity of approximately 5.5×10^{-3} S/cm and 6.5×10^{-3} S/cm, respectively, at 3 wt% and 5 wt% CNT. Bose et al. observed higher percolation threshold in the cocontinuous polyamide 6 (PA6)/acrylonitrile-butadiene-styrene (ABS) blends containing CNTs compared to the ABS/CNT composites [28]. They found that the nanotubes preferentially resided in PA6 as PA6 displayed a closer value in surface energy as well as a lower melt viscosity. The authors explained their results in terms of good wettability of CNTs by insulating PA6 that led to the suppression of electrical conductivities observed in the PA6/ABS/CNT system.

In this contribution, PC/LCP blends were produced with 20 wt% LCP and the rheological, morphological, electrical, and mechanical properties of the resultant PC/LCP/CNT composites were characterized. The morphological changes in the blends caused by the introduction of CNTs were related to the changes in viscosity and the consequent reduction of electrical conductivity. Several specific questions were answered in this work, which were not addressed in the work of Mukherjee et al. [27, 29]. First, it was not clear from the outset if unmodified CNTs would remain at the interface, move to either the LCP or PC domains, or distribute both in PC and LCP domains in the blend. The images provided in Mukherjee et al. [27] and taken via a high-resolution transmission electron microscope were inconclusive about the location of CNTs. Specific knowledge of CNT localization

TABLE 1: Physical properties of the materials used.

| Materials | Density (g/cm ³) | Glass transition temperature, T_g (°C) | Melting point, T_m (°C) | Melt flow index (g/10 min) |
|-----------|------------------------------|--|---------------------------|--|
| PC | 1.20 | 149.4 | — | 18 (300°C/1.2 kg) |
| V400P | 1.40 | 110 | 225 | 14 (230°C/2.16 kg) |
| VA950 | 1.40 | 100 | 280 | Not available from the supplier ^a |
| CNT | 0.13–0.15 (bulk density) | — | — | — |

^aThe melt flow index of VA950 cannot be measured under the test conditions as stated by the manufacturer.

in LCP or PC domains would in turn help rationalize the trend of electrical conductivity of the blends. Second, the impact of the feeding sequence on the distribution of CNTs in the PC and LCP phases should be examined. Specifically, CNT was first compounded with LCP and the resultant blend was mixed with PC. In another experiment, CNT was compounded first with PC and then with LCP.

2. Experimental

2.1. Materials. Polycarbonate was supplied by SABIC Innovative Plastics (Mt Vernon, IN) as Lexan 121. Two grades of LCPs—VA950 and V400P were obtained from Ticona (Florence, KY). The multiwalled carbon nanotube was obtained in the form of Baytubes, C-150P of approximate diameter 13 nm and length $> 1 \mu\text{m}$ from Bayer MaterialScience (Pittsburgh, PA). A selection of properties of these components is listed in Table 1.

2.2. Composite Preparation. Compounds were prepared in a twin-screw, minicomponenter (HAAKE MiniLab) at 290°C for neat PC and PC/V400P/CNT, and at 300°C for PC/VA950/CNT, with a rotational speed of 60 rpm. All the components were dried in a vacuum oven at 120°C for 8 hrs. The feeding sequence was as follows: PC and CNT were melt-mixed in a minicomponenter for 5 minutes, taken out, then melt-mixed again for 5 minutes with the addition of a certain amount of an LCP. Samples with the prefix “REV” are of the reversed mixing sequence, where CNT was first mixed with LCP followed by mixing the compound with PC. The composite compositions were kept the same in both sequences.

Injection-molded samples were prepared using a mini-injection-molding machine from DSM research with the injection-molding temperature and mold temperature of, respectively, 310°C and 150°C for PC, V400P and PC/V400P/CNT, and 300°C and 80°C for VA950 and PC/VA950/CNT. The injection pressure was $6 \times 10^5 \text{ kg m}^{-1} \text{ s}^{-2}$ for all samples. The injection-molded rectangular bars were cut into the dimensions of 36.0 mm \times

12.0 mm \times 2.0 mm and 30.0 mm \times 6.5 mm \times 2.0 mm for the determination of electrical conductivity and dynamic mechanical properties, respectively. The discs of PC, V400P, and VA950 with 28 mm diameter and 0.8 mm thickness were used in measurements of contact angle.

3. Characterization

The rheological properties of the samples were investigated using ARES (TA Instruments) rotational rheometer. The frequency sweep measurement was performed with 25 mm parallel plate geometry, in oscillatory shear mode, and a fixed strain amplitude of 2%. A Rame-Hart contact angle goniometer (Model 100-00) operating at 1 atm and a temperature of $24 \pm 2^\circ\text{C}$ was used for measurement of contact angle of two reference liquids, di-iodomethane and deionized water. A Keithley sub-Femtoamp Remote SourceMeter four-point conductivity probe (model 6430) was used for measurement of electrical conductivity of the compounds with a current of $10 \mu\text{A}$ for low resistivity samples and a voltage of 100 V for high resistivity samples. The morphology of LCP in PC/LCP/CNT compounds was examined by scanning electron microscopy (SEM, JEOL SM-71510) and transmission electron microscopy (TEM, Tecnai 12 TEM). For this purpose, PC was dissolved by immersing the blends in chloroform at room temperature for 12 h and the LCP residue was recovered by filtration. Therefore, all SEM images presented in this paper show only the LCP phase. The dynamic mechanical analyzer (RSA III) was used to study the mechanical response, such as storage modulus and loss modulus of the samples at temperature ranging from 35°C to 200°C and a heating rate of 4°C/min. These tests were conducted in single point bending mode with a fixed strain of 0.2% and a vibration frequency of 1 Hz.

4. Results and Discussion

4.1. Melt Rheology. The melt rheological response in frequency sweep was recorded at two temperatures according to the injection molding conditions, that is, 300°C for the systems comprising of VA950, and at 310°C for those comprising of V400P. As evident in Figures 2(a) and 2(b), at both temperatures, the PC showed Newtonian behavior and both LCPs exhibited non-Newtonian behavior, that is, the complex viscosity ($|\eta^*|$) decreased with increasing frequency. It is widely accepted that fibril formation of the LCP in a thermoplastic matrix is governed by two major factors—the ratio of viscosity of LCP and the matrix polymer and the value of interfacial tension between the polymer components. The LCP with lower viscosity than the matrix polymer tends to deform into fibrils. In other words, the viscosity ratio of less than unity is promising for fibrillation of the LCP phase. In addition, sufficiently low interfacial tension between LCP and the matrix polymer is also required for good fibril formation. Also, the LCP content must be high to yield substantially large LCP domains, which in turn would facilitate elongation of the LCP domains. It was found that the values of $|\eta^*|$ of VA950 at 300°C were slightly

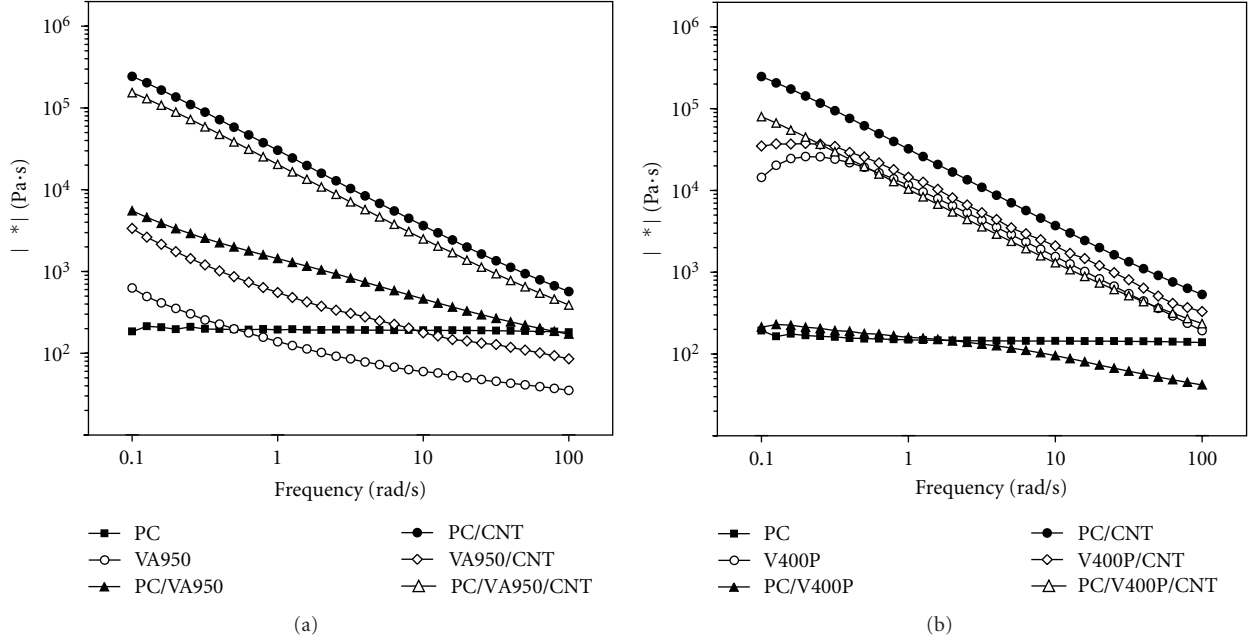


FIGURE 2: Comparison of complex viscosity for PC, PC/LCP blends, and composites with 5 wt% CNT. (a) V400P, measured at 310°C, (b) VA950, measured at 300°C.

greater than those of PC at very low frequencies (from 0.1 to 0.8 rad/s), and lesser at higher frequencies (from 0.8 to 100 rad/s), indicating that the viscosity ratio of VA950 and PC was less than unity during injection molding. The blend of PC with 20 wt% VA950 showed viscosity higher than the individual polymer components. This can be attributed possibly to trans-esterification at the interfaces of PC and VA950 as observed by Tovar et al. [30]. It is also not surprising that the viscosity increased in compounds with the addition of CNTs. The viscosity of PC/VA950 with 5 wt% CNT was slightly lower than PC with 5 wt% CNT and was greater than VA950 with 5 wt% CNT. At 310°C, V400P exhibited the upward concavity at low frequency (Figure 2(b)) which is often found in LCP. The V400P grade of LCP also showed higher viscosity than PC and, therefore, was expected to form spheres instead of fibrils in PC. As expected, the viscosity of this LCP also increased in the presence of CNTs. The viscosity of PC/V400P with 5 wt% CNT was found to be lower than the composites of the corresponding polymer components containing 5 wt% CNT. This can be attributed to the lubricating effect of the V400P domains brought about by immiscibility between a flexible coil-like polymer such as polycarbonate and a rigid-rod LCP as supported by arguments from statistical thermodynamics [31].

4.2. Calculation of Spreading Coefficient. The two-liquid geometric model was used to calculate the surface energy (1) [32, 33] of the polymeric solids with the aid of contact angle measurements:

$$\gamma_{LV}(1 + \cos \theta) = 2(\gamma_S^d \gamma_{LV}^d)^{1/2} + 2(\gamma_S^p \gamma_{LV}^p)^{1/2}. \quad (1)$$

In (1), γ_{LV} and γ_S are the surface energies of the reference liquid and the polymer, respectively, the superscript d refers to the dispersive part and p refers to the polar part, and θ is the measured contact angle. It should be noted that the surface energy is the sum of the dispersion and the polar parts:

$$\gamma = \gamma^d + \gamma^p. \quad (2)$$

The interfacial energies (γ_{12}) can be calculated from the surface energies using two widely used methods—the geometric-mean equation (3) and the harmonic-mean equation (4) [34]:

$$\gamma_{12} = \gamma_1 + \gamma_2 - 2\left(\sqrt{\gamma_1^d \gamma_2^d} + \sqrt{\gamma_1^p \gamma_2^p}\right), \quad (3)$$

$$\gamma_{12} = \gamma_1 + \gamma_2 - 4\left(\frac{\gamma_1^d \gamma_2^d}{\gamma_1^d + \gamma_2^d} + \frac{\gamma_1^p \gamma_2^p}{\gamma_1^p + \gamma_2^p}\right). \quad (4)$$

In (3) and (4), γ_i stands for the surface energy of the component i ($i = 1, 2$), γ_i^d and γ_i^p are the dispersive part and the polar part, respectively. A fairly successful approach to predict the morphology of the blends with a matrix component and two dispersed components was proposed by Harkins [35]. The Harkins equation predicts the tendency of a liquid to spontaneously spread across the solid or liquid substrate using interfacial tension data. It was proposed in a three component system that component 3 encapsulates component 1 if the spreading coefficient λ_{31} given in (5) is positive:

$$\lambda_{31} = \gamma_{12} - \gamma_{32} - \gamma_{13}. \quad (5)$$

In (5), the three terms on the right are the interfacial energies between the respective components. Table 2 shows

TABLE 2: Contact angle of polymers at 25°C.

| Material | Contact angle (degree) | |
|----------|------------------------|-------|
| | Diiodomethane | Water |
| PC | 29.2 | 72.2 |
| V400P | 25.3 | 60.0 |
| VA950 | 29.9 | 70.0 |

TABLE 3: Surface energies (in mJ/m^2) based on the two-liquid geometric method.

| Material | γ^d | γ^p | γ | Polarity (%) |
|----------|------------|------------|----------|--------------|
| PC | 39.36 | 6.50 | 45.86 | 14.2 |
| V400P | 17.56 | 24.06 | 41.62 | 57.8 |
| VA950 | 38.42 | 7.79 | 46.21 | 16.9 |
| CNT | 18.4 | 26.9 | 45.3 | 59.4 |

the contact angle values measured with di-iodomethane and water, which were used to calculate the surface energy values reported in Table 3 using γ_{LV}^d and γ_{LV}^p of the reference liquids provided by Kaelble [36]. Although there was some disagreement in literature for the contact angle data for PC [37–39], and VA950 [40, 41], those values still cover our experimental values. The surface energy of V400P has not yet been reported by others and the values for CNT were taken from [42]. The polarity of the materials was found in the following order: CNT > V400P > VA950 > PC. Since the carbonaceous materials tend to localize in more polar polymers [43], we anticipated that CNT would migrate towards the LCP phase. The interfacial energy of PC/VA950 was found to be much lower than that of PC/V400P (see Table 4) suggesting that the former should be a more compatible blend than the latter and, therefore, should be more conducive to fibrillation by LCP. The spreading coefficients of PC/V400P/CNT and PC/VA950/CNT were found to be 0.92 and 1.45 mJ/m^2 , respectively, after considering CNT as component 1, PC as component 2, and LCP as component 3, and after substituting the interfacial energy values in Harkins equation. The positive value of λ_{31} indicated that carbon nanotubes would be encapsulated by the LCP domains. It should be noted that the discussion in this paragraph was based on the values of surface tension data obtained at room temperature. In this context, it is recognized that the changes in surface tension of most polymers with respect to temperature were comparable, for example, 0.06–0.08 $\text{dyne} \cdot \text{cm} \text{ deg} \text{ K}^{-1}$ [34, 44, 45].

4.3. Morphology. SEM images of LCP residue extracted from PC/V400P and PC/VA950 blends are presented in Figure 3. The V400P phase in injection molded specimens remained in the form of droplets with the number-average diameter of 0.61 μm and a weight average diameter of 0.67 μm (Figure 3(a)) as a result of lower viscosity of PC. The average diameter was computed from the diameter of at least 100 droplets measured from the SEM images.

The as-compounded PC/VA950 blends taken from the minicomponent also show spherical VA950 domains with

number-average diameter of 0.49 μm and a weight-average diameter of 0.60 μm (Figure 3(b)). The VA950 domains in both fibrillar and spherical forms were found in injection molded specimen as in Figure 3(c). This can be attributed to lower pressure generated in the mini-injection molder and low rate of shear in mold filling, typically around 1.0 s^{-1} . One may expect more elongated fibrils in a high speed injection molding process, where the shear rate greater than 10 s^{-1} is typically encountered. First, higher rate of deformation and second, lowering of the viscosity ratio at higher shear rate may cause more extensive fibrillation. Subdued fibrillation and underdeveloped fibrillar structures of LCP domains may also have resulted from the feeding sequence. For example, prior mixing of CNT with LCP increased the viscosity of the LCP phase and hence increased the viscosity ratio of LCP/PC blends. In this case, only spherical domains were obtained as seen in Figure 4. Similar observations were made by Mukherjee et al. [27] in the presence of carboxylated CNTs. The surface of the droplets became rough as a result of the presence of LCP-coated CNT of $\sim 50 \text{ nm}$ diameter, although the diameter of as received nanotube was reported to be 13 nm. The mixing sequence was found to influence both the size and the shape of the LCP phase morphology. For example, larger and irregular dispersed VA950 domains were found when CNT was first mixed with VA950 (Figure 4(c)) compared to those of the reversed mixing sequence (Figure 4(b)). In the reversed mixing sequence, CNT increased the viscosity of the PC-phase and accordingly produced much lower viscosity ratio of LCP to PC than in mixtures without CNT.

Figure 5 shows the TEM micrographs of the PC/CNT and PC/LCP/CNT composites. All these samples contained 5 wt% of CNT. The PC/CNT composite shows good CNT dispersion (Figure 5(a)) whereas PC/LCP/CNT composites (Figures 5(b) and 5(c)) clearly reveal nonuniform CNT dispersion. The darker areas present in Figures 5(b) and 5(c) in the form of spheroids are actually the LCP domains. Clearly, the CNTs mainly resided inside the LCP droplets especially in composites of V400P LCP, in agreement with the SEM images seen in Figure 4. Some differences are noticeable in CNT dispersion between the composites PC/VA950/5 wt% CNT and PC/V400P/5 wt% CNT. For example, the TEM image in Figure 5(c) shows that CNT particles were present in both PC-phase and inside LCP domains when VA950 was used, while as per Figure 5(b), CNTs were mostly contained in V400P LCP domains. The interfacial energy data presented in Table 4 shows that CNT had very close affinity for PC and VA950 LCP, with interfacial energy of respectively 10.9 and 9.4 mJ/m^2 . On the other hand, CNTs showed more affinity to V400P LCP with interfacial energy of 0.09 mJ/m^2 . From the melt viscosity point of view, the filler tends to reside in the less viscous phase. This is in accordance with the localization of CNTs in the VA950 domains. On the other hand, the presence of V400P, having higher viscosity than PC, would result in the suppressed migration of the nanotubes into V400 phase and thus competing with the thermodynamic driving force. According to Persson and Bertilsson, viscosity effects are weak and dominate only when the difference of interactions between the filler/polymer1 and

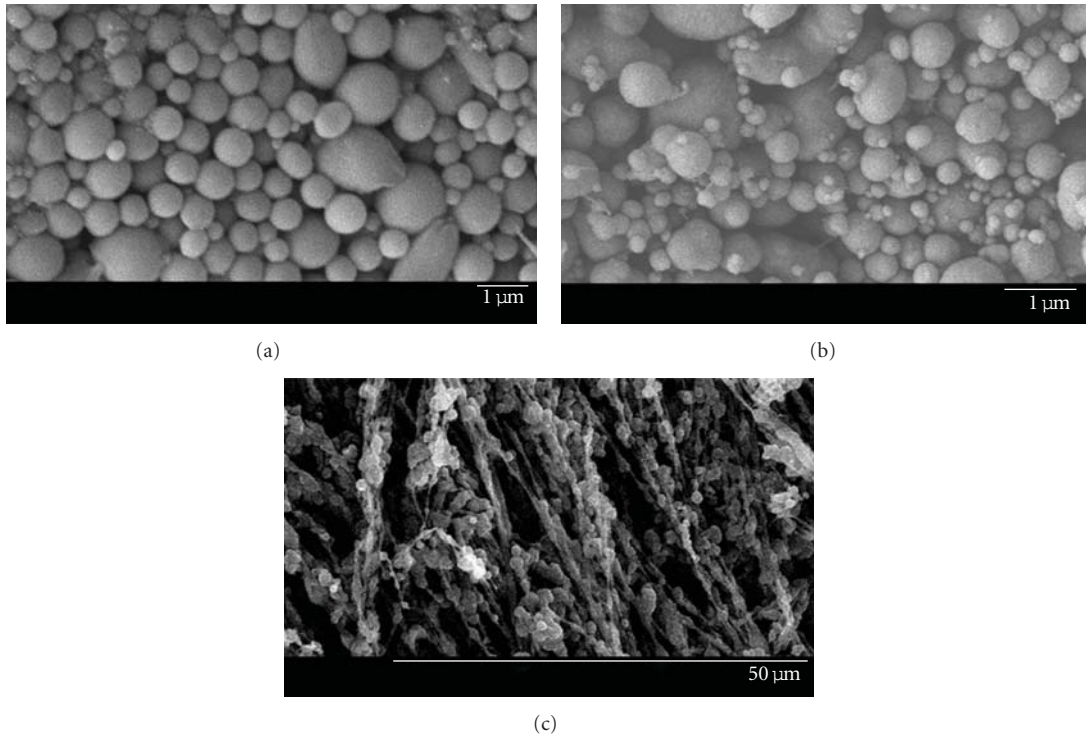


FIGURE 3: SEM micrographs of the LCP residues of PC/V400P (a) injection-molded specimen, (b) as-compounded PC/VA950, and (c) PC/VA950 injection-molded specimen.

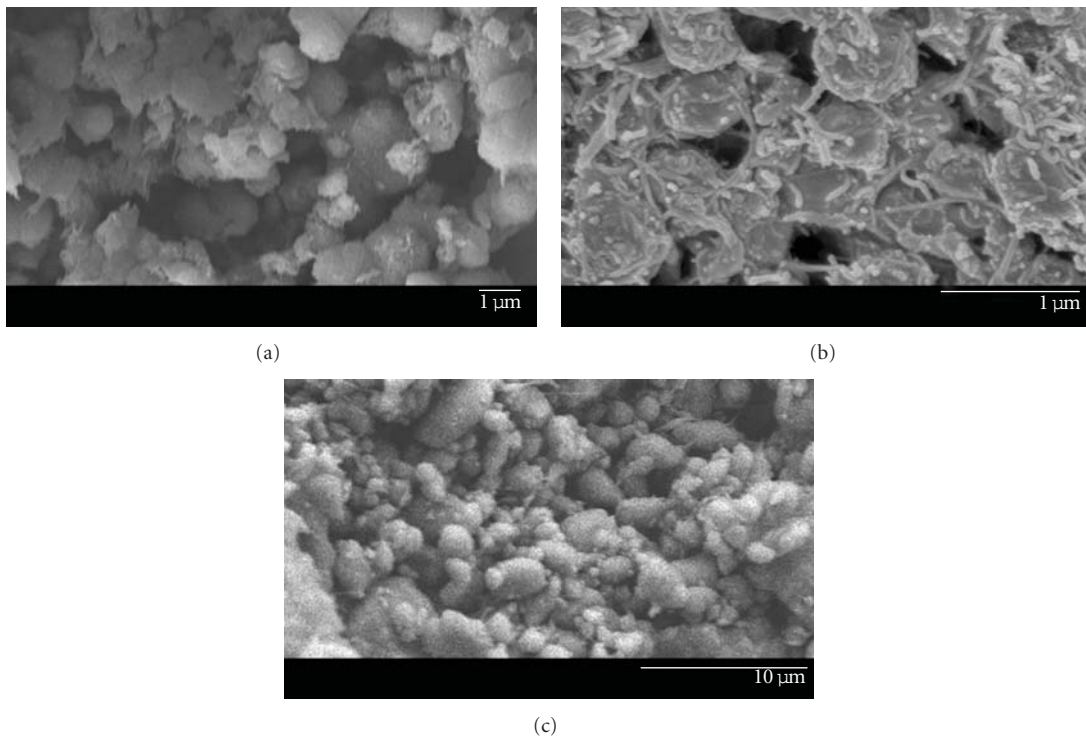


FIGURE 4: SEM micrographs of the LCP residues of injection-molded specimen of (a) PC/V400P/5 wt% CNT, (b) PC/VA950/5 wt% CNT, (c) PC/VA950/5 wt% CNT with reversed feeding sequence.

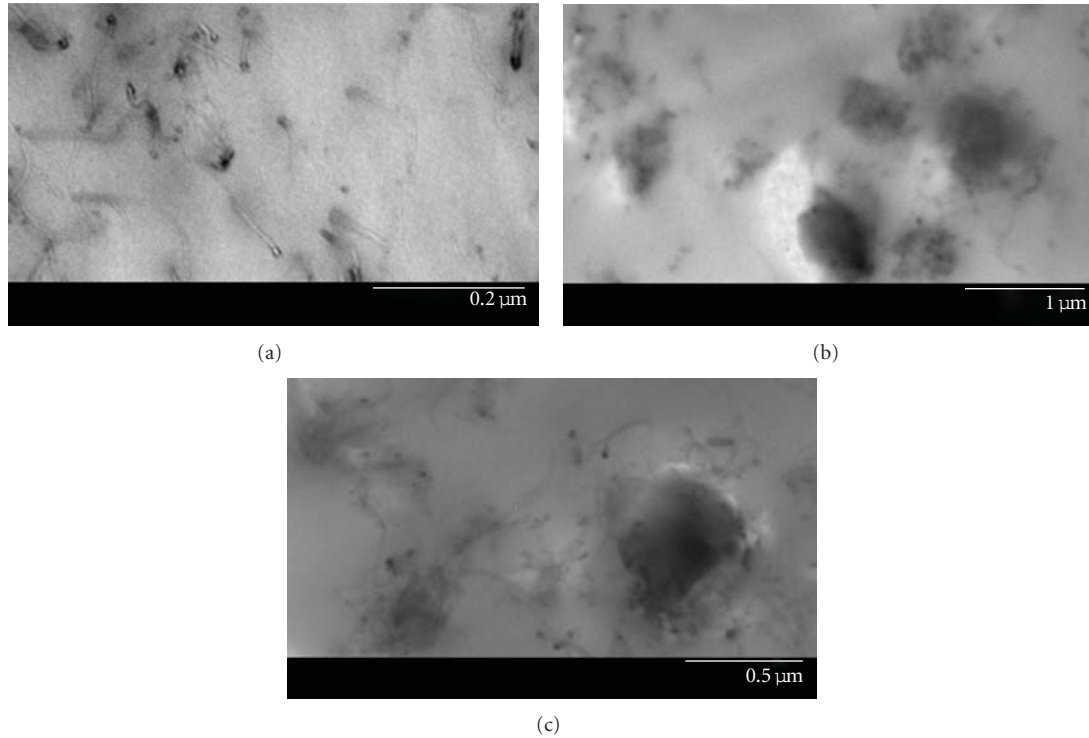


FIGURE 5: TEM micrographs of the thin sections of composites with 5 wt% CNT based on the (a) neat PC, (b) PC/V400P, and (c) PC/VA950.

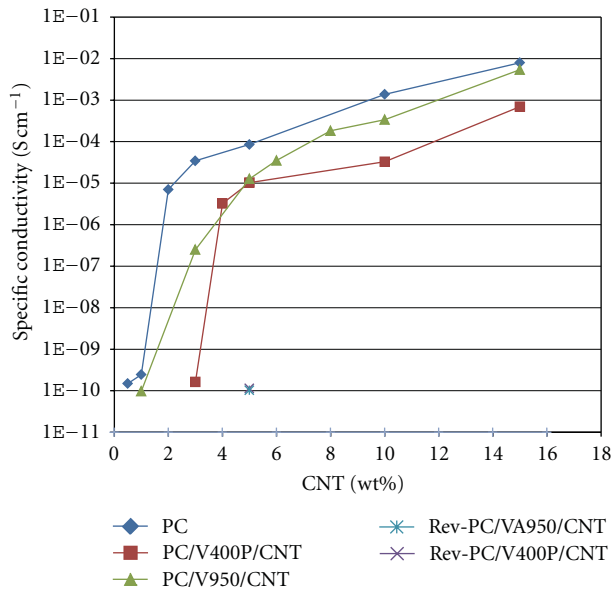


FIGURE 6: The specific conductivity of composites as function of CNT weight percent.

filler/polymer 2 is small [24, 46]. Since such difference in the PC/V400P/CNT system is quite large, it is not surprising that the thermodynamic factor prevailed on the viscosity factor, that is, the nanotubes selectively localized in V400P domains.

TABLE 4: Interfacial energies calculated from the geometric-mean equation and the harmonic-mean equation.

| Material | Interfacial energy (mJ/m ²) | |
|-----------|---|------------------------|
| | Geometric-mean equation | Harmonic-mean equation |
| PC/CNT | 10.9 | 20.0 |
| V400P/CNT | 0.09 | 0.18 |
| VA950/CNT | 9.4 | 17.6 |
| PC/V400P | 9.9 | 18.4 |
| PC/VA950 | 0.06 | 0.13 |

4.4. Electrical Conductivity. Figure 6 provides the specific electrical conductivity of five compounds as function of CNT content. The electrical conductivity at 5 wt% CNT can be expressed in the following order with the numbers in parentheses representing electrical percolation threshold: PC/CNT (1 wt%) > PC/VA950P/CNT (1 wt%) > PC/V400P/CNT (3 wt%). In this case, the percolation threshold was taken as the starting point of sharp rise of electrical conductivity. In light of the SEM and TEM images presented in Figures 4 and 5, it can be inferred that the nanotube conductive pathways were destroyed due to subdued fibrillation in the presence of either type of the LCP. The composites of LCP and CNT were found to be insulators even when the CNT content was as high as 10 wt%. Compounds of V400P and VA950 with up to 15 wt% CNT did not produce conductive composites. Therefore, in addition to restricted fibrillation, the increase in the electrical percolation threshold as well as

TABLE 5: Storage moduli, G' at 40°C, for PC, PC/LCP blends, and composites with 5 wt% CNT.

| Material | PC | PC/CNT | V400P | V400P/CNT | PC/V400P | PC/V400P/CNT | VA950 | VA950/CNT | PC/VA950 | PC/VA950/CNT |
|------------|------|--------|-------|-----------|----------|--------------|-------|-----------|----------|--------------|
| G' (GPa) | 1.58 | 1.73 | 4.30 | 4.83 | 2.25 | 1.57 | 3.05 | 4.28 | 1.74 | 1.83 |

the lowered electrical conductivity of the blends may result from encapsulation of the nanotubes with the insulating LCP as predicted by thermodynamic factors. Similar observation in blends of ABS/PA6/CNT was reported by Bose et al. [28].

Nevertheless, the composite of PC/VA950P/CNT showed percolation at 1 wt% CNT loading. This can be attributed to the presence of CNTs on the rough surfaces of VA950/CNT domains as seen in Figure 4(b) and corroborated by TEM image presented in Figure 5(c). A distinct shift in the percolation threshold to the higher CNT loading was observed in composites of V400P LCP. Although the melt viscosity of V400P was significantly higher than that of the PC matrix, the good affinity between this LCP and the nanotubes rendered the confinement of a large number of CNTs within the V400P phase. Consequently, only a small amount of CNT was available to span the matrix or to bridge across the LCP domains to form an electrical percolation network. For blends of PC/VA950/CNT, the spreading coefficient also predicts the migration of CNTs to the better-wetting VA950 phase, but not to the same extent as the blend with V400P. Subsequently, the formation of the electrical network by CNTs was more favored in the blend containing VA950 as compared to the one with V400P. Overall, the strong insulating properties of an LCP and the tendency of CNT to localize in the LCP-phase lowered the values of electrical conductivity when incorporated into the PC/CNT compounds. The affinity of CNT with both LCPs was demonstrated very clearly by the electrical conductivity values of the REV-PC/LCP/CNT composites. Here, CNT was first mixed with the LCP to obtain composite specimens REV-PC/V400P/CNT, and REV-PC/V950/CNT. During the second mixing step with PC, most of CNT remained in the LCP phase indicating that filler migration to the PC matrix was not favored. Consequently, these composites did not show electrical conductivity even at a loading of 5 wt% CNT. These results comply with the SEM image shown in Figure 4(c).

4.5. DMA Results. Table 5 shows the values of storage modulus at 40°C of three groups of sample—the neat polymers (PC, V400P, VA950), the blends of PC with 20 wt% LCP (PC/V400P, PC/VA950) and the composites of either PC or LCP with 5 wt% CNT (PC/CNT, V400P/CNT, VA950/CNT) or both PC/LCP with 5 wt% CNT (PC/V400P/CNT, PC/VA950/CNT). The storage moduli at less than 110°C of compounds containing V400P showed the following order: V400P/CNT > V400P > PC/V400P > PC/CNT > PC, PC/V400P/CNT. The most surprising result is the lower value of storage modulus of PC/V400P/CNT composite in comparison with PC/V400P blend and V400P/CNT composite. It was expected that the addition of CNT to PC/V400P would increase the modulus further in view of the fact that CNT remained primarily in V400P domains

and that V400P/CNT composite showed higher modulus than V400P (Table 5). The only possible explanation of this reduction of storage modulus of PC/V400P/CNT composite may be attributed to potential degradation of molecular weight of PC due to longer exposure (10 minutes) to compounding temperature compared to 5 minutes in other materials. However, reduction of PC molecular weight was not verified using chromatographic method. For VA950-containing compounds, the storage moduli at low temperature show the following trend: VA950/CNT > VA950 > PC/VA950/CNT ~ PC/VA950 ~ PC/CNT > PC. Once again, the storage modulus of PC/VA950/CNT composite remained in the neighborhood of PC/VA950 and PC/CNT, possibly due to molecular weight reduction of the PC phase, the latter attributed to longer exposure of PC to high compounding temperature.

5. Conclusions

Two PC/LCPs blends were designed by adjusting the melt viscosity ratio and the shear rate used in processing, such as injection molding to interpret the trends in mechanical properties and electrical conductivity in terms of CNT localization in LCP domains, PC phase, or at the interfaces. The PC/VA950 blend showed fibrillar structures and PC/V400P blend showed spherical LCP domains. Attempt was made to distribute the CNT in both PC/LCP blends and to determine the percolation threshold of CNT for electrical conductivity, although the positive values of the spreading coefficient parameter for CNT particles promoted preferential localization of CNT inside the LCP domains. PC showed surface energy and polarity comparable to VA950 but different from V400P, due to which double percolation was found to occur only for PC/VA950. Accordingly, PC/CNT and PC/VA950/CNT composites showed the same electrical percolation threshold (1 wt%) while PC/V400P/CNT needed 3 wt% CNT to show electrical percolation. Prior addition of CNT to LCP increased the viscosity of LCP phase further, which increased the viscosity ratio to greater than unity and hindered LCP fibril formation.

Acknowledgments

Financial support was provided in part by the Thailand Research Fund through the Royal Golden Jubilee Ph.D. Program and National Center of Excellence for Petroleum, Petrochemicals and Advanced Materials.

References

- [1] P. Pisitsak and R. Magaraphan, “Rheological, morphological, thermal, and mechanical properties of blends of vectra A950

- and poly(trimethylene terephthalate): a study on a high-viscosity-ratio system," *Polymer Testing*, vol. 28, no. 2, pp. 116–127, 2009.
- [2] L. P. Tan, C. Y. Yue, K. C. Tam, Y. C. Lam, and X. Hu, "Effects of shear rate, viscosity ratio and liquid crystalline polymer content on morphological and mechanical properties of polycarbonate and LCP blends," *Polymer International*, vol. 51, no. 5, pp. 398–405, 2002.
- [3] H. Wang, K. W. Lee, T. S. Chung, and M. Jaffe, "Rheology, morphology and properties of LCP/nylon 66 composite fibers," *Polymer Composites*, vol. 21, no. 1, pp. 114–123, 2000.
- [4] S. Saengsuwan, S. Bualek-Limcharoen, G. R. Mitchell, and R. H. Olley, "Thermotropic liquid crystalline polymer (Rodrun LC5000)/polypropylene in situ composite films: rheology, morphology, molecular orientation and tensile properties," *Polymer*, vol. 44, no. 11, pp. 3407–3415, 2003.
- [5] R. Viswanathan and I. A. Isayev, "Blends of a PPO-PS alloy with a liquid crystalline polymer," *Journal of Applied Polymer Science*, vol. 55, no. 7, pp. 1117–1129, 1995.
- [6] W. Bu and I. A. Isayev, "Prepregs and laminates of polyetherimide-reinforced by a thermotropic," *Journal of Applied Polymer Science*, vol. 56, no. 2, pp. 329–340, 1997.
- [7] I. Isayev and S. Swaminathan, "Wholly aromatic polyester fiber-reinforced polyetherimide composite and process for preparing same," European Patent EP 0 291 323, A2, 1994.
- [8] R. Tchoudakov, M. Nakis, and A. Seigmann, "Electrical conductivity of polymer blends containing liquid crystalline polymer and carbon black," *Polymer Engineering & Science*, vol. 44, no. 3, pp. 528–540, 2004.
- [9] Y. W. Wong, K. L. Lo, and F. G. Shine, "Electrical and thermal properties of composite of liquid crystalline polymer filled with carbon black," *Journal of Applied Polymer Science*, vol. 82, no. 6, pp. 1549–1555, 2001.
- [10] J. Bao, C. Xu, W. Cai, and X. T. Bi, "Electrically conductive composite of polypyrrole and liquid crystalline copoly(esteramide)s," *Journal of Applied Polymer Science*, vol. 52, no. 10, pp. 1489–1497, 1994.
- [11] M. Sumita, K. Sakata, Y. Hayakawa, S. Asai, K. Miyasaka, and M. Tanemura, "Double percolation effect on the electrical conductivity of conductive particles filled polymer blends," *Colloid & Polymer Science*, vol. 270, no. 2, pp. 134–139, 1992.
- [12] J. C. Huang, "Carbon black filled conducting polymers and polymer blends," *Advances in Polymer Technology*, vol. 21, no. 4, pp. 299–313, 2002.
- [13] I. Mironi-Harpaz and M. Narkis, "Thermo-electric behavior (PTC) of carbon black-containing PVDF/UHMWPE and PVDF/XL-UHMWPE blends," *Polymer Engineering and Science*, vol. 41, no. 2, pp. 205–221, 2001.
- [14] R. Tchoudakov, O. Breuer, M. Narkis, and A. Siegmann, "Conductivity/Morphology Relationships in immiscible polymer blends: HIPS/SIS/Carbon black" in *Conductive Polymers and Plastics in Industrial Applications*, L. Rupprecht, Ed., p. 51, William Andrew Publishing/Plastics Design Library, New York, NY, USA, 1999.
- [15] D. P. Dharaia, S. C. Jana, and S. F. Lyuksyutov, "Production of electrically conductive networks in immiscible polymer blends by chaotic mixing," *Polymer Engineering and Science*, vol. 46, no. 1, pp. 19–28, 2006.
- [16] C. Zhang, X. S. Yi, H. Yui, S. Asai, and M. Sumita, "Morphology and electrical properties of short carbon fiber-filled polymer blends: high-density polyethylene/ poly (methyl methacrylate)," *Journal of Applied Polymer Science*, vol. 69, no. 9, pp. 1813–1819, 1998.
- [17] C. Zhang, P. Wang, C. A. Ma, G. Wu, and M. Sumita, "Temperature and time dependence of conductive network formation: dynamic percolation and percolation time," *Polymer*, vol. 47, no. 1, pp. 466–473, 2006.
- [18] P. Pötschke, A. R. Bhattacharyya, and A. Janke, "Carbon nanotube-filled polycarbonate composites produced by melt mixing and their use in blends with polyethylene," *Carbon*, vol. 42, pp. 965–969, 2004.
- [19] P. Pötschke, A. R. Bhattacharyya, and A. Janke, "Morphology and electrical resistivity of melt mixed blends of polyethylene and carbon nanotube filled polycarbonate," *Polymer*, vol. 44, no. 26, pp. 8061–8069, 2003.
- [20] P. Pötschke, S. Pegel, M. Claes, and D. Bonduel, "A novel strategy to incorporate carbon nanotubes into thermoplastic matrices," *Macromolecular Rapid Communications*, vol. 29, no. 3, pp. 244–251, 2008.
- [21] S. Bose and A. R. Bhattacharyya, "Rheology, electrical conductivity and the phase behaviour of cocontinuous PA6/ABS blends with MWNT: correlating the aspect ratio of MWNT with the percolation threshold," *Journal of Polymer Science B*, vol. 46, pp. 1619–1631, 2008.
- [22] V. Mittal, Ed., *Specific Interactions Induced Controlled Dispersion of Multiwall Carbon Nanotubes in Co-Continuous Polymer Blends*, in *Polymer Nanotube Nanocomposites: Synthesis, Properties, and Applications, Chapter 13*, John Wiley & Sons, Hoboken, NJ, US, 2010.
- [23] S. Y. Hobbs, M. E. J. Dekkers, and V. H. Watkins, "Effect of interfacial forces on polymer blend morphologies," *Polymer*, vol. 29, no. 9, pp. 1598–1602, 1988.
- [24] F. Fenouillot, P. Cassagnau, and J. C. Majesté, "Uneven distribution of nanoparticles in immiscible fluids: morphology development in polymer blends," *Polymer*, vol. 50, no. 6, pp. 1333–1350, 2009.
- [25] H. H. Chen, J. P. deSouza, D. G. Baird, K. T. The, and J. Morton, "Processing of in situ composites based on thermoplastic matrices and liquid crystalline polymers," in *Proceedings of the 9th International Conference on Composite Materials (ICCM '93)*, vol. 5, p. 467, July 1993.
- [26] A. I. Isayev and S. Swaminathan, "Wholly aromatic polyester fiber-reinforced polyetherimide composite and process for preparing same," U.S. Patent 4,835,047, 1989.
- [27] M. Mukherjee, T. Das, R. Rajasekar, S. Bose, S. Kumar, and C. K. Das, "Improvement of the properties of PC/LCP blends in the presence of carbon nanotubes," *Composites A*, vol. 40, no. 8, pp. 1291–1298, 2009.
- [28] S. Bose, A. R. Bhattacharyya, A. R. Kulkarni, and P. Pötschke, "Electrical, rheological and morphological studies in co-continuous blends of polyamide 6 and acrylonitrile-butadiene-styrene with multiwall carbon nanotubes prepared by melt blending," *Composites Science and Technology*, vol. 69, no. 3–4, pp. 365–372, 2009.
- [29] M. Mukherjee, S. Bose, G. C. Nayak, and C. K. Das, "A study on the properties of PC/LCP/MWCNT with and without compatibilizers," *Journal of Polymer Research*, vol. 17, no. 2, pp. 265–272, 2010.
- [30] G. Tovar, P. J. Carreau, and H. P. Schreiber, "Transesterification, morphology and some mechanical properties of thermotropic liquid crystal polymers/polycarbonate blends," *Colloids and Surfaces A*, vol. 161, no. 1, pp. 213–223, 2000.
- [31] P. J. Flory, "Statistical thermodynamics of mixtures of rodlike particles. 5. Mixtures with random coils," *Macromolecules*, vol. 11, no. 6, pp. 1138–1141, 1978.

- [32] D. K. Owens and R. C. Wednt, "Estimation of the surface free energy of polymers," *Journal of Applied Polymer Science*, vol. 13, no. 8, pp. 1741–1747, 1969.
- [33] D. H. Kaelble, "A reinterpretation of organic liquid- polytetrafluoroethylene surface interactions," *Journal of Adhesion*, vol. 2, pp. 50–60, 1970.
- [34] S. Wu, *Polymer Interface and Adhesion*, Marcel Dekker, New York, NY, USA, 1982.
- [35] W. D. Harkins, *The Physical Chemistry of Surface Films*, Reinhold, New York, Ny, USA, 1952.
- [36] D. H. Kaelble, *Physical Chemistry of Adhesion*, Wiley Interscience, New York, NY, USA, 1970.
- [37] J. L. Dewez, E. Humbeek, E. Everaet, A. Doren, and P. G. Rouxhet, *Polymer-Solid Interfaces*, Institute of Physics Publishing, Bristol, UK, 1991.
- [38] S. Jonsson, *Presented at Aspects of Adhesion*, Radcure, Middlesex, UK, 1992.
- [39] J. S. Cho, "Metallized Plastics Surface modification of polymers by ion-assisted reactions: an overview," in *Adhesion Aspects of Thin Films*, K. L. Mittal, Ed., vol. 2, p. 105, VSP, Utrecht, The Netherlands, 2005.
- [40] K. X. Ma, T. S. Chung, and R. J. Good, "Surface energy of thermotropic liquid crystalline polyesters and polyesteramide," *Journal of Polymer Science B*, vol. 36, no. 13, pp. 2327–2337, 1998.
- [41] T. S. Chung, K. X. Ma, and M. Jaffe, "Experimental and theoretical estimations of surface tensions for commercial liquid crystalline polymers, Vectra A-950, B-950 and Xydar SRT-900," *Macromolecular Chemistry and Physics*, vol. 199, no. 6, pp. 1013–1017, 1998.
- [42] S. Nuriel, L. Liu, A. H. Barber, and H. D. Wagner, "Direct measurement of multiwall nanotube surface tension," *Chemical Physics Letters*, vol. 404, no. 4–6, pp. 263–266, 2005.
- [43] C. F. Schoff, "Painting problem," in *Coatings of Polymers and Plastics*, R. A. Ryntz and P. V. Yaneff, Eds., p. 227, Marcel Dekker, New York, NY, USA, 2003.
- [44] S. Wu, "Calculation of interfacial tension in polymer systems," *Journal of Polymer Science C*, vol. 34, no. 1, pp. 43–19, 1974.
- [45] G. L. Gaines, "Surface and interfacial tension of polymer liquids-a review," *Polymer Engineering & Science*, vol. 12, no. 1, pp. 1–11, 1997.
- [46] A. L. Persson and H. Bertilsson, "Viscosity difference as distributing factor in selective absorption of aluminium borate whiskers in immiscible polymer blends," *Polymer*, vol. 39, no. 23, pp. 5633–5642, 1998.

Research Article

Direct-Write Drawing of Carbon Nanotube/Polymer Composite Microfibers

Scott M. Berry,^{1,2,3} Santosh Pabba,² Robert W. Cohn,² and Robert S. Keynton^{1,2,4}

¹ Department of Mechanical Engineering, University of Louisville, 200 Sacket Hall, Louisville, KY 40292, USA

² The Electrooptics Research Institute and Nanotechnology Center, University of Louisville, Louisville, KY 40292, USA

³ Department of Biomedical Engineering, University of Wisconsin-Madison, 6036 WIMR, 1111 Highland Avenue, Madison, WI 53705, USA

⁴ Department of Bioengineering, University of Louisville, 419 Lutz Hall, Louisville, KY 40292, USA

Correspondence should be addressed to Scott M. Berry, scott.michael.berry@gmail.com

Received 30 April 2012; Accepted 23 July 2012

Academic Editor: Sadhan C. Jana

Copyright © 2012 Scott M. Berry et al. This is an open access article distributed under the Creative Commons Attribution License, which permits unrestricted use, distribution, and reproduction in any medium, provided the original work is properly cited.

Carbon-nanotube- (CNT-) doped polymer solutions were drawn into arrays of microfibers using a novel direct-write process. This process utilizes a micromanipulator-controlled syringe loaded with solvated polymer mixed with CNTs to “write” networks of composite fibers with precisely positioned endpoints. The diameters of these composite fibers are correlated to the degree of capillary thinning that occurs prior to the solidification of the directly written CNT-doped solution filament. The fibers had diameters ranging from 7 μm to over 100 μm and possessed conductivities as high as 0.1 Sm^{-1} . Fiber diameter was found to increase with increasing polymer concentration and decreasing fiber length and can be controlled through modulation of these parameters. The presence of CNTs was found not to significantly affect fiber diameter, despite the CNTs significant effect on viscosity, which was previously reported to influence diameter. This discrepancy is likely related to the non-Newtonian effects of CNT/polymer solutions, including an apparent shear thinning at increasing axial strain rates.

1. Introduction

CNT-doped polymers have emerged as popular materials in the production of microelectronic components and devices. These composites possess distinct attributes characteristic of both CNTs (high strength and electrical conductivity) and polymers (light weight, flexible, and customizable), making them ideal selections for the production of a variety of devices including chemical or mechanical sensors [1], flexible electromagnetic interference (EMI) shielding [2], and “smart” textiles [3]. One critical quality essential to the functionality of all microelectronic applications is the existence of sufficient conductivity throughout the composite material. Several groups have reported that conductivity of a CNT/polymer composite will increase with increasing CNT concentration in a nonlinear or nonisotropic manner [4–7]. The complex relationship between CNT concentration and conductivity is related to the principle of “percolation,” which predicts a sharp rise in conductivity when CNT

concentration surpasses a threshold value where a *continuous* network of CNTs exists within the surrounding polymer matrix. Furthermore, processing of composites into fiber geometries has been reported to align the CNTs along the fiber axis [5, 6]. However, the effect of this alignment on conductivity seems unclear, as indicated by conflicting reports [6, 7] in the literature.

Micro/nanofibrous architectures have proven effective in a variety of microelectronic applications due to intrinsic advantages associated with fibrous structures including improved flexibility, maximum surface area, and increased strength. Melt spinning has emerged as a popular technique to process these bulk composites into fibers, with reported generation of fibers composed of CNT-doped polyamide 12 [8], polyamide 6 [9], PMMA [10], and polypropylene [11]. Additionally, CNT/polyvinyl alcohol (PVAc) composite fibers have been produced via wet spinning [3, 12] and CNT-doped poly(lactide) (PLA) [13] and polystyrene [14] via electrospinning. In recent work by Pabba et al. [5, 15],

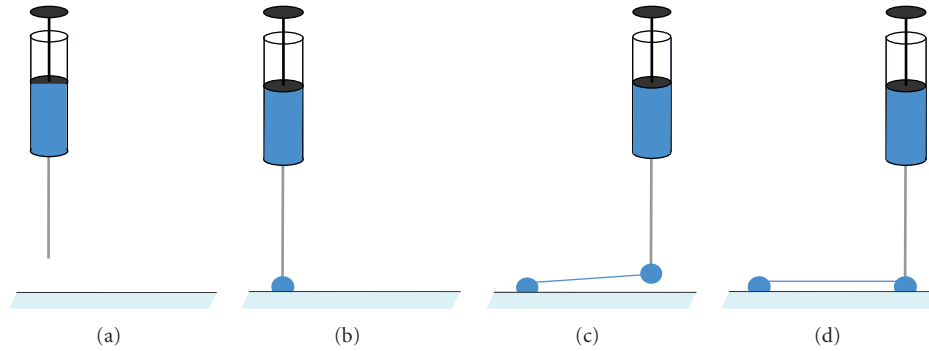


FIGURE 1: Direct-write drawing of CNT-doped polymer fibers. (a) Load syringe with CNT-doped solvated polymer. (b) Pressurize syringe to expel solution into contact with substrate. (c) Translate syringe to desired endpoint. (d) Pressurize syringe to establish second contact point.

a technique was reported in which viscous CNT/PMMA solutions were manually brushed across microfabricated pillar arrays to form networks of micro- and nanoscale solution filaments, which solidified to form suspended fibers. While each of these fiber fabrication strategies enables production of large quantities of fibers, none facilitates the construction of individual fibers that can be precisely positioned on any three-dimensional substrate. This limitation imposes constraints on the design of next-generation microelectronics, particularly those with 3D features.

In this investigation, CNT-doped polymer fibers that were precisely positioned in 3D were produced using a previously described direct-write technique [16, 17]. The direct-write system consists of a micromanipulator-controlled syringe that was programmed to pattern arrays of fibers on a substrate. The direct-write syringe was first loaded with a test solution and positioned $500\ \mu\text{m}$ above a glass substrate (Figure 1(a)). The syringe was then pressurized to expel a pendant droplet of solution, which contacts and adheres to the substrate (Figure 1(b)). Next, the syringe was lifted 1 mm and translated laterally to extend this droplet into a filament of solution (Figure 1(c)). The fiber endpoint was established by lowering the syringe to its initial height after the translation, thereby allowing the pendant drop to make an additional contact point (Figure 1(d)). Meanwhile, during extension, the solution filament underwent surface tension-driven capillary thinning, while solvent evaporation promoted the solidification of the composite fiber. By repeating this process, arrays of composite fibers were created in series in a “connect-the-dots” manner.

In our previous work, we demonstrated that the diameters of the fibers with the direct-write system from polymer solutions alone (i.e., no CNTs) were dependent on both solution properties and direct-write system parameters. Specifically, fiber diameter increased with increasing viscosity, increasing solvent evaporation rate, decreasing surface tension, decreasing fiber length, and decreasing fiber-drawing rate [16, 17]. Unfortunately, the applicability of these relationships is limited by the assumption that the polymer solution behaves in a “Newtonian-like” manner (i.e., that the capillary velocity of the solution, defined as the ratio of surface tension to viscosity, remains constant

over the course of direct-write processing). Although some polymer solutions were found to meet this criterion, this critical assumption represents a significant shortcoming for the previously described model. Therefore, the purpose of the current investigation is to extend the direct-write technique to CNT/polymer composites and determine how the non-Newtonian nature of these materials affects direct-write outcomes.

2. Materials and Methods

2.1. Solution Preparation. Solutions containing 1% CNTs were prepared by dissolving either 24% or 26% (by wt.) poly(methyl methacrylate) (PMMA) (Sigma-Aldrich, St. Louis, MO, MW = 996,000 g/mol) in a solution of chlorobenzene supplemented with multiwalled nanotubes (MWNTs) (Conc. = 10 mg/mL) that were functionalized to remain well-dispersed in chlorobenzene (Zyve NanoSolve, Richardson, TX). Once dried, the 24% and 26% solutions would produce solid PMMA with 4.0% or 3.7% CNTs, respectively. Control solutions containing no CNTs were prepared by dissolving 24 or 26% (by wt.) PMMA in pure chlorobenzene.

2.2. Solution Characterization. The effect of axial strain on extensional viscosity was determined for PMMA solutions with and without the addition of CNTs. A capillary breakup rheometer (CaBER) (Thermo Haake 1, Thermo Electron Corp.) was utilized to measure the midpoint diameters, $D_{\text{mid}}(t)$, of filaments of each of the test solutions as they experienced surface tension-driven thinning. These filaments were formed by stretching cylinders of each solution in a near-instantaneous manner ($t_{\text{stretch}} = 20\ \text{ms}$) from a length of 2 mm to a length of 8 mm. The midpoint diameters of the elongated filaments were continuously monitored for 10 seconds with a laser micrometer at a sampling rate of 3,000 Hz.

The midpoint diameter data collected by the CaBER was analyzed in order to determine the axial strain rate, $\dot{\epsilon}$, of

the solution filaments. Assuming uniaxial extension, the axial strain rate is correlated to midpoint diameter by [18]:

$$\dot{\epsilon} = \frac{-2}{D_{\text{mid}}(t)} \frac{dD_{\text{mid}}(t)}{dt}. \quad (1)$$

This strain rate was then employed to calculate the apparent extensional viscosity, η_{ext} , of the test solutions using [19]:

$$\eta_{\text{ext}} = \frac{(4 \cdot 0.7127 - 2)\sigma}{D_{\text{mid}}(t)\dot{\epsilon}}. \quad (2)$$

η_{ext} was plotted as a function of axial strain rate over the course of the CaBER experiments to determine the level of dependency of extensional viscosity on strain rate. The dependency of η_{ext} on $\dot{\epsilon}$ was quantified to determine if any extensional thinning (or thickening) of the test solutions was apparent, suggesting non-Newtonian behavior during extensional flow [19]. Surface tension was measured via the Wilhelmy technique [20], and solvent mass transfer coefficient was measured using thermogravimetric analysis (TGA), as previously described [16].

2.3. Direct-Write Fiber Fabrication. Fibers were drawn to three different lengths (4, 8, and 16 mm) from each of the test solutions at a rate of 20 mm/s, which was found to work well in previous studies [16, 21]. A total of 8 drawing attempts were made for each combination of solution and length. The syringe was pressurized to expel a constant flow of approximately 20 $\mu\text{L}/\text{min}$ through a 22 gauge needle (I.D. = 394 μm). After drawing, each array was coated with a thin layer ($t = 10$ to 20 nm) of gold/palladium alloy and the diameter of each fiber was measured in three locations (at the midpoint and 200 μm from each end) using a scanning electron microscope (SEM) (Zeiss Supra 35VP, Thornwood, NY). Process yield was determined by calculating the ratio of unbroken fibers to fiber drawing attempts.

2.4. Electrical Transport Measurement. The conductivity of the MWNT-doped fibers was measured to quantify the electrical transport along the fibers. The ends of each fiber were metalized with silver paint to minimize contact resistance, and the resistance of each fiber was analyzed with a highly sensitive parameter analyzer (Agilent 4156, Santa Clara, CA). Conductivity for each fiber was calculated by

$$G = \frac{4L}{R\pi(D_{\text{avg}})^2}, \quad (3)$$

where G is conductivity, L is the length of the fiber, R is the measured fiber resistance, and D_{avg} is the average fiber diameter [22].

2.5. Cross-Sectional Imaging. Cross-sections of fibers from each test solution were inspected with an SEM to determine the homogeneity of the fibers. Fibers were frozen in liquid nitrogen for 1 minute, cleaved with a razor blade, and coated with a thin layer ($t = 10$ to 20 nm) of gold-palladium prior to imaging. The images were then used to determine the level and distribution of CNT aggregation within the fibers.

3. Results and Discussion

3.1. Solution Characterization. Solutions containing PMMA and CNTs were observed to possess surface tensions that were slightly higher than pure chlorobenzene ($\sigma = 33.28 \text{ mN/m}$ at 20°C). The presence of CNTs in the solutions was found to have no significant effect on the surface tensions of the PMMA solutions (Table 1). The inclusion of CNTs in the test solutions was found to impede the evaporation of the chlorobenzene from the solutions as evidenced by the lower values in the mass transfer coefficients.

The CaBER was utilized to instantaneously extend volumes of each test solution into liquid bridges with initial aspect ratios (L/D) of approximately 2.7. The diameters of these liquid bridges, $D_{\text{mid}}(t)$, were monitored for 10 seconds as surface tension-driven thinning occurred (Figure 2(a)). This figure illustrates that solutions with no CNTs were observed to thin more rapidly than those with 1% CNTs and the 24% PMMA solution with no CNTs thinned faster than the corresponding 26% PMMA solution. Both solutions with 1% CNTs thinned at approximately the same rate, suggesting that the presence of CNTs is the dominating factor in the surface tension-driven thinning of these solutions. The measurement of $D_{\text{mid}}(t)$ was used with (1) and (2) and the data from Table 1 to calculate $\dot{\epsilon}$ and η_{ext} , which are plotted against each other in Figure 2(b). Unfortunately, the CaBER instrument was only able to apply a limited range of axial strain rates to the test solutions and this range was different for each solution (i.e., each of the curves in Figure 2(b) is for a small range of strain rate, making comparison between solutions more difficult). However, based on this limited data, it appears that the CNT composites experience shear thinning while the extensional viscosity of the PMMA-only solutions is relatively independent of shear rate.

3.2. Direct-Write Production of Fibers. The direct-write process was successfully employed to produce CNT-doped fibers with diameters ranging from 7 μm to over 100 μm (Figure 3). The fiber diameter data is given in Figure 4(a). ANOVA analysis of this data determined that fiber diameter increased with increasing PMMA concentration ($P < 0.001$) and decreasing length ($P < 0.001$). However, the presence of 1% CNTs did not significantly influence fiber diameter ($P = 0.2$) except for the 4 mm long fibers drawn from the 24% polymer solution ($P < 0.005$). Paired t -Test analysis confirmed that the fibers possessed significantly smaller diameters midway along their lengths relative to their ends ($P < 0.001$). Also, the ends of the fibers where drawing was begun were significantly smaller than the ends where drawing was completed ($P < 0.001$). The average coefficient of variation (diameter standard deviation/diameter average) for all fibers along the length of the fibers was 34%. The process yield for the direct-write process exceeded 85% under all test conditions (Figure 4(b)).

The characterization of test solution rheology suggests that the CNT-doped solutions experience strain thinning when exposed to axial strain, whereas nondoped solutions behave in a more Newtonian manner, even at higher strain rates (Figure 2(b)). A similar trend was observed

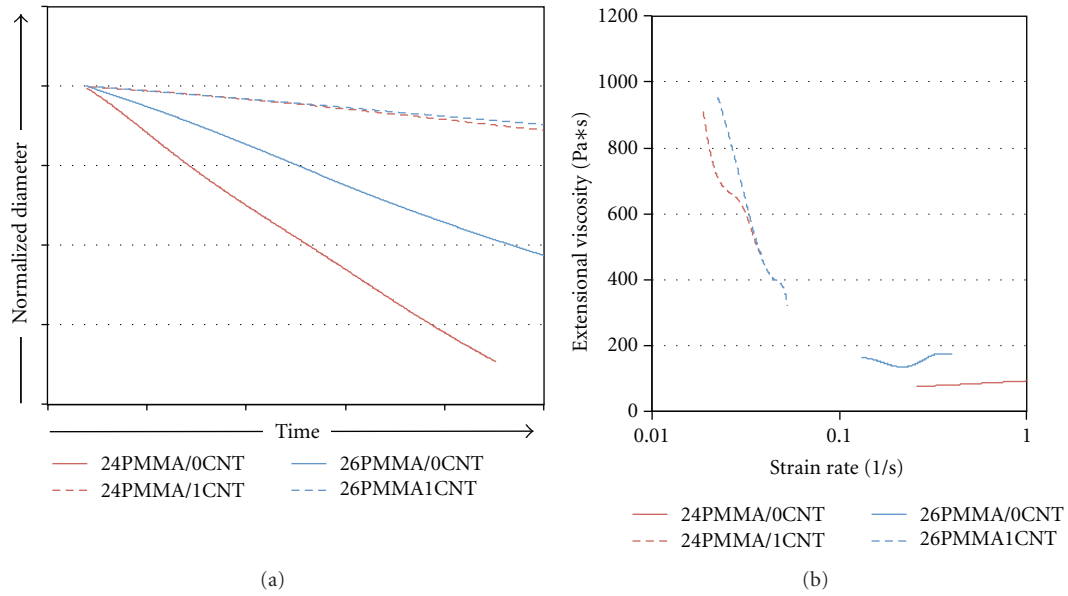


FIGURE 2: (a) CaBER data illustrating the surface tension-driven thinning of the test solutions as a function of time. (b) Extensional viscosity of test solutions as a function of axial strain rate experienced during capillary thinning.

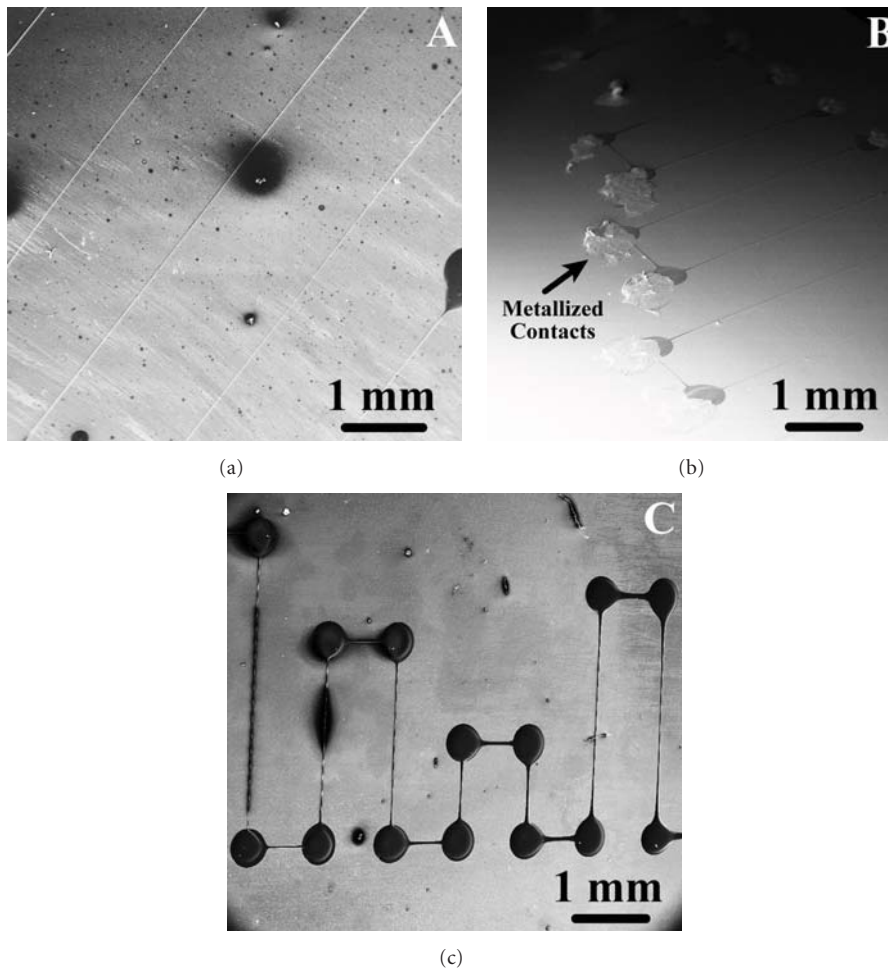


FIGURE 3: Fibers produced with the direct-write process. (a) Multiple parallel fibers. (b) Ends of fibers metallized with silver paste. (c) Test array of fibers with varying lengths. Fibers appear darker in (c) due to differences in SEM imaging contrast.

TABLE 1: Surface tensions and mass transfer coefficients of test solutions.

| PMMA solution concentration | CNT solution concentration | Surface tension (mN/m) | Mass transfer coefficient (m/s) |
|-----------------------------|----------------------------|------------------------|---------------------------------|
| 24% | 0% | 37.2 ± 7.3 | $1.06E - 07$ |
| 26% | 0% | 43.6 ± 7.2 | $1.06E - 07$ |
| 24% | 1% | 45.8 ± 5.2 | $5.82E - 08$ |
| 26% | 1% | 45.3 ± 1.5 | $5.82E - 08$ |

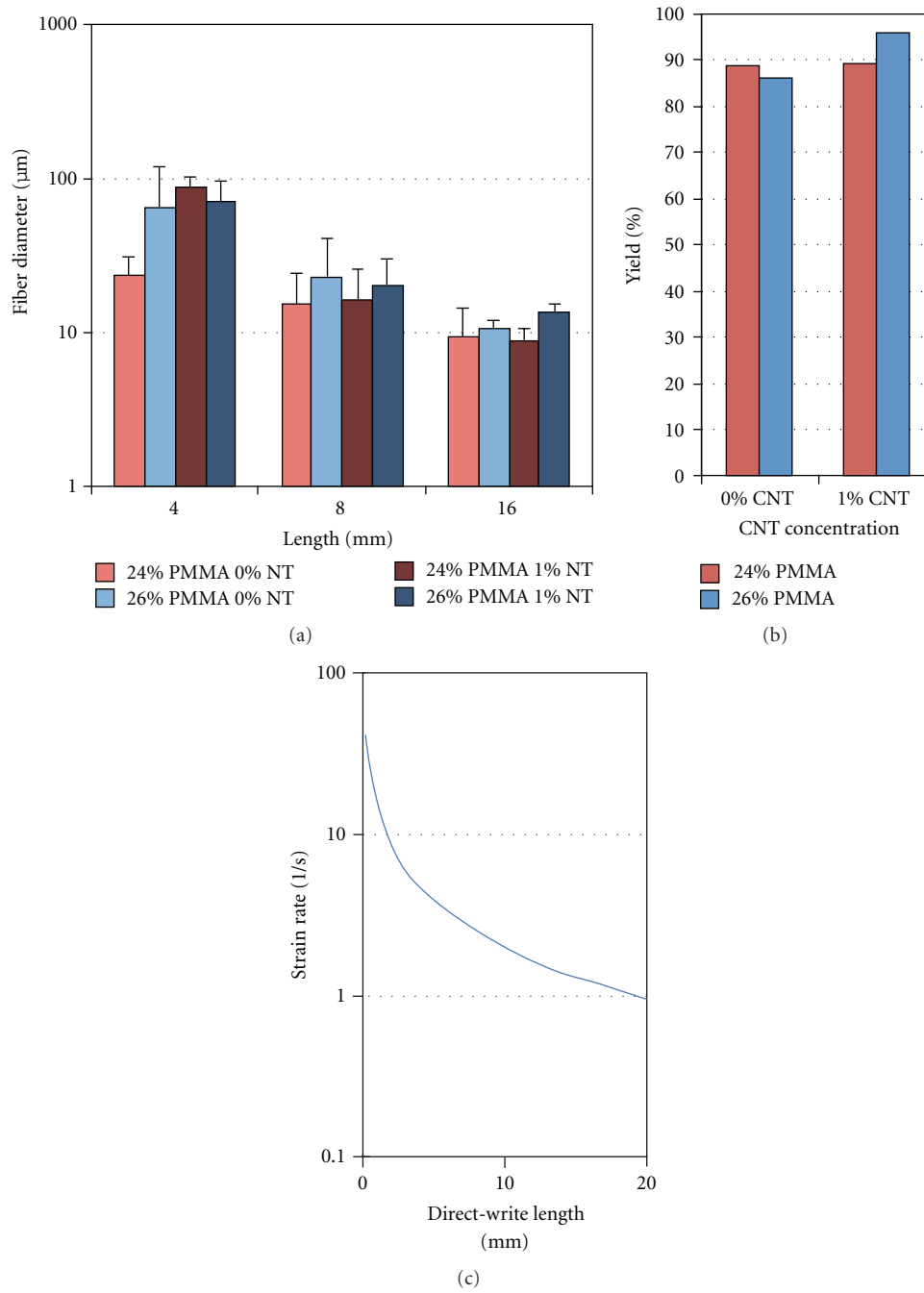


FIGURE 4: Fiber diameter as a function of fiber length, PMMA concentration, CNT concentration. Error bars denote standard deviation and $n = 8$. (b) Direct-write yield as a function of PMMA concentration and CNT concentration. (c) Axial strain imparted on the solution by the motion of the direct-write system as a function of drawing length, as predicted by (4).

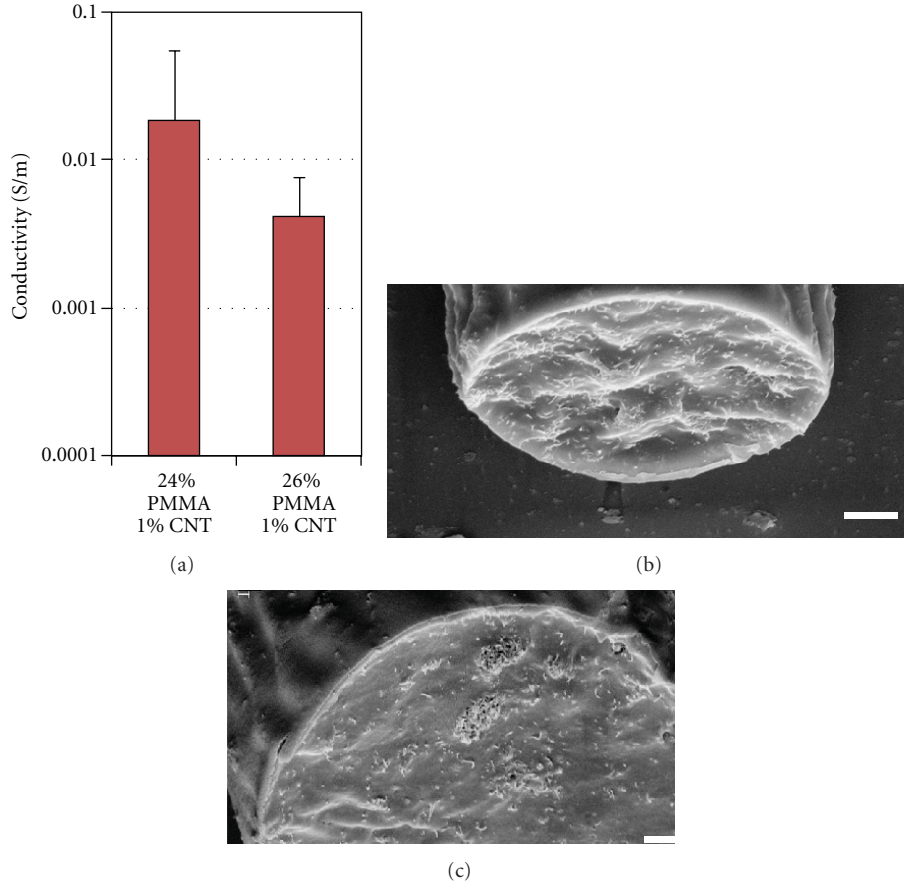


FIGURE 5: (a) Conductivity as a function of PMMA concentration. (b) Cross-sectional image of fiber drawn from 24% PMMA/1% CNT solution. (c) Cross-sectional image of fiber drawn from 26% PMMA/1% CNT solution. Scale bars in (b) and (c) are 1 μm .

by Rahatekar et al. who concluded that epoxy doped with CNTs will thin when exposed to increasing shearing strain rates until it asymptotically approaches the viscosity of pure epoxy [23]. Although the CaBER system was not capable of inducing high axial strain rates ($\dot{\epsilon} > 0.1$) on the CNT-doped solutions, the orientations of the curves in Figure 2(b) suggests that such an asymptotic relationship may exist (i.e., the extensional viscosity of the CNT-doped solutions could approach that of the pure PMMA solutions if axial strain rate was increased).

During direct-write drawing, the solution experiences axial strain due to surface tension-driven thinning in a manner similar to the CaBER experiments. However, the motion of the direct-write syringe, which imposed additional axial strain on the solution, augmented this strain. The magnitude of this strain generated by the motion of the direct-write syringe, ϵ_{DW} , is given by [24]:

$$\epsilon_{\text{DW}} = \ln\left(\frac{L(t)}{L_0}\right), \quad (4)$$

where $L(t)$ is the length of the direct-write fiber as it is drawn and L_0 is the initial length of the solution droplet on the direct-write syringe before drawing ($L_0 \approx 394 \mu\text{m}$).

Equation (4) is differentiated to obtain the axial strain rate imparted by the direct-write process:

$$\dot{\epsilon}_{\text{DW}} = \frac{1}{L(t)} \frac{dL(t)}{dt}, \quad (5)$$

where $dL(t)/dt$ is the drawing velocity of the direct-write system. Figure 4(c) illustrates the magnitude of the axial strain rate generated by the direct-write process for fibers drawn up to lengths of 16 mm at a test velocity of 20 mm/s. Comparison of these axial strain rates with those generated by the CaBER (Figure 2(b)), which expresses the magnitude of axial strain rate during surface tension-driven thinning only, suggest that the motion of the drawing process influences axial strain rate by an approximate order of magnitude more than the surface tension-driven thinning motion alone. Furthermore, the axial strain rates encountered during the direct-write process may be sufficiently large to thin the CNT-doped solutions into the asymptotic regime where η_{ext} approaches η_{ext} of the homopolymer system, providing a potential explanation as to why CNT concentration was shown not to influence fiber diameter, except in the case of the shortest fibers (i.e., lowest applied strain) with the lower polymer concentration (i.e., more thinning of the undoped solution).

3.3. Fiber Conductivity. It was observed that conductivity decreases with increasing PMMA concentration (Figure 5(a)), but it was not statistically significant ($P = 0.1$). Fiber length was found not to significantly affect conductivity, suggesting that lengthening fibers (from 4 mm to 16 mm) did not induce a major change in the CNT/polymer matrix architecture. Cross-sectional imaging of representative fibers drawn from each test solution illustrated the level of CNT dispersion within the fibers, as shown in Figures 5(b) and 5(c). In general, the magnitude of conductivity was similar to that previously reported for PMMA/CNT composite fibers [4].

4. Conclusions

Arrays of CNT-doped PMMA fibers were successfully produced using the direct-write method. This development enables production of conductive composite fibers that are precisely positioned, thus facilitating the fabrication of point-to-point connectors *in situ*. Directly written composite fibers possessed diameters ranging from 7 μm to over 100 μm and were typically produced with process yields greater than 85%. Fiber diameter increased with increasing PMMA concentration and decreasing fiber length. Analysis of the rheological data indicated that the CNT-doped solutions experienced significant reduction in extensional viscosity when exposed to strain rates consistent with those imposed by the direct-write process. Conductivity was not significantly affected by PMMA concentration or fiber length and fibers with conductivities as high as 0.1 Sm^{-1} were fabricated.

Acknowledgments

The work presented in this paper was funded by the National Science Foundation NIRT Program (ECS-0506941), NSF PFI Program (EEC-0438604), and National Aeronautics and Space Administration cooperative agreement (NCC5-571).

References

- [1] S. M. Cho, Y. J. Kim, Y. S. Kim, Y. Yang, and S. C. Ha, "The application of carbon nanotube—polymer composite as gas sensing materials," in *Proceedings of the IEEE Sensors*, pp. 701–704, October 2004.
- [2] Y. Yang, M. C. Gupta, and K. L. Dudley, "Towards cost-efficient EMI shielding materials using carbon nanostructure-based nanocomposites," *Nanotechnology*, vol. 18, no. 34, Article ID 345701, 2007.
- [3] A. B. Dalton, S. Collins, E. Muñoz et al., "Super-tough carbon-nanotube fibres," *Nature*, vol. 423, no. 6941, p. 703, 2003.
- [4] J. M. Benoit, B. Corraze, S. Lefrant, W. J. Blau, P. Bernier, and O. Chauvet, "Transport properties of PMMA-carbon nanotubes composites," *Synthetic Metals*, vol. 121, no. 1–3, pp. 1215–1216, 2001.
- [5] S. Pabba, A. N. Sidorov, S. M. Berry et al., "Oriented nanomaterial air bridges formed from suspended polymer-composite nanofibers," *ACS Nano*, vol. 1, no. 1, pp. 52–67, 2007.
- [6] F. Du, J. E. Fischer, and K. I. Winey, "Coagulation method for preparing single-walled carbon nanotube/poly(methyl methacrylate) composites and their modulus, electrical conductivity, and thermal stability," *Journal of Polymer Science, Part B*, vol. 41, no. 24, pp. 3333–3338, 2003.
- [7] R. Haggemueller, H. H. Gommans, A. G. Rinzier, J. E. Fischer, and K. I. Winey, "Aligned single-wall carbon nanotubes in composites by melt processing methods," *Chemical Physics Letters*, vol. 330, no. 3–4, pp. 219–225, 2000.
- [8] J. K. W. Sandler, S. Pegel, M. Cadek et al., "A comparative study of melt spun polyamide-12 fibres reinforced with carbon nanotubes and nanofibres," *Polymer*, vol. 45, no. 6, pp. 2001–2015, 2004.
- [9] J. Gao, M. E. Itkis, A. Yu, E. Bekyarova, B. Zhao, and R. C. Haddon, "Continuous spinning of a single-walled carbon nanotube-nylon composite fiber," *Journal of the American Chemical Society*, vol. 127, no. 11, pp. 3847–3854, 2005.
- [10] J. Zeng, B. Saltysiak, W. S. Johnson, D. A. Schiraldi, and S. Kumar, "Processing and properties of poly(methyl methacrylate)/carbon nano fiber composites," *Composites Part B*, vol. 35, no. 2, pp. 173–178, 2004.
- [11] S. Kumar, H. Doshi, M. Srinivasarao, J. O. Park, and D. A. Schiraldi, "Fibers from polypropylene/nano carbon fiber composites," *Polymer*, vol. 43, no. 5, pp. 1701–1703, 2002.
- [12] A. B. Dalton, S. Collins, J. Razal et al., "Continuous carbon nanotube composite fibers: properties, potential applications, and problems," *Journal of Materials Chemistry*, vol. 14, no. 1, pp. 1–3, 2004.
- [13] F. Ko, Y. Gogotsi, A. Ali et al., "Electrospinning of continuous carbon nanotube-filled nanofiber yarns," *Advanced Materials*, vol. 15, no. 14, pp. 1161–1165, 2003.
- [14] R. Sen, B. Zhao, D. Perea et al., "Preparation of single-walled carbon nanotube reinforced polystyrene and polyurethane nanofibers and membranes by electrospinning," *Nano Letters*, vol. 4, no. 3, pp. 459–464, 2004.
- [15] S. Pabba, S. M. Berry, M. M. Yazdapanah, R. S. Keynton, and R. W. Cohn, "Nanotube suspension bridges directly fabricated from nanotube-polymer suspensions by manual brushing," in *Proceedings of the 6th IEEE Conference on Nanotechnology (IEEE-NANO '06)*, pp. 565–568, Cincinnati, Ohio, USA, June 2006.
- [16] S. M. Berry, S. D. Cambron, S. P. Warren, S. Pabba, R. W. Cohn, and R. S. Keynton, "Characterization and modeling of direct-write fabrication of microscale polymer fibers," *Polymer*, vol. 52, no. 7, pp. 1654–1661, 2011.
- [17] S. M. Berry, S. A. Harfenist, R. W. Cohn, and R. S. Keynton, "Characterization of micromanipulator-controlled dry spinning of micro- and sub-microscale polymer fibers," *Journal of Micromechanics and Microengineering*, vol. 16, no. 9, pp. 1825–1832, 2006.
- [18] A. Tripathi, P. Whittingstall, and G. H. McKinley, "Using filament stretching rheometry to predict strand formation and "processability" in adhesives and other non-Newtonian fluids," *Rheologica Acta*, vol. 39, no. 4, pp. 321–337, 2000.
- [19] Thermo Electron Corp, *CaBER Instruction Manual*.
- [20] P. G. de Gennes, F. Brochard-Wyart, and D. Quere, *Capillarity and Wettuing Phenomena: Drops, Bubbles, Pearls, Waves*, Springer, Berlin, Germany, 2004.
- [21] S. M. Berry, S. P. Warren, D. A. Hilgart et al., "Endothelial cell scaffolds generated by 3D direct writing of biodegradable polymer microfibers," *Biomaterials*, vol. 32, no. 7, pp. 1872–1879, 2011.
- [22] D. Halliday, R. Resnick, and J. Walker, *Fundamentals of Physics*, vol. 1, John Wiley & Sons, Hoboken, NJ, USA, 7th edition, 2005.

- [23] S. S. Rahatekar, K. K. K. Koziol, S. A. Butler et al., "Optical microstructure and viscosity enhancement for an epoxy resin matrix containing multiwall carbon nanotubes," *Journal of Rheology*, vol. 50, no. 5, pp. 599–610, 2006.
- [24] M. Yao and G. H. McKinley, "Numerical simulation of extensional deformations of viscoelastic liquid bridges in filament stretching devices," *Journal of Non-Newtonian Fluid Mechanics*, vol. 74, no. 1–3, pp. 47–88, 1998.